Spring 2020

Dual-Cure Benzoxazine Networks for Additive Manufacturing

Jeremy Weigand

DUAL-CURE BENZOXAZINE NETWORKS FOR ADDITIVE MANUFACTURING

by

Jeremy J. Weigand

A Dissertation
Submitted to the Graduate School,
the College of Arts and Sciences
and the School of Polymer Science and Engineering
at The University of Southern Mississippi
in Partial Fulfillment of the Requirements
for the Degree of Doctor of Philosophy

Approved by:

Dr. Jeffrey Wiggins, Committee Chair
Dr. Robson F. Storey
Dr. Derek L. Patton
Dr. Yoan Simon
Dr. Xiaodan Gu

Dr. Jeffrey Wiggins	Dr. Derek L. Patton	Dr. Karen S. Coats
Committee Chair	Director of School	Dean of the Graduate School

May 2020

Published by the Graduate School

ABSTRACT

The research presented addresses the design of novel materials for additive manufacturing through a dual-cure approach that combines UV initiated free-radical polymerization of an acrylic network combined with the thermally initiated ring opening polymerization of a benzoxazine network. This work is split into three primary sections: the first and second sections focus on the synthesis and characterization of networks based on dual-cure BOX monomers, while the third develops simulation tools to further investigate thermoset networks prepared via additive manufacturing.

A novel 3D printing formulation based on a multifunctional benzoxazine (BOX) monomer possessing both photo and thermally polymerizable functional groups is reported. Printing formulation viscosity is readily tuned using a monofunctional reactive diluent to enable Stereolithography (SLA) 3D printing. In the primary curing step, the printing formulation is UV-cured by SLA 3D printing to prepare accurate parts on the millimeter size scale. The 3D printed parts are then heated in the secondary curing step to activate a thermally initiated BOX ring opening polymerization.

The last chapter of this research applies a combined computational and experimental approach to study the photo initiated free radical polymerization of an acrylate during SLA 3D printing at an atomistic level. After simulated crosslinking, network properties including crosslink density and glass transition temperature are calculated and compared to experimental results.

ACKNOWLEDGMENTS

Thank you to my advisor, Dr. Jeffrey Wiggins. His unique form of mentorship has facilitated both my personal and professional development during my time in his lab. The freedom given to me by “doc” has allowed me to pursue my own scientific interests, through which, I have learned more about myself than I could have ever imagined, and for that, I will always be thankful.

I would like to sincerely thank my committee Dr. Derek Patton, Dr. Yoan Simon, Dr. Xiaodan Gu, and Dr. Robson Storey for helping to shape me as a scientist through their thoughtful comments and discussions. I would also like to gratefully acknowledge Dr. Olivia McNair and Dr. Alicyn Rhoades who have guided, supported, and educated me over the years. You both have mentored me even when you did not have to, and you did it to the best of your ability, I appreciate it more than I can put into words. Finally, thank you to all past, Present, and future members of the WRG, who have helped me immensely over the years.

Thank you to the amazing friends I have made in Hattiesburg, Dr. Andrew Janise, Dr Brian Greenhoe, Joshua Tropp, Jacob Schekman, Travis Palmer, Mike Roth, Matt Hartline, Chris Croshaw, Bernardo Barea Lopez, Jared Bates, Aynslie Fritz and many others. You all have made my time in Hattiesburg some of the best times in my life and I consider myself very lucky to be able to call you all my friends.

DEDICATION

Most importantly, this dissertation is dedicated to my family, who have supported me endlessly throughout graduate school. Hopefully this work is the beginning of many years of creating, learning, and growing together.

TABLE OF CONTENTS

ABSTRACT ii

ACKNOWLEDGMENTS iii

DEDICATION iv

LIST OF TABLES ix

LIST OF ILLUSTRATIONS x

LIST OF SCHEMES xvi

LIST OF ABBREVIATIONS xvii

CHAPTER I – Introduction 1

1.1 Background 1

1.1.1 Additive Manufacturing 2

1.1.2 Dual-Cure Polymer Networks 9

1.1.3 Benzoxazine Developments 12

1.2 Research Motives 18

1.2.1 VPP of Dual-Cure Benzoxazine Networks (Chapter III) 18

1.2.2 Benzoxazine Alloys for Room Temperature VPP (Chapter IV) 19

1.2.3 Molecular Dynamics Simulations of Acrylate Networks (Chapter V) 20

CHAPTER II – Experimental 22

2.1 Materials 22

2.2 Monomer Synthesis 22

2.2.1 Synthesis of Di-Hydroxy Functional Benzoxazine Monomer 22

2.2.2 Synthesis of Di-(meth)acrylate Functional Benzoxazine Monomer (DMBOX) 23

2.2.3 Synthesis of Mono-Hydroxy Functional Benzoxazine Monomer 26

2.2.4 Synthesis of (meth)acrylate Functional Benzoxazine Monomer (MBOX) 27

2.3 Formulation preparation and 3D Printing 30

2.4 Characterization 32

2.4.1 Proton Nuclear Magnetic Resonance Spectroscopy (^{1}H NMR) 32

2.4.2 Rheological Experiments 33

2.4.3 Fourier Transform Infrared Spectroscopy 35

2.4.4 Thermogravimetric analysis 36

2.4.5 Differential Scanning Calorimetry 36

2.4.6 Dynamic Mechanical Analysis 37

2.4.7 Mechanical Analysis 38

2.5 Molecular Dynamics Simulation Methods 38

2.5.1 Simulated Photopolymerization 39

2.5.2 Simulated Annealing 42

CHAPTER III - 3D Printing of Dual-Cure Benzoxazine Networks 43

3.1 Abstract 43

3.2 Results and Discussion 44

3.2.1 Printing Formulation Preparation and Rheological Characterization 44
3.2.2 Thermal Stability of Printed Parts 55
3.2.3 DSC Studies of Primary and Secondary Cure 59
3.2.4 Spectroscopic Studies of Primary and Secondary Cure 60
3.2.5 Thermomechanical Properties After Primary and Secondary Cure 64
3.2.6 Conclusion 68
CHAPTER IV – Dual Cure Benzoxazine Blends 70
4.1 Abstract 70
4.2 Results and Discussion 71
4.2.1 Printing Formulation Preparation and Rheological Characterization 71
4.2.2 Thermal Stability and Ring Opening Polymerization of BOX 81
4.2.3 Thermomechanical Properties 90
4.2.4 SLA 3D Printing Performance 94
4.2.5 Conclusions 95
CHAPTER V – Molecular Dynamics Simulations of Acrylate Networks 96
5.1 Abstract 96
5.2 Results and Discussion 97
5.2.1 Viscosity and Cure Kinetics of Printing Formulations 97
5.2.2 Degree of Cure After 3D Printing. 101
5.2.3 Disordered Cell Preparation and Simulated Crosslinking 102

5.2.4 Experimental and Simulated Network Properties 107

5.3 Conclusions 113

CHAPTER VI – Conclusions and Future Work 114

APPENDIX A – Monomer Structure Validations 117

APPENDIX B – Supplementary Experiments 123

REFERENCES 125

LIST OF TABLES

Table 1.1 Summary of typical polymers used for common AM methods[2,7] 3

Table 3.1 Photorheology of 3D printing formulations with 1 wt% TPO-L and increasing DMBOX concentration 53

Table 3.2 Decomposition temperatures of 60:40 DMBOX:RD un-cured monomer blend, 3D printed networks, and 3D printed networks with secondary cure at 200 °C for 1 hr.. 57

Table 3.3 Summary of 60:40 DMBOX:RD thermomechanical data before and after thermally initiated BOX ring opening polymerization 66

Table 4.1 Photorheology of 3D printing formulations with 1 wt% TPO-L and increasing DMBOX concentration 78

Table 4.2 Summary of Thermal Degradation Temperatures of BOX Blends 82

Table 4.3 Summary of 50 mol% DMBOX : MBOX thermomechanical data before and after thermally initiated BOX ring opening polymerization 93

Table 5.1 DOC calculated for each UA loading level 102

Table 5.2 Summary of simulation cell compositions and the associated experimental formulation. Note: 20 TPO-L photoinitiator molecules were added to each cell 103

Table 5.3 Crosslinking simulations compared to photorheology results 105

Table 5.4 Calculated crosslink densities for each formulation compared to number of crosslinks achieved in each simulation 110

LIST OF ILLUSTRATIONS

Figure 1.1 A) Schematic of vat photopolymerization additive manufacturing B) Parts fabricated using vat photopolymerization additive manufacturing 4

Figure 1.2 General representation of a hybrid polymer network and interpenetrating polymer network 11

Figure 2.1 ^{1}H-NMR spectrum of DMBOX monomer 25

Figure 2.2 ATR-FTIR spectra of (A) di-hydroxy and di-(meth)acrylate functional characteristic BOX absorptions and (B) hydroxyl peak at 3400 cm^{-1}, carbonyl peak at 1718 cm^{-1}, and (meth)acrylate double bond peak at 1637 cm^{-1}. 26

Figure 2.3 ^{1}H-NMR spectrum of MBOX monomer 29

Figure 2.4 ATR-FTIR spectra of (A) mono-hydroxy and mono-(meth)acrylate functional characteristic BOX absorptions and (B) hydroxyl peak at 3400 cm^{-1}, carbonyl peak at 1718 cm^{-1}, and (meth)acrylate double bond peak at 1637 cm^{-1} 30

Figure 2.5 Form 2 SLA 3D Printer 32

Figure 2.6 SMARTS Patterns used to define reactive sites during crosslinking simulations. 40

Figure 2.7 Simulated photopolymerization workflow[72] 41

Figure 3.1 Plot of viscosity vs shear rate of DMBOX based blends 45

Figure 3.2 Plot of viscosities of DMBOX based blends at 1.7 s^{-1} 47

Figure 3.3 Storage (G') and loss (G'') moduli as a function of irradiation time with increasing [TPO-L] for 60:40 DMBOX:RD blend 49

Figure 3.4 Gel time as a function of photoinitiator concentration for 60:40 DMBOX:RD blend 49

Figure 3.5 Tan Delta measured as a function of irradiation time for 60:40 DMBOX:RD blend with 1 wt% TPO-L 51
Figure 3.6 Shear storage and loss modulus of 3D printing formulations with 1 wt% TPO-L and increasing DMBOX concentration as a function of irradiation time..... 53
Figure 3.7 Axial force as a function of irradiation time for BOX blends with 1 wt% TPO-L and increasing DMBOX concentration as a function of irradiation time..... 55
Figure 3.8 weight loss profiles of 60:40 DMBOX:RD un-cured monomer blend, 3D printed networks, and 3D printed networks with secondary cure at 200 °C for 1 hr 57
Figure 3.9 3D printed 60:40 DMBOX:RD blend held isothermally at 200 °C for 150 min 58
Figure 3.10 DSC thermograms for (a) un-cured 60:40 DMBOX:RD monomer blend, (b) after 3D printing, and after thermal treatment at 200 °C for (c) 30 (b) 60 and (e) 90 minutes 60
Figure 3.11 Images of 3D printed parts and ATR-FTIR spectra of 60:40 DMBOX:RD formulation before printing (a), after 3D printing (b), and after 1-hr at 200 °C (c) 61
Figure 3.12 Real-time conversion plots of acrylate photopolymerization (1 wt% TPO-L photoinitiator, 250 mW cm^{-2}) and benzoxazine ring opening polymerization (200 °C) .. 63
Figure 3.13 Tan Delta plotted as a function of temperature 60:40 DMBOX:RD 3D printed parts before and after thermally initiated BOX ring opening polymerization..... 65
Figure 3.14 Storage modulus plotted as a function of temperature 60:40 DMBOX:RD 3D printed parts before and after thermally initiated BOX ring opening polymerization..... 66
Figure 3.15 Uniaxial compression stress vs strain for 60:40 DMBOX:RD 3D printed parts before and after thermally initiated BOX ring opening polymerization 67

Figure 4.1 Plot of viscosity vs shear rate of DMBOX based blends 73
Figure 4.2 Storage modulus of 3D printing formulations with increasing TPO-L loading level as a function of time 74
Figure 4.3 Gel time as a function of TPO-L concentration. 75
Figure 4.4 Tan Delta measured as a function of irradiation time for 50 mol% DMBOX : MBOX blend with 0.25 wt% TPO-L 76
Figure 4.5 Shear storage and loss modulus of 3D printing formulations with 1 wt% TPO-L and increasing DMBOX concentration as a function of irradiation time 78
Figure 4.6 Conversion of (meth)acrylate C=C double bond and BOX as a function of irradiation time. 80
Figure 4.7 TGA weight loss profiles of 50 mol% DMBOX : MBOX un-cured monomer blend, 3D printed networks, and 3D printed networks after thermal cure 82
Figure 4.8 3D printed 50 mol% DMBOX : MBOX blend held isothermally for 1 hr at increasing temperatures. Labels indicate weight loss % at each temperature 83
Figure 4.9 3D printed 50 mol% DMBOX : MBOX blend held isothermally at 180 °C for 8 hrs 84
Figure 4.10 DSC thermograms for 50 mol% DMBOX : MBOX monomer blend, after 3D printing, and after thermal cure 86
Figure 4.11 Conversion of BOX ring opening polymerization at increasing isothermal temperatures 88
Figure 4.12 Rheological characterization of thermally intiated BOX polymerizatio 90
Figure 4.13 Tan Delta plotted as a function of 50 mol% DMBOX : MBOX 3D printed parts before and after thermally initiated BOX ring opening polymerization 92

Figure 4.14 Storage modulus plotted as a function of temperature 50 mol% DMBOX : MBOX 3D printed parts before and after thermally initiated BOX ring opening polymerization 93

Figure 4.15 SLA 3D printed object example from the 50 mol% DMBOX : MBOX monomer blend with 1 wt% TPOL and 0.07 wt% UV absorber before and after thermal polymerization of BOX..... 94

Figure 5.1 Viscosity as a function of shear rate for printing formulations, Mol% indicates UA loading level..... 98

Figure 5.2 Complex viscosity plotted as a function of step time, Mol% indicates UA loading level..... 100

Figure 5.3 Average gel time plotted as a function of UA loading level. 100

Figure 5.4 Left, full FTIR spectra of 60mol% 3D printed sample. Right, comparison of C=C stretch absorbance before and after 3D printing. 102

Figure 5.5 Representative plot of density as a function of simulation time at 300K for a disordered system composed of 90 Bis GMA monomers and 90 UA monomers. 104

Figure 5.6 Largest molecular weight fraction and 2nd largest molecular weight fraction plotted as a function of cross-link saturation for formulations with increasing UA loading level..... 105

Figure 5.7 C=C double bond conversion profiles for formulations with increasing UA mol %..... 106

Figure 5.8 Plots of Tan Delta and storage modulus as a function of temperature with increasing UA mol %..... 108

Figure 5.9 Rubbery modulus as a function of UA mol% and images of crosslinked cells from simulations with increasing UA mol% where unreacted monomer and oligomers are colored red and yellow respectively 109
Figure 5.10 Representative density vs temperature plot obtained during simulated annealing of a 50 mol% UA network 111
Figure 5.11 Glass transition temperature plotted as a function of UA mol%..... 112
Figure A.1 H^1 NMR (600 MHz) spectrum of Di-Hydroxy Functional Benzoxazine Monomer..... 117
Figure A.2 H^1 NMR (600 MHz) spectrum of Di-(meth)acrylate Functional Benzoxazine Monomer (DMBOX) 117
Figure A.3 ATR-FTIR spectrum of Di-Hydroxy Functional Benzoxazine Monomer ... 118
Figure A.4 ATR-FTIR spectrum of Di-(meth)acrylate Functional Benzoxazine Monomer (DMBOX)..... 118
Figure A.5 H^1 NMR (600 MHz) spectrum of Mono-Hydroxy Functional Benzoxazine Monomer..... 119
Figure A.6 H^1 NMR (600 MHz) spectrum of Mono-(meth)acrylate Functional Benzoxazine Monomer (MBOX) 119
Figure A.7 ATR-FTIR spectrum of Mono-Hydroxy Functional Benzoxazine Monomer 120
Figure A.8 ATR-FTIR spectrum of Mono-Hydroxy Functional Benzoxazine Monomer and Mono-(meth)acrylate Functional Benzoxazine Monomer (MBOX) 120
Figure A.9 H^1 NMR (300 MHz) spectrum of Bis-GMA Monomer 121
Figure A.10 ATR-FTIR spectrum of Bis-GMA Monomer 121

Figure A.11 H^1 NMR (300 MHz) spectrum of Genomer 1122 Monomer 122

Figure A.12 ATR-FTIR Spectra of Genomer 1122 Monomer 122

Figure B.1 Strain sweep of 60:40 DMBOX:RD blend with 1 Wt% TPO-L and a 0.5 mm gap 123

Figure B.2 Storage and loss modulus of 50 mol% MBOX blend with increasing TPO-L loading level as a function of time 124

LIST OF SCHEMES

Scheme 1.1 General photopolymerization mechanism..... 5

Scheme 1.2 Photolysis of type 1 photoinitiator 6

Scheme 1.3 Common free-radical monomers and photoinitiators used in VPP AM[2,8] 8

Scheme 1.4 Epoxide and vinyl ether monomers used for cationic photopolymerization[2,8] 9

Scheme 1.5 General benzoxazine monomer synthesis and polymerization of mono and difunctional monomers 13

Scheme 1.6 Proposed BOX monomer synthesis mechanism 15

Scheme 1.7 Suggested cationic ring opening polymerization mechanism of benzoxazines 16

Scheme 2.1 Synthesis of Di-(meth)acrylate Functional Benzoxazine Monomer (DMBOX) 24

Scheme 2.2 Synthesis of Mono-(meth)acrylate Functional Benzoxazine Monomer (MBOX) 28

Scheme 2.3 General reaction scheme of a photoinitiated free radical polymerization..... 40

LIST OF ABBREVIATIONS

°C	Centigrade
ABS	Acrylonitrile Butadiene Styrene
AM	Additive Manufacturing
BHT	Butylated hydroxytoulene
Bis-GMA	Bisphenol A-glycidyl methacrylate
BOX	Benzoxazine
BPA	Bisphenol-A
CAD	Computer-Aided Design
CDCl3	Deuterated chloroform
CH2Cl2	Dichloromethane
CLIP	Continuous Liquid Interface Production
DGEBA	Dglycidyl ether of bisphenol a
DLP	Digital Light Processing
DMA	Dynamic Mechanical Analysis
DMA	Dynamic Mechanical Analysis
DSC	Differential Scanning Calorimetry
E’	Storage Modulus
E’’	Loss Modulus
FDM	Fused Deposition Modeling
FTIR	Fourier Transform Infrared
g	Gram
G’	Shear Storage Modulus

G”	Shear Loss Modulus
GPa	Gigapascal
HDPE	High Density Polyethylene
HIPS	High Impact Polystyrene
HPN	Hybrid Polymer Network
hr	Hour
Hz	Hertz
IPN	Interpenetrating Polymer Network
J	Joule
L	Liter
LOM	Laminated Object Manufacturing
m	Meter
Mc	Molecular weight between cross-links
MD	Molecular Dynamics
MgSO4	Magnesium Sulfate
MHz	Megahertz
Min	Minute
mL	Milliliter
mm	Millimeter
mmol	Millimole
MPa	Megapascal
mW	Milliwatt
NaOH	Sodium Hydroxide

nm	Nanometer
NMR	Nuclear Magnetic Resonance
PA	Polyamide
PC	Polycarbonate
PEEK	Polyether ether ketone
PLA	Polylactic acid
PMMA	Poly(methyl methacrylate)
PP	Polypropylene
PS	Polystyrene
RD	Reactive Diluent
ROP	Ring Opening Polymerization
SAN	Styrene−Acrylonitrile copolymer
SLA	Stereolithography
SLS	Selective Laser Sintering
T_g	Glass Transition Temperature
TPU	Thermoplastic Polyurethane
VPP	Vat Photopolymerization

CHAPTER I – Introduction

1.1 Background

Since the beginning of time, mankind has searched for novel ways to shape materials for specific applications. From learning to sharpen rocks for hunting to injection molding of large-scale parts with high throughput, humanity has evolved and developed faster, more precise methods of manipulating form and function of materials to better serve a desired purpose. Introduced in the 1980s, Additive manufacturing (AM), commonly referred to as 3D printing, has emerged as an advanced manufacturing method to produce complex geometries and shows great potential in a variety of industries.

ASTM defines AM as "the process of joining materials to make objects from three-dimensional model data, usually layer-by-layer, as opposed to subtractive manufacturing methodologies".[1] AM is quickly proliferating in aerospace, medical, and robotics applications due to its ability to rapidly produce complex 3D structures with micrometer precision.[2] Consequently, the AM market is growing, with revenues estimated at $2.7 billion in 2016, a growth of 12.9% from 2015, and these revenues are expected to surpass $100 billion within the next two decades.[3] Major aerospace companies including Boeing, Bell, and Airbus have all recognized the utility of AM, fabricating critical and non-critical aircraft parts and tools using various AM methods. In 2015 more than 20,000 non-metallic AM parts were installed on aircrafts; Boeing specifically having 16 military and commercial aircraft that fly with parts fabricated using AM technologies.[3,4] Industrial highlights such as these demonstrate not just the rapid advancement of AM as a manufacturing method, but also the increasing demand for performance from the materials applied to AM.

One of the key challenges facing the AM market is related to the development of new materials tailored for the innovative process. Despite ever increasing research efforts in the area of AM material development, parts produced using AM typically underperform in the area of mechanical properties.[2] This limiting factor may be addressed by the careful design of new polymers engineered specifically for the unique considerations of AM.[5]

1.1.1 Additive Manufacturing

While traditional manufacturing methods operate by removing material to fabricate objects, in AM, complex objects and assemblies are readily created by depositing or fusing material in successive layers. This can be accomplished by a broad range of AM methods including selective laser sintering (SLS), inkjet and polyjet printing, fused deposition modeling (FDM), laminated object manufacturing (LOM), direct write printing technologies, and stereolithography (SLA).[6] All standard AM processes begin with the development of a computer-aided design (CAD) file to define part geometry and size. The CAD file is then converted into a series of 2D cross-sections through a process called “slicing”, and the resulting 2D cross-sections define the layers that will be “printed” to build the part. Once the file is uploaded to the 3D printer, individual layers of material are deposited or bonded together in a pattern defined by the slicing process. A key advantage of AM is that this manufacturing workflow is not restricted by part design constraints compared to other traditional polymer processing techniques which require molds or machining. Polymeric materials used for AM may vary from a wide range of thermoplastics to thermosets depending on the AM process

used and desired part properties. A summary of AM methods and materials commonly processed using each approach are presented in Table 1.1. While thermoplastic polymers in powder, filament or sheet form are common, thermosetting monomers processable via photopolymerization have achieved wide spread use among a wide range of industries.

Table 1.1 Summary of typical polymers used for common AM methods[2,7]

AM Method	Typical Feature Resolution	Typical Materials
SLS	50 – 100 µm	PA6, PA11, PA12, HDPE. PP, PEEK, TPU, PS, HIPS, PMMA, SAN, PC
FDM	100 – 150 µm	ABS, PLA. PC, PA, HIPS,
SLA	25 – 100 µm	Acrylates, Epoxides, Vinyl Ethers
Polyjet	25 µm	Acrylates

The wide selection of polymer chemistries suitable for photopolymerizations have recently enabled innovations in a specific subset of photopolymerization-based AM techniques commonly referred to as vat photopolymerization (VPP).[1,2,8,9] Figure 1.1 depicts a general schematic of the VPP process and examples of parts prepared using VPP. Most modern VPP devices operate in a “bottom up” configuration where a build platform is immersed in a bath of printing formulation and a light source selectively initiates photopolymerization through an optically transparent window. This process

continues in an iterative, layer-by-layer approach until the final structure defined by the CAD file is formed. Examples of VPP techniques include SLA, digital light processing (DLP), and continuous liquid interface production (CLIP). These AM methods typically rely on very precise light or laser sources to initiate the photopolymerization of each layer, which allows for high feature resolution on the micrometer size scale.[10] The high feature resolution and ability to tailor material properties using VPP AM has enabled innovations in a wide range of fields that include robotics, microfluidics, biomedical devices, and dentistry.[11–13]

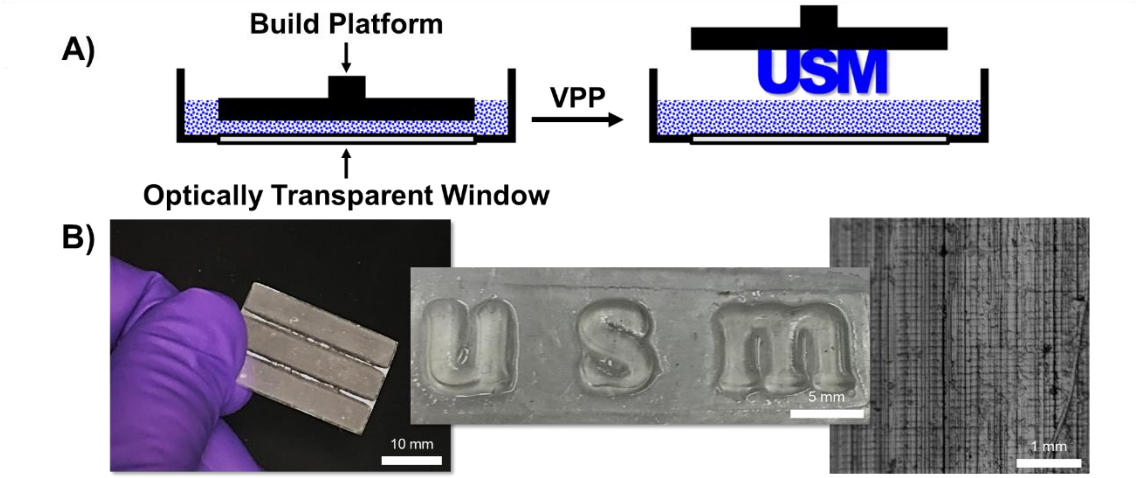

Figure 1.1 A) Schematic of vat photopolymerization additive manufacturing B) Parts fabricated using vat photopolymerization additive manufacturing

VPP utilizes monomers or prepolymer oligomers that are viscous liquids at room temperature which, upon exposure to a UV light, rapidly photopolymerize to form crosslinked polymer networks. VPP AM formulations blend these UV polymerizable monomers or prepolymer oligomers with a low concentration of photoinitiator, which upon UV irradiation generates an active species to initiate photopolymerization. Once a

radical is formed, it adds across the double bond of a monomer during the initiation step, after which the propagating radical may continue to add to monomer until termination. Several termination events may occur, including radical coupling events, where either initiating or propagating radicals may combine, disproportionation, where a radical may abstract a hydrogen atom from the growing polymer chain end, or oxygen inhibition, where a peroxy radical with relatively low reactivity is formed. Scheme 1.1 illustrates the general reaction mechanism of a typical photopolymerization using vinyl monomers.

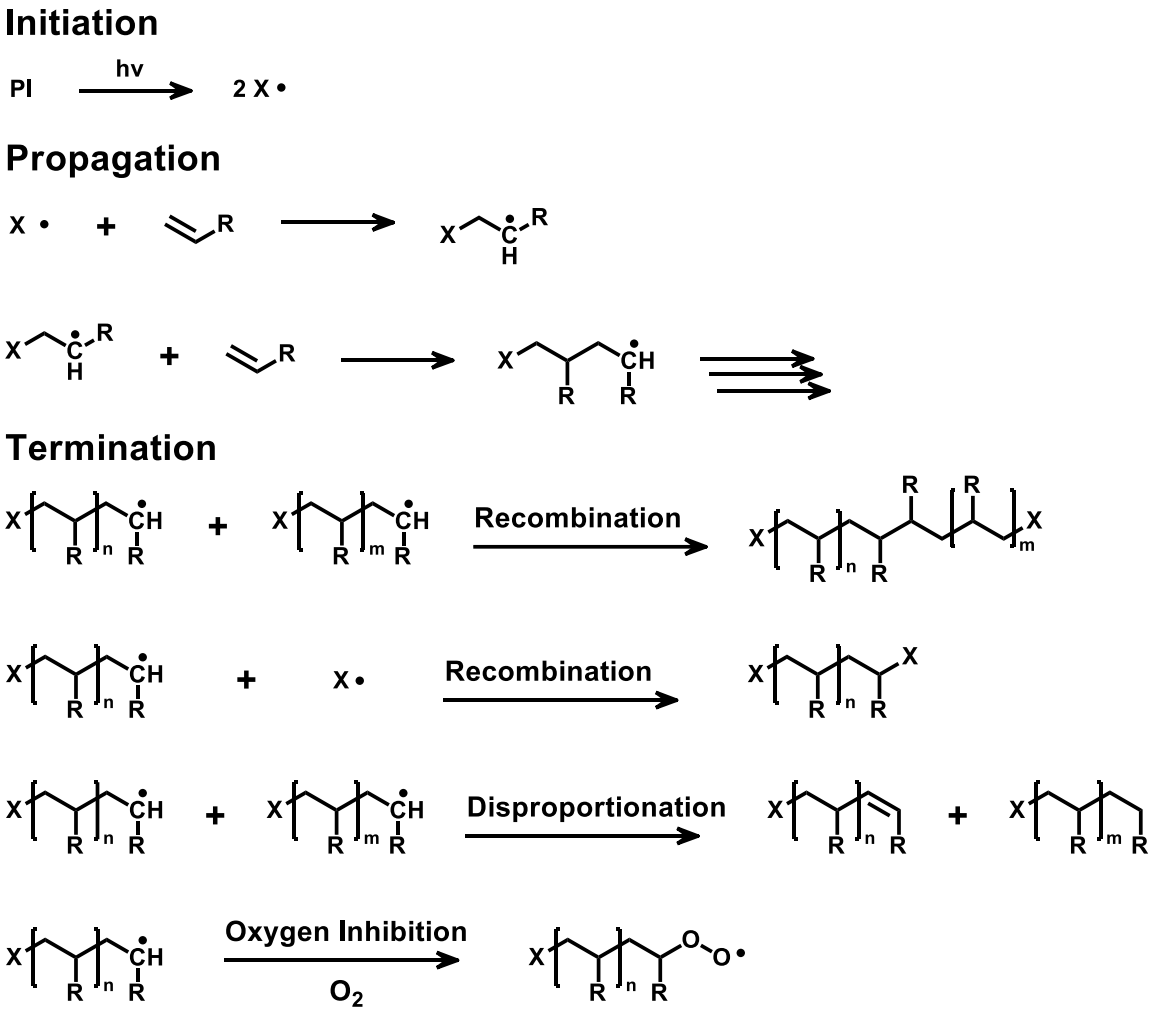

Scheme 1.1 General photopolymerization mechanism

Photoinitiators used in VPP AM techniques are typically single molecules classified as Norrish type I initiators.[2,8] These molecules cleave into reactive radical fragments upon photolysis that may further react to initiate polymerization. Specifically, acyl phosphine oxide photoinitiators are commonly employed in VPP due to their efficient initiation at relatively high wavelengths of light and the high reactivity of phosphonyl radicals generated upon photolysis.[14–16] The selection of a photoinitiator for a given VPP AM formulation must be based on compatibility with the monomer blend and the wavelength of light to be used. Liquid photoinitiators are preferred as they typically improve miscibility with the monomer blend. Additionally, the initiator should have a strong absorbance in the spectrum of light emitted by the laser or light source. Photoloysis of a common Norrish type I photoinitiator Ethyl(2,4,6-trimethylbenzoyl) phenylphosphinate, trade name TPO-L, is depicted in Scheme 1.2. This photoinitiator is used for the research herein due to formulation miscibility, the high efficiency of radical generation and the good overlap between the 3D printer laser output wavelength and photoinitiator absorbance.

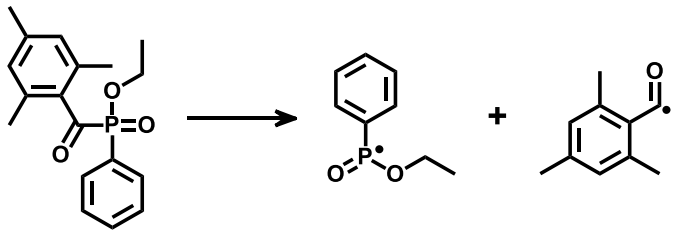

Scheme 1.2 Photolysis of type 1 photoinitiator

Acrylate or (meth)acrylate chemistries are the dominant choice for monomers in photopolymerization based AM techniques. Acrylates are electron poor vinyl monomers commonly utilized in photopolymerizations due to their high UV reactivity and molecular design versatility. Acrylate and (meth)acrylate monomers are commercially available with a variety of functionalities and backbone structures and are typically able to be prepared using straightforward synthetic techniques.

Two of the most commonly used acrylates in VPP AM are polyurethane or diglycidyl ether of bisphenol a (DGEBA) moieties terminated with acrylate or methacrylate functional groups.[17] These monomers are a logical choice as they are commercially available, exhibit fast photopolymerization rates, and provide good mechanical and thermal stability.[2,8] Often however, multi-functional acrylate or methacrylate monomers used for VPP are too viscous for the VPP process without the addition of a low viscosity reactive diluent or comonomer.[18,19] Reactive diluents used in VPP AM are commonly low viscosity acrylate functional monomers that will reduce formulation viscosity but also react into the final crosslinked network. Structures of commonly used monomers, reactive diluents, and photoinitiators in VPP AM are illustrated in Scheme 1.3.

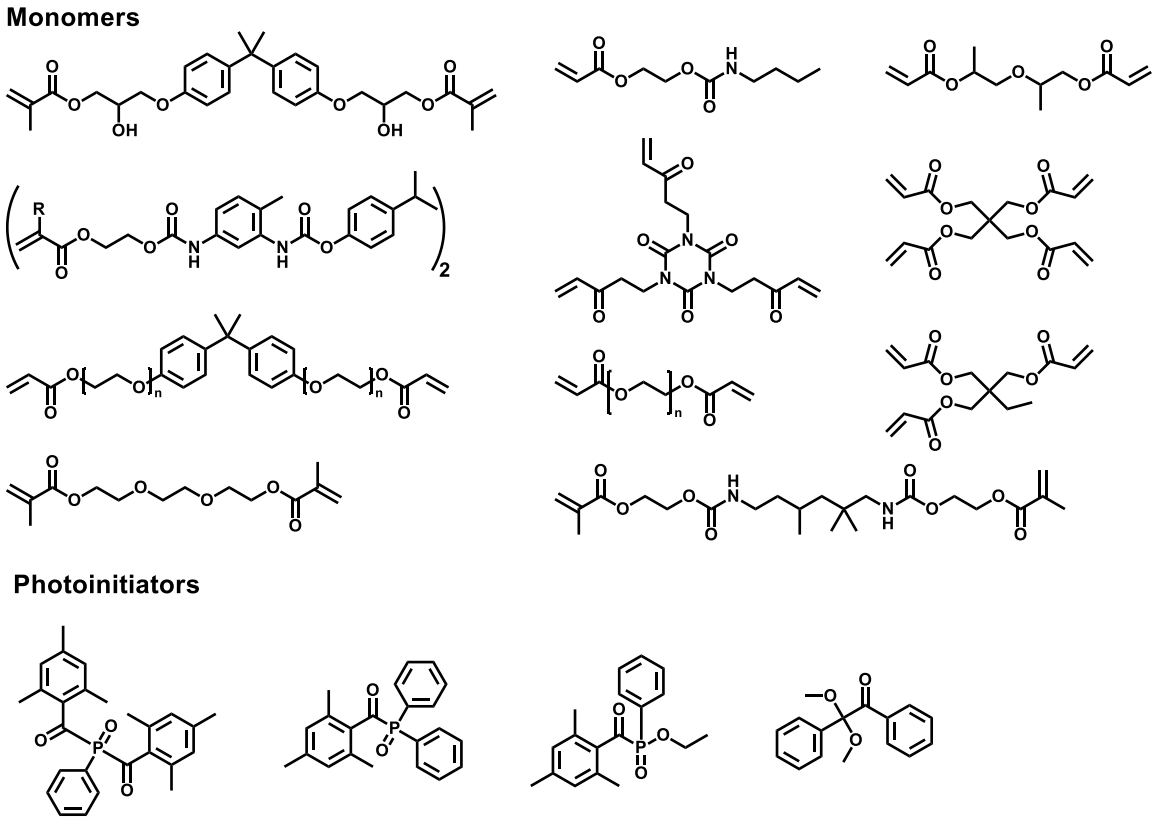

Scheme 1.3 Common free-radical monomers and photoinitiators used in VPP AM[2,8]

Scheme 1.4 shows examples of cationic polymerizable monomers used for VPP AM. Catatonically polymerizable epoxy functional monomers are a common choice in the scientific and patent literature as they have favorable mechanical properties and low shrinkage values upon photopolymerization when compared to acrylate or (meth)acrylate functional monomers.[2] While epoxy functional monomers reduce shrinkage upon photopolymerization, they also suffer from much slower photopolymerize rates than free radically polymerizable acrylate and (meth)acrylate functional monomers. To address this issue, often epoxy monomers are blended with more reactive vinyl ether monomers to ensure sufficient crosslinking during the AM process while also reducing part shrinkage.

Another approach to tune AM formulations is by blending free radically polymerizable monomers shown in Scheme 1.3 with cationic monomers to synthesize "dual-cure" networks.[2,8]

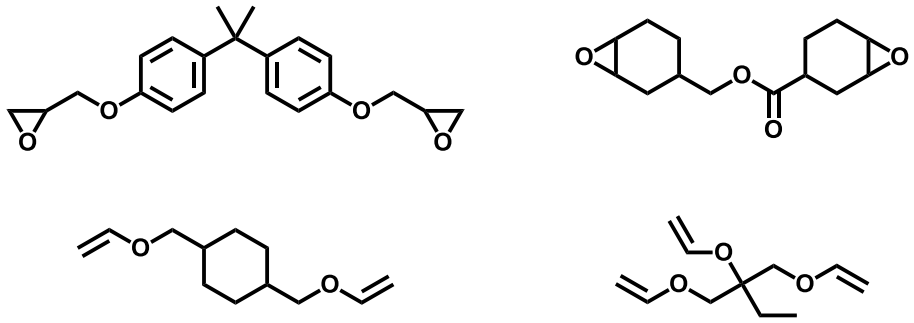

Scheme 1.4 Epoxide and vinyl ether monomers used for cationic photopolymerization[2,8]

1.1.2 Dual-Cure Polymer Networks

Dual-cured polymer networks are synthesized by monomers that react by two discrete curing mechanisms to form two separate polymer networks.[20] These curing mechanisms can occur simultaneously or in series, depending on the stimuli required to initiate each reaction. The use of dual-cure mechanisms offers the ability to combine the advantages of multiple polymerization techniques to form polymer networks with tailorable properties. There are two common types of polymer network architectures that can be synthesized by the dual-cure approach, interpenetrating polymer networks (IPNs) and "hybrid" polymer networks (HPNs).

Since the first synthesis of an IPN in 1914 by *Aylsworth*, IPNs have been extensively studied utilizing many different polymer compositions.[21] IPNs are polymer networks comprised of two or more chemically different polymer networks, which are

not covalently bound, but held together by physical entanglements between polymer chains.[22] IPNs may be synthesized by either sequentially or simultaneously polymerizing each network. During sequential preparation of an IPN, the first polymer network is crosslinked before the second monomer and crosslinker blend is subsequently swollen into the network and polymerized during a second reaction step. During simultaneous preparation of an IPN the monomers and crosslinkers for both polymer networks are blended, and the separate, noninterfering polymerizations are carried out concurrently. Epoxy-acrylate systems for example, are commonly combined to synthesize IPNs as the advantages of a UV initiated acrylate photopolymerization can be combined with the mechanical strength of a thermally polymerized epoxy network.[23]

While IPNs allow for the combination of different polymer networks resulting in highly tailorable properties, they are limited by a balance of the miscibility between the two distinct network components and polymerization kinetics.[24] The thermodynamic miscibility between the two IPN components may be calculated according to the Flory-Huggins solution theory, where during the crosslinking of each network, molecular weight builds and the entropy of mixing between the two networks is reduced. This reduction in entropy of mixing ultimately reduces the miscibility between the two components and may cause entropically driven phase separation during polymerization. Crosslinking of each component however, will prevent phase separation of the two networks by forming physical entanglements that interlock the two networks together if polymerization rates are rapid compared to diffusion and phase separation rates.[24] HPNs offer a strategy to avoid the issue of phase separation by incorporating two separate

functional groups on the same monomer, thus each polymer network may be derived from the same monomer, limiting phase separation effects during polymerization.[25]

In contrast to IPNs, HPNs are a combination of two or more chemically different polymer networks that are covalently bound together.[25] Differences in network connectivity between HPNs and IPNs are illustrated in Figure 1.2. HPNs offer potential for improved homogeneity and improved reaction rates compared to IPNs as they are held together by crosslinks rather than physical entanglements.[26]

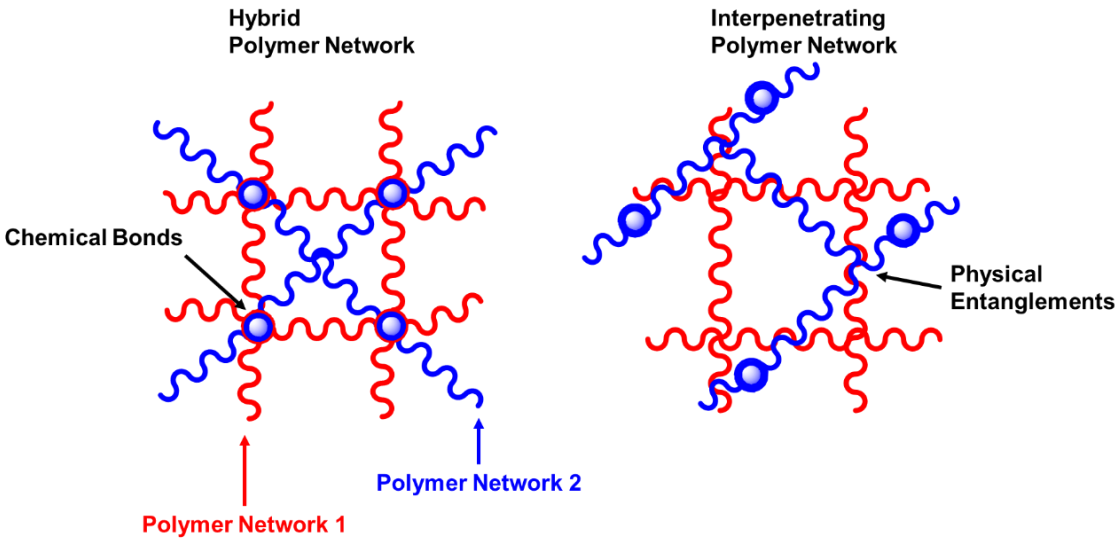

Figure 1.2 General representation of a hybrid polymer network and interpenetrating polymer network

Dual-cure polymer networks based on photopolymerizations are a popular choice due to their rapid polymerization rates at ambient temperatures and the ability to tailor network properties. Specifically, free radical photopolymerizations of acrylate or (meth)acrylate functional monomers are often selected as the primary polymerization in dual-cure networks due to their straightforward, modular synthesis. This allows for the

facile preparation of networks with a wide range of properties. Additionally, ambient temperature photopolymerization tolerates the incorporation of thermal initiated moieties for sequential polymerization of the second polymer network. A variety of networks have been studied in the literature using this strategy, including the combination of acrylate functionality with epoxide[23], oxetane[27,28], and benzoxazine (BOX)[29–31] functionalities.

1.1.3 Benzoxazine Developments

First established by Holly and Cope in 1944, benzoxazines are heterocyclic compounds that are rapidly gaining attention in the aerospace industry as an alternative to phenolic and epoxy-based materials.[32] After early work by Holly, Cope, Burke, and others, it was not until a series of patents in the 1980's by Higginbottom that multifunctional BOX monomers were studied as thermosetting matrices.[33–36] After this key advancement in the BOX literature, most research that followed has focused on understanding polymerized BOX thermoset networks. Much of the foundational work studying BOX networks was done by *Ishida et al* in the 1990s, which established many of the key BOX properties that others have built upon.[37–40] These unique properties include modular molecular design, high glass transition temperatures, high modulus, good thermal stability, low moisture absorption, no by-products released during polymerization, near-zero chemical shrinkage, and ease of thermal polymerization by self-initiation.[41]

The general synthesis of BOX monomers involves the reaction of a phenolic derivative, primary amine, and formaldehyde as outlined in Scheme 1.5. This scheme highlights both the simplistic nature of BOX monomer synthesis and the high degree of

molecular design modularity afforded by BOX polymers. Both R and R' in scheme 1.5 are available for incorporation of a wide variety of functionalities and may be enabled using a broad range of commercially available starting materials. Additionally, in their di-functional form, both R and R' remain tunable to provide a wide variety of network backbone structures and advanced functionalities.

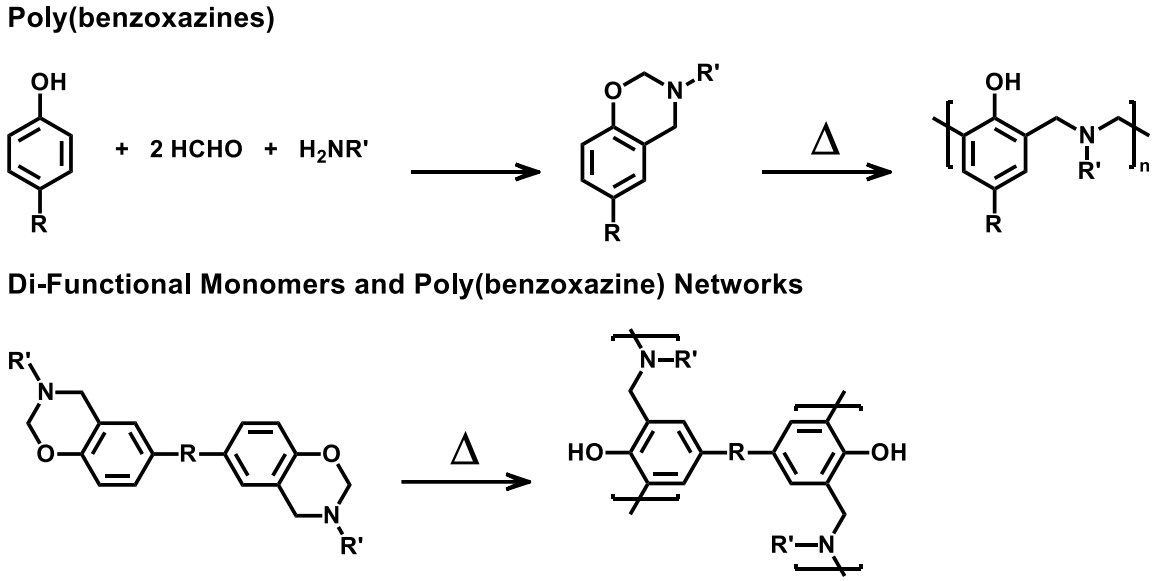

Scheme 1.5 General benzoxazine monomer synthesis and polymerization of mono and difunctional monomers

Scheme 1.6 illustrates the proposed mechanism for the formation of the oxazine ring, where the primary amine reacts with formaldehyde to generate an intermediate aminomethylol group which further reacts to form a 1,3,5-triazaine compound. The triazine ring then reacts with a phenol and formaldehyde to form the oxazine ring.[42] BOX monomers have been synthesized in the literature through a variety of methods ranging from homogeneous or heterogeneous solutions to reactions in the melt with high solids content. In solution, solvent selection has been shown to have a significant influence on

efficiency of forming the benzoxazine ring. In general, it has been observed that solvents with low dielectric constants result in the highest yields of BOX monomer. Solvents such as dichloromethane, chloroform, dioxane, and xylenes are popular choices in the literature for the synthesis of a variety of BOX monomers.[43] The molecular design modularity afforded by this robust and straightforward monomer synthesis allows for the opportunity to study a variety of monomer structures. As a result, these monomers may then be polymerized into crosslinked thermoset networks with a wide range of structures and functionalities with highly tailorable properties

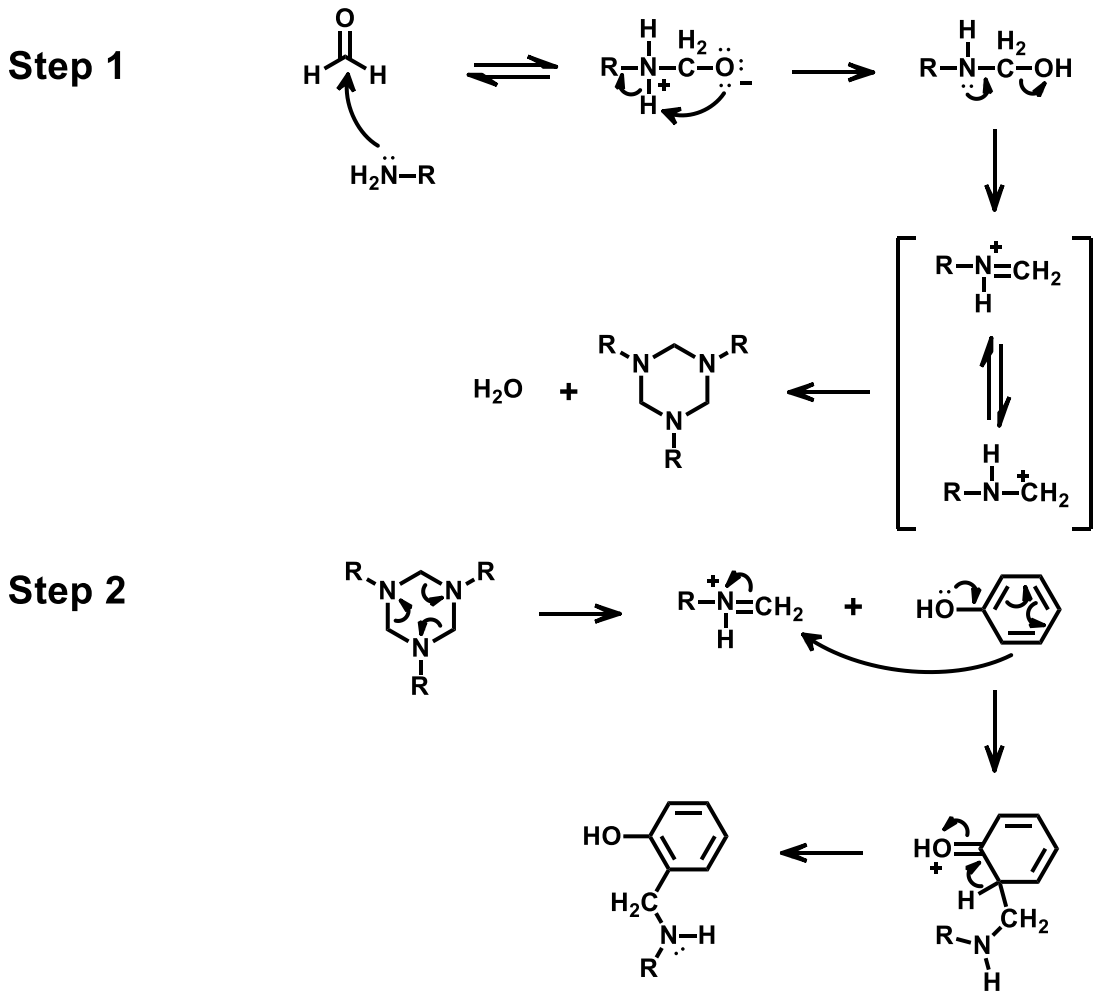

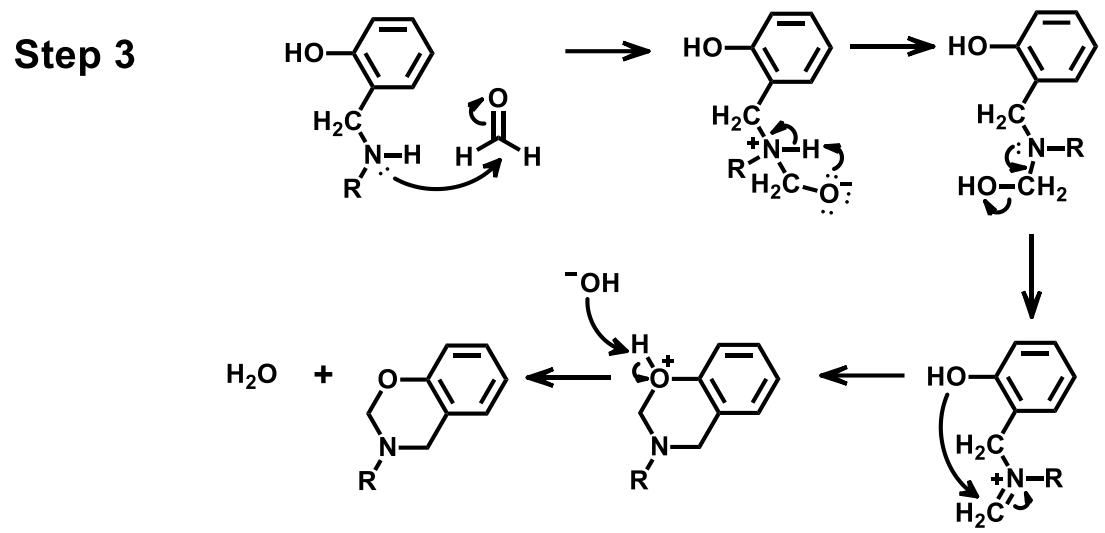

Scheme 1.6 Proposed BOX monomer synthesis mechanism

BOX monomers undergo ring opening polymerization (ROP) upon heating with either the addition of a curing agent or may self-polymerize, where phenolic impurities act as initiators. Thermally activated ROP is achieved by heating monomers (~150 °C) to begin opening BOX rings which will simultaneously supply phenolic moieties to initiate further ring opening. BOX ROP is a form of addition polymerization where benzoxazine monomers react at the terminal end of a polymer chain which acts as a reactive center. It is hypothesized that under no catalytic influence, the ROP of benzoxazines involves a cationic ring opening process as depicted in Scheme 1.7.

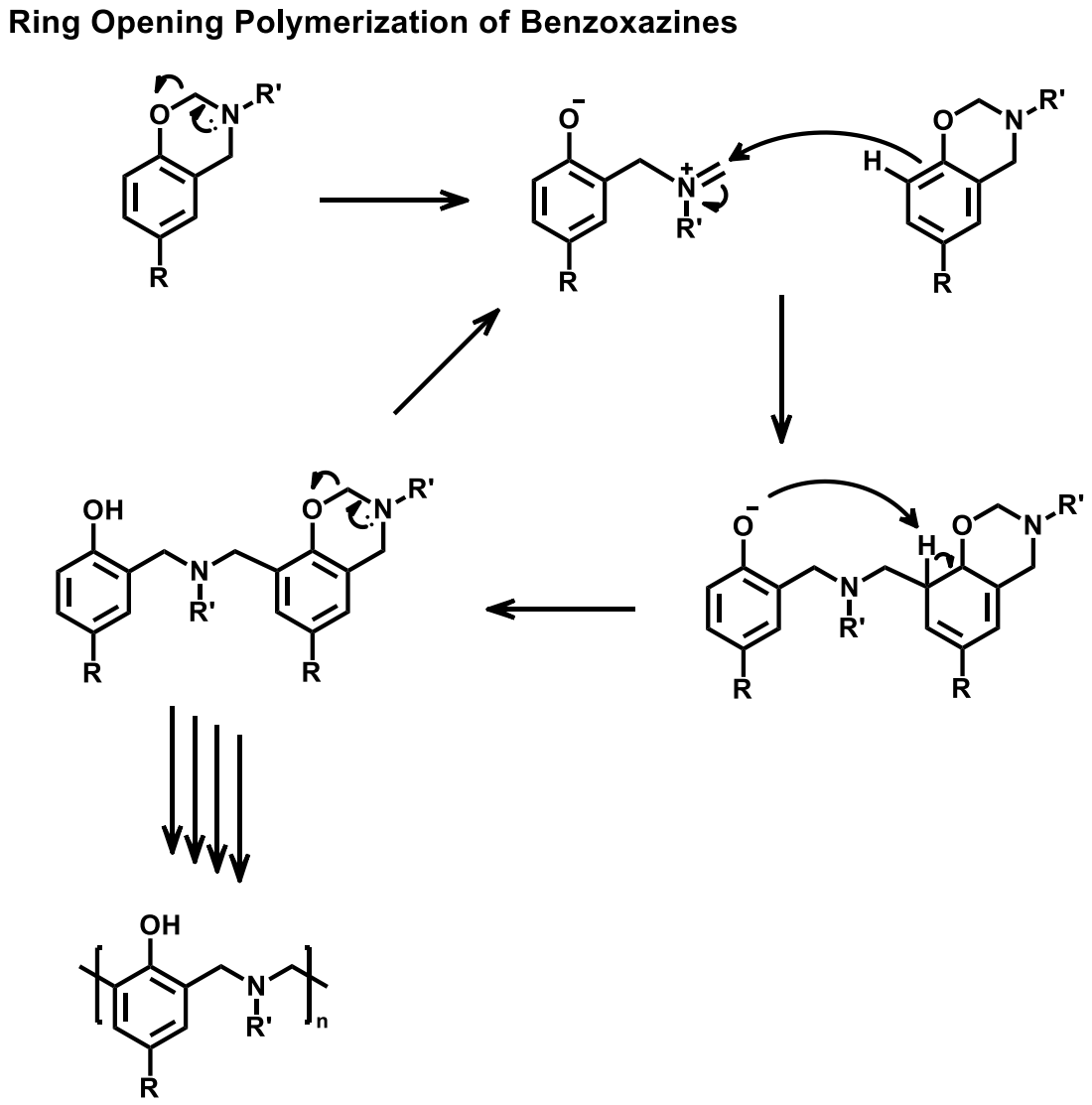

Scheme 1.7 Suggested cationic ring opening polymerization mechanism of benzoxazines

During this reaction, polymerization may take place at the *ortho* and *para* positions of the phenol. It has been demonstrated in the literature that the preferred reaction site during polymerization is the position *ortho* to the hydroxyl group of the phenol.[33,35] The initial reaction step produces an intermediate which provides electron

movement from the nitrogen atom to the hydroxyl group which is followed by nucleophilic aromatic substitution and proton abstraction.[44]

While monomer synthesis and subsequent polymerization of BOX is relatively straightforward, the processability of these monomers is often difficult. Multifunctional BOX monomers are typically glassy solid powders or highly viscous liquids at temperatures below 120 °C, thus limiting their processability. Currently, multifunctional BOX monomers blended with low viscosity epoxy reactive diluents are commercially available, but the desirable properties of BOX are significantly reduced by the high dilution of epoxies needed to achieve liquid physical states favorable for processing.[45]

Alternatively, research by *Ishida et al.* has focused on utilizing liquid monofunctional BOX monomers as reactive diluents to blend with glassy solid multifunctional benzoxazines yielding 100% BOX liquid alloys.[46–48] BOX liquid alloys show significantly reduced viscosity compared to their un-diluted state and the monofunctional reactive diluent will copolymerize with multifunctional BOX monomers upon heating. These studies conducted by *Ishida et al* have shown that this strategy has proven to be an effective method of reducing BOX monomer blend viscosity with negligible effects on network properties below the T_g. Alloying multiple BOX monomers with varying monomer architecture to tune network properties and enable processing shows promise to expand the applications of BOX networks.

Despite the pioneering results from these groups which have been able to improve the processability of BOX monomers, examples in the literature utilizing BOX alloys for AM, and specifically VPP, remain absent or severely limited. This is surprising, due to key advantages of BOX chemistries such as their modular synthesis, UV resistance, and

superior thermomechanical properties that make them exceptional candidates for a dual cure VPP AM approach. This dissertation aims to fill this gap in the literature by fundamentally studying BOX chemistries as potential candidates for VPP AM materials using a dual cure approach.

1.2 Research Motives

1.2.1 VPP of Dual-Cure Benzoxazine Networks (Chapter III)

While dual-cure strategies offer unique advantages for VPP AM, the bulk of research endeavors have focused on acrylate and epoxy or similar systems.[49] BOX based formulations are also an attractive choice as a secondary heat activated curing mechanism to prepare IPNs or HPNs. BOX networks are an emerging class of high-performance thermosets which offer high glass transition temperatures, dimensional and thermal stability, chemical and flame resistance, and limited water absorption.[50–52] A key advantage of BOX monomers for dual-cure networks are their simplistic and modular synthesis rooted in the Mannich condensation of a phenol, primary amine, and formaldehyde.[31] BOX chemistries also exhibit near-zero shrinkage during polymerization, high UV resistance, and do not release condensate upon polymerization, making BOX chemistries attractive candidates for application in dual-cure networks.[39,53–55] While BOX networks have been used with a variety of UV polymerizable chemistries to synthesize dual-cure networks,[29,56,57] the utility of such for VPP AM applications remains mostly unexplored.

This research combines photo and thermal polymerization techniques to create HPNs based on a monomer having both acrylic and BOX moieties in an SLA AM

application. Acrylate-functionalized BOX monomers are combined with a low viscosity monofunctional urethane acrylate reactive diluent (RD) to prepare formulations tailored to SLA 3D printing processes wherein viscosity and reaction rates are closely monitored. In the first stage, part geometry is established by free radical photopolymerization during the SLA AM process of the methacrylate functional BOX monomer (DMBOX) and the monofunctional acrylate RD 2-(((butylamino) carbonyl)oxy)ethyl ester (GEN 1122) in the presence of phosphine oxide-based photo initiator ethyl(2,4,6-trimethylbenzoyl) phenylphosphinate (TPO-L). In the second stage, the 3D printed part is heated to thermally polymerize unreacted BOX functional groups, creating covalent linkages within the formed part. The overarching goal is to demonstrate a new class of dual-cure BOX based materials for SLA AM, expanding the material base for the innovative manufacturing method.

1.2.2 Benzoxazine Alloys for Room Temperature VPP (Chapter IV)

As AM and SLA VPP continue to expand to new and challenging engineering applications, the demand for AM materials with improved engineering properties also increases. Recently, innovative efforts have been made towards facile, room temperature VPP AM of engineering materials such as polyimides,[58,59] polyether ether ketone (PEEK),[60] and epoxies.[61] These examples focus on a two-stage dual-cure approach, in the first step part geometry is set with a stimuli responsive binder and in the second stage part properties are driven by thermal post processing. This approach has resulted in significant material innovations for room-temperature VPP AM of high-performance polymers, benzoxazines remain un-explored in this field.

This research utilizes BOX monomers functionalized with photopolymerizable (meth)acrylate functional groups for SLA VPP AM. A viscous di-(meth)acrylate functional BOX monomer (DMBOX) is diluted with a low-viscosity monofunctional (meth)acrylate BOX monomer (MBOX) to prepare formulations tailored to SLA AM wherein viscosity and reaction kinetics are closely monitored and controlled. In the first stage, part geometry is established by free radical photopolymerization during SLA AM of the (meth)acrylate functional BOX monomers in the presence of phosphine oxide based photoinitiator TPO-L. In the second stage, the AM part is heated to thermally polymerize unreacted BOX functional groups within the formed part. The overarching goal of this research is to expand upon our previous research that demonstrated a new class of BOX materials for SLA AM. This research utilizes a dual-cure diluent in combination with a viscous di-functional dual-cure monomer, improving AM part thermomechanical properties while maintaining control of viscosity and photopolymerization rates.

1.2.3 Molecular Dynamics Simulations of Acrylate Networks (Chapter V)

Multi-functional acrylate or (meth)acrylate monomers used for coating or printing applications are often viscous, and thus difficult to process. A popular strategy to enable the processing of these monomers is by blending them with a low viscosity reactive diluent or comonomer to enable ease of processing. The choice of comonomer or reactive diluent can have a significant influence on the formulation viscosity, photopolymerization kinetics, and ultimately final crosslinked network properties.[62] Molecular dynamics (MD) simulations allow for the study of molecular level

characteristics of polymer networks and can aid in the understanding of how polymer network properties are impacted by the comonomer.[63] However, the lack of literature base utilizing MD simulations to study the free radical polymerization of acrylate and (meth)acrylate monomers has limited the application of MD simulations in the development of photopolymerizable formulations tailored for specific applications.

Our work aims to expand upon this literature base using MD simulations to model the photopolymerization and resulting network properties of a two-component photopolymerizable formulation. This study utilizes a DGEBA di-(meth)acrylate monomer, bisphenol A-glycidyl methacrylate (Bis GMA), blended with a mono-functional urethane acrylate reactive diluent, 2-[(butylcarbamoyl)oxy]ethyl acrylate (trade name Genomer 1122), and a Norrish type I acyl phosphine oxide based photoinitiator, TPO-L. Simulations utilized SMARTS patterns,[64] a language for substructure searching in a molecule, to model a photoinitiated free radical polymerization resulting in a crosslinked polymer network. Simulations of crosslinked structures are then studied as a function of increasing reactive diluent concentration to determine the resulting network properties. Simulation results are then compared to experimentally obtained values. The overall goal of this work is to demonstrate the application of MD simulations in the development of photopolymerizable formulations tailored for specific applications such as VPP AM.

CHAPTER II – Experimental

2.1 Materials

Bisphenol A (97+% Alfa Aesar), p-Cresol (99+% ACROS), 2-(2-aminoethoxy) ethanol (98%, ACROS), paraformaldehyde (90%, ACROS) triethylamine, (99%, pure, ACROS), methacryloyl chloride (95%, containing 200 ppm MEHQ as stabilizer, ACROS), xylenes, and dichloromethane were purchased from Fisher Scientific and used without further purification. For synthesized monomer purification, sodium hydroxide (NaOH) beads, anhydrous diethylether, and anhydrous magnesium sulfate ($MgSO_4$) were also purchased from Fisher Chemical Co. Monomers 2-(((butylamino) carbonyl)oxy)ethyl ester (GENOMER 1122) and bisphenol A diglycidyl ether dimethacrylate (EPOXY METHACRYLATE 97-053) as well as photoinitiator Ethyl(2,4,6-trimethylbenzoyl) phenylphosphinate (TPO-L) were generously donated by Rahn. UV absorber Tinuvin Carboprotect was generously donated by BASF.

2.2 Monomer Synthesis

2.2.1 Synthesis of Di-Hydroxy Functional Benzoxazine Monomer

In the first reaction step, bisphenol-A (11.4 g, 50.0 mmol), 2-(2-aminoethoxy) ethanol (11.0 g, 100 mmol), and paraformaldehyde (12.0 g, 800 mmol) were added to a 500 mL round bottom flask and dissolved in 120 mL of xylenes. The reaction mixture was heated to 120 °C in a preheated oil bath for 20 minutes. The crude reaction mixture was allowed to cool and then purged with N_2 overnight to remove solvent. Residual starting materials and phenolic impurities were removed by dissolving the concentrated reaction mixture in 120 mL of dichloromethane, extracting with 3M NaOH, and rinsing

with distilled water sequentially. Residual solvent was then removed under reduced pressure to obtain a clear viscous oil (10.5 g, 44% yield). The purified and dried product was characterized by ^{1}H NMR (600 MHz, Chloroform-d) δ 6.96 (dd, J = 8.6, 2.4 Hz, 1H), 6.81 (d, J = 2.4 Hz, 1H), 6.68 (d, J = 8.6 Hz, 1H), 4.86 (s, 2H), 4.01 (s, 2H), 3.73 – 3.68 (m, 4H), 3.61 – 3.59 (m, 2H), 3.00 (t, J = 5.4 Hz, 2H), 1.60 (s, 3H). The ^{1}H NMR spectra of di-hydroxy functional benzoxazine monomer is listed in Appendix A. ATR-FTIR characteristic benzoxazine peaks: 1498 cm^{-1} and 804 cm^{-1} assigned to the vibration of the tri-substituted benzene ring, 935 cm^{-1} out of plane C-H vibration of the benzene ring attached to the oxazine ring, 1213 cm^{-1} due to C-O-C asymmetric stretch of the oxazine ring.

2.2.2 Synthesis of Di-(meth)acrylate Functional Benzoxazine Monomer (DMBOX)

Di-hydroxy-functional benzoxazine monomer (10.0 g, 20 mmol) was re-dissolved in 120 mL of dichloromethane and cooled to 0 °C under N_2 atmosphere with magnetic stirring. Trimethylamine (6.3 mL, 45 mmol) followed by methacryloyl chloride (4.4 mL, 45 mmol) were then added to the sealed reaction mixture via syringe before warming the mixture to room temperature overnight. The crude mixture was filtered to remove TEA/HCl salt and washed with 1M NaOH and distilled water. Photoinhibitor, 0.01wt% of BHT, was added to the washed product prior to solvent removal via reduced pressure at 35 °C (rotovaporization). The product was then re-dissolved in diethyl ether and filtered to remove residual TEA/HCl salt and washed again with 1M NaOH and distilled water prior to solvent removal with reduced pressure at 35 °C to obtain a light-yellow oil. Structure of product was confirmed via ATR-FTIR and ^{1}H NMR (600 MHz, $CDCl_3$): δ

(ppm) = 6.93 (dd, J = 8.6, 2.4 Hz, 2H), 6.80 (d, J = 2.4 Hz, 2H), 6.65 (d, J = 8.5 Hz, 2H), 6.13 (s, 2H), 5.56 (s, 2H), 4.85 (s, 4H), 4.31 – 4.28 (m, 4H), 3.99 (s, 4H), 3.73 – 3.67 (m, 8H), 2.98 (t, J = 5.5 Hz, 4H), 1.95 (s, 6H), 1.58 (s, 6H). ATR-FTIR characteristic benzoxazine peaks: 1498 cm^{-1} and 804 cm^{-1} assigned to the vibration of the tri-substituted benzene ring, 935 cm^{-1} out of plane C-H vibration of the benzene ring attached to the oxazine ring, 1213 cm^{-1}due to C-O-C asymmetric stretch of the oxazine ring. Characteristic (meth)acrylate peaks: 1718 cm^{-1} carbonyl stretch, 1637 cm^{-1} assigned to the C=C stretching; in addition to these, there is a disappearance of the peak at 3400 cm^{-1} assigned to the hydroxyl stretching vibration.

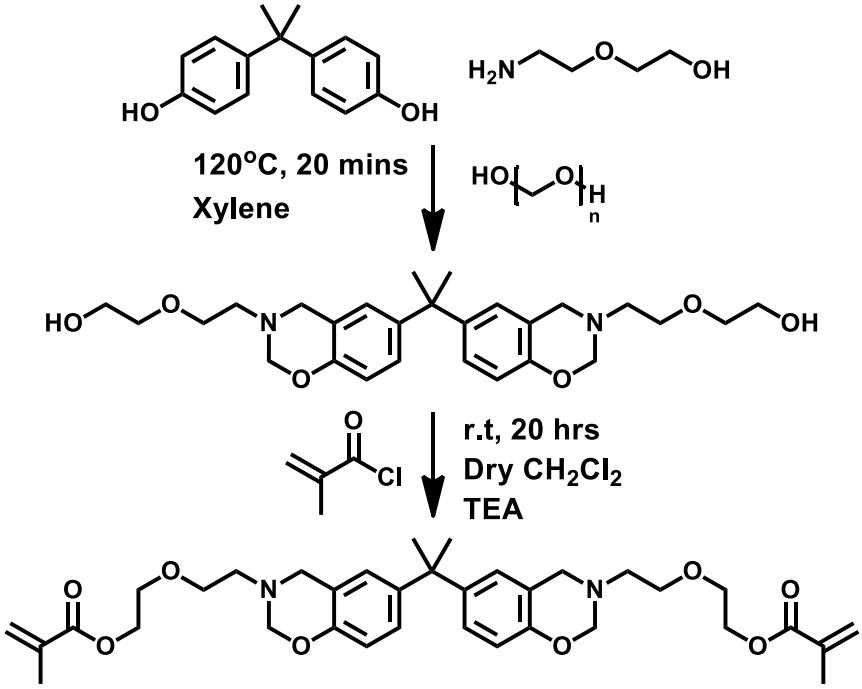

Scheme 2.1 Synthesis of Di-(meth)acrylate Functional Benzoxazine Monomer (DMBOX)

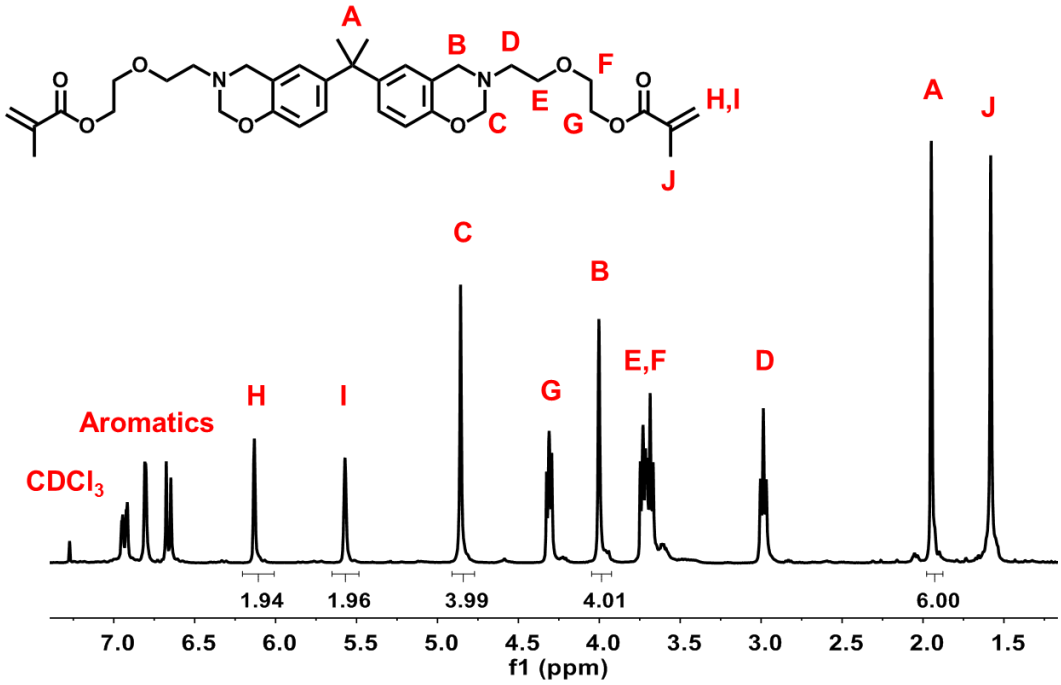

Figure 2.1 ^{1}H-NMR spectrum of DMBOX monomer

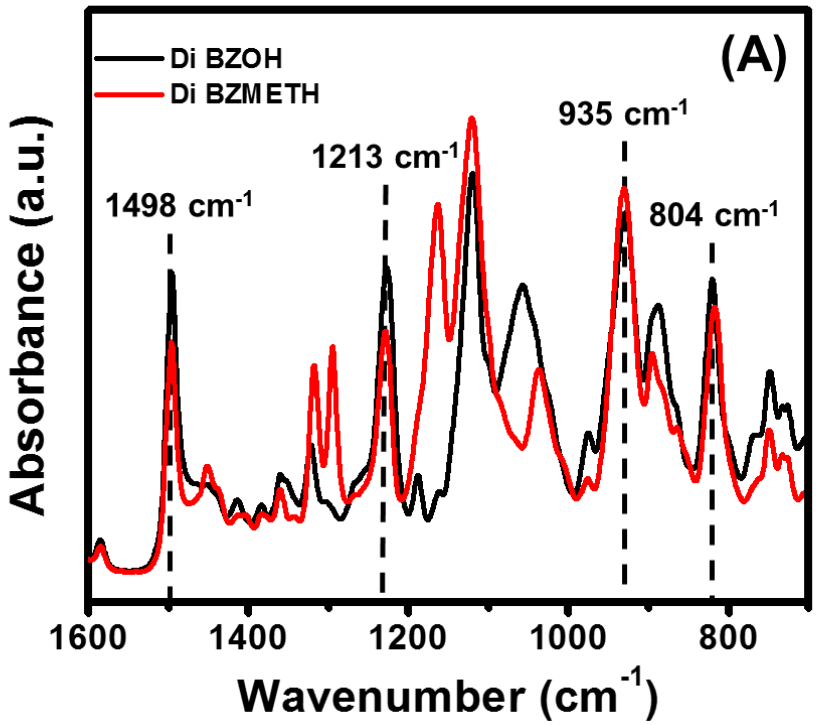

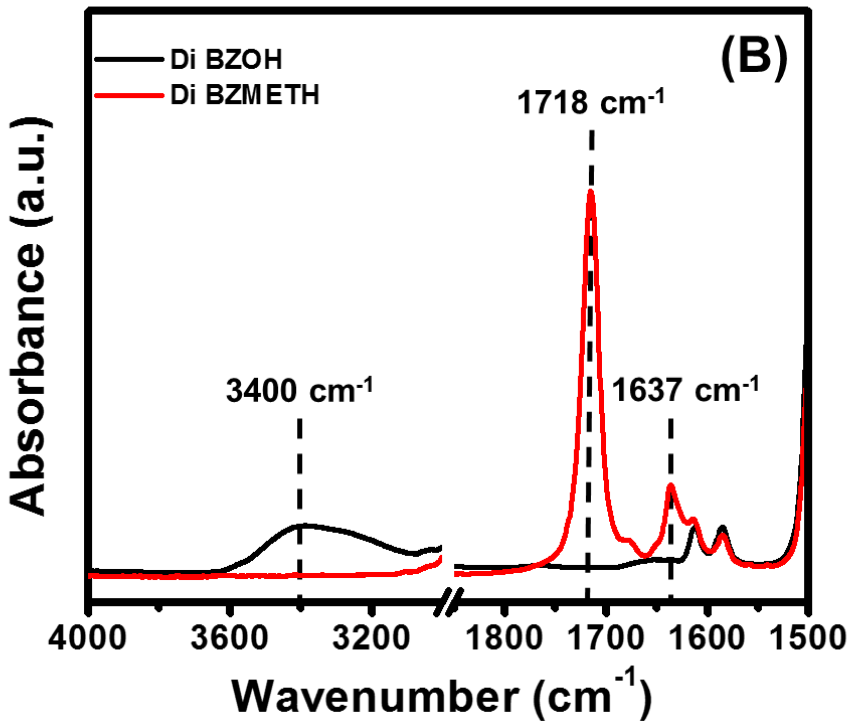

Figure 2.2 ATR-FTIR spectra of (A) di-hydroxy and di-(meth)acrylate functional characteristic BOX absorptions and (B) hydroxyl peak at 3400 cm^{-1}, carbonyl peak at 1718 cm^{-1}, and (meth)acrylate double bond peak at 1637 cm^{-1}.

2.2.3 Synthesis of Mono-Hydroxy Functional Benzoxazine Monomer

In the first reaction step, paraformaldehyde (5.0g, 167 mmol), 2-(2-aminoethoxy) ethanol (8.0g, 76 mmol), and p-cresol (8.0g, 74 mmol) were added to a 250 mL glass vessel equipped with an over-head electric mixer (Arrow Electric Mixer, Model 1750). The reaction vessel was then submerged in an oil bath and heated to 60°C with vigorous stirring for 20 minutes to achieve a homogenous reaction mixture in the absence of solvent. The temperature of the oil bath was then increased to 90 °C and the reaction was progressed for 90 min yielding a clear yellow oil. Residual starting materials and

phenolic impurities were removed by dissolving the reaction mixture in 120 mL of dichloromethane, extracting with 3M NaOH, and rinsing with distilled water sequentially. The purified monomer was then dried over magnesium sulfate and residual solvent was removed under reduced pressure. Structure of product was confirmed via ATR-FTIR and ^{1}H NMR (600 MHz, Chloroform-d) δ 6.93 (dd, J = 8.4, 2.2 Hz, 1H), 6.79 – 6.74 (m, 1H), 6.69 (d, J = 8.3 Hz, 1H), 4.86 (s, 2H), 4.01 (s, 2H), 3.74 – 3.71 (m, 2H), 3.68 (t, J = 5.3 Hz, 2H), 3.61 – 3.59 (m, 2H), 2.99 (t, J = 5.3 Hz, 2H), 2.25 (s, 3H). The ^{1}H NMR spectra of mono-hydroxy functional benzoxazine monomer is listed in Appendix A. ATR-FTIR characteristic benzoxazine peaks: 1498 cm^{-1} and 804 cm^{-1} assigned to the vibration of the tri-substituted benzene ring, 935 cm^{-1} out of plane C-H vibration of the benzene ring attached to the oxazine ring, 1213 cm^{-1} due to C-O-C asymmetric stretch of the oxazine ring.

2.2.4 Synthesis of (meth)acrylate Functional Benzoxazine Monomer (MBOX)

In the second reaction step, hydroxyl-functional benzoxazine monomer (10.0 g, 42 mmol) was re-dissolved in 120 mL dichloromethane and cooled to 0 °C under N_2 atmosphere with magnetic stirring. Triethylamine (6.3 mL, 45 mmol) followed by methacryloyl chloride (4.4 mL, 45 mmol) were then added to the sealed reaction mixture via syringe before warming the mixture to room temperature overnight. The crude mixture was filtered to remove TEA/HCl salt and washed with 1M NaOH and distilled water. Photoinhibitor, 0.01wt% of BHT, was added to the washed product prior to solvent removal via reduced pressure at 35 °C (rotovaporization). The product was then re-dissolved in diethyl ether and filtered to remove residual TEA/HCl salt and washed

again with 1M NaOH and distilled water prior to solvent removal with reduced pressure at 35 °C to obtain a green oil. Structure of product was confirmed via ATR-FTIR and ^{1}H NMR (600 MHz, Chloroform-d) δ 6.93 (dd, J = 8.3, 2.2 Hz, 1H), 6.79 – 6.74 (m, 1H), 6.72 – 6.66 (m, 1H), 6.17 – 6.14 (m, 1H), 5.61 – 5.57 (m, 1H), 4.87 (s, 2H), 4.33 (t, 2H), 4.03 (s, 2H), 3.77 – 3.72 (m, 2H), 3.70 (t, J = 5.5 Hz, 2H), 3.00 (t, J = 5.5 Hz, 2H), 2.26 (s, 3H), 1.97 (s, 3H). ATR-FTIR characteristic benzoxazine peaks: 1498 cm^{-1} and 804 cm^{-1} assigned to the vibration of the tri-substituted benzene ring, 935 cm^{-1} out of plane C-H vibration of the benzene ring attached to the oxazine ring, 1213 cm^{-1} due to C-O-C asymmetric stretch of the oxazine ring. Characteristic (meth)acrylate peaks: 1718 cm^{-1} carbonyl stretch, 1637 cm^{-1} assigned to the C=C stretching, in addition to these there is a disappearance of the peak at 3400 cm^{-1} assigned to the hydroxyl stretching vibration.

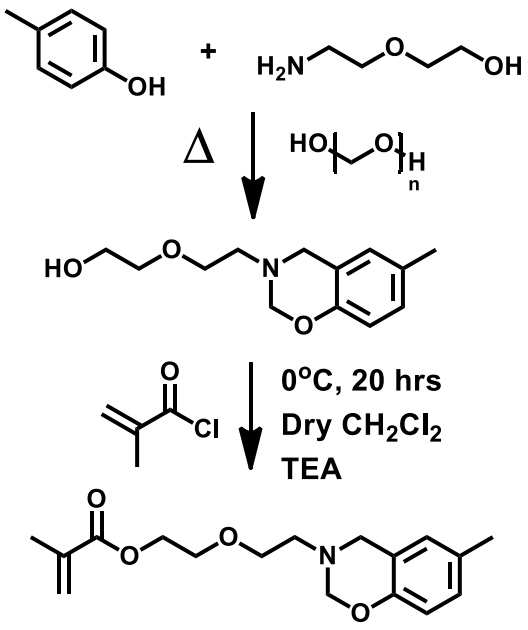

Scheme 2.2 Synthesis of Mono-(meth)acrylate Functional Benzoxazine Monomer (MBOX)

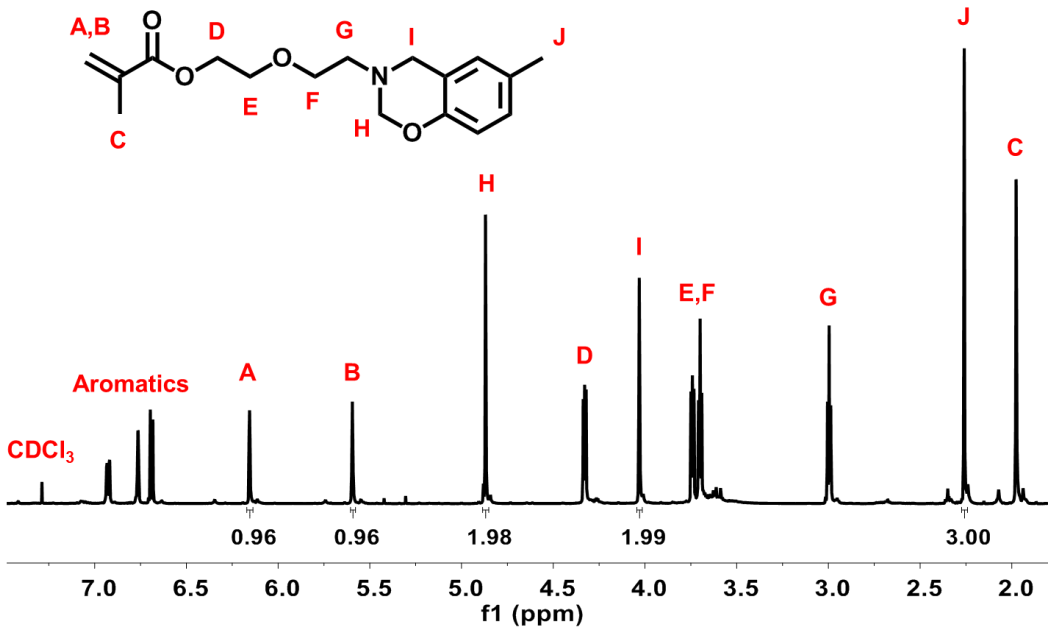

Figure 2.3 ^{1}H-NMR spectrum of MBOX monomer

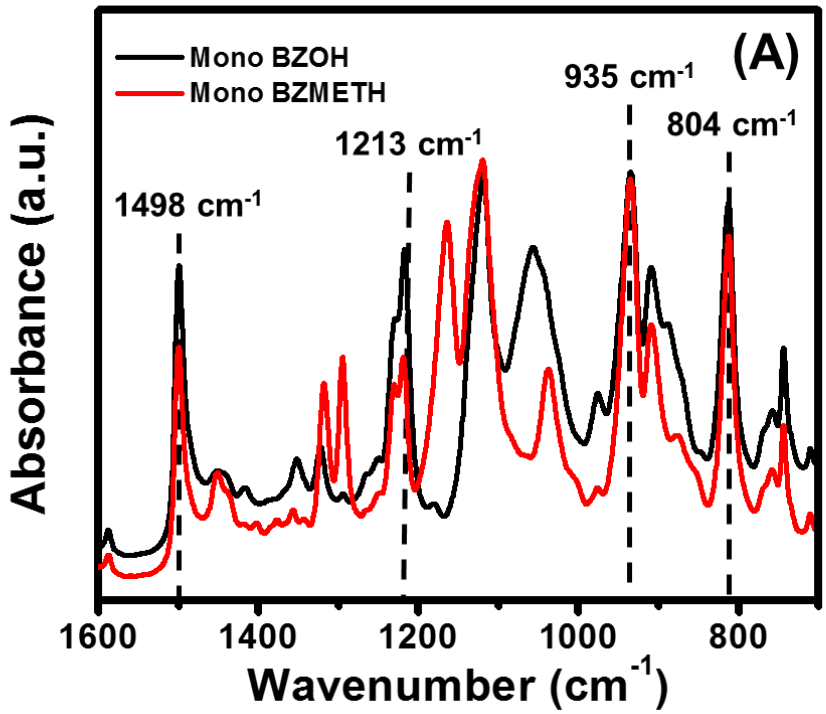

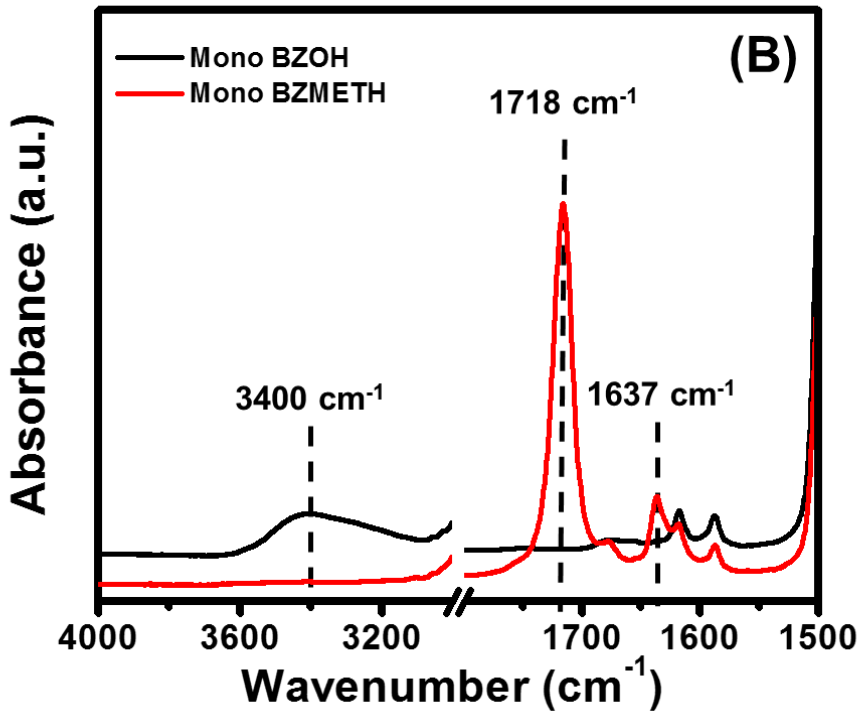

Figure 2.4 ATR-FTIR spectra of (A) mono-hydroxy and mono-(meth)acrylate functional characteristic BOX absorptions and (B) hydroxyl peak at 3400 cm^{-1}, carbonyl peak at 1718 cm^{-1}, and (meth)acrylate double bond peak at 1637 cm^{-1}

2.3 Formulation preparation and 3D Printing

All formulations were prepared for 3D printing by magnetic stir mixing of DMBOX monomer with MBOX and TPO-L photoinitiator at room temperature. A UV light absorber, (Tinuvin Carboprotect) was also added to formulations before 3D printing at 0.07 wt% to improve print resolution. Formulations are mixed with magnetic stirring under vacuum at room temperature before printing to avoid air bubbles. CAD models were designed in Solidworks® CAD software and prepared for printing using PreForm (FormLabs) software. Print files of test specimen were 3D printed using a commercially

available desktop SLA 3D printer (Form 2, FormLabs) equipped with a 250 mW laser having a 140 µm spot size. The Form 2 3D printer used in this research is shown in Figure 2.5, where the basic components of the SLA bottom up configuration are labeled. These components include the build platform where the printed part will be built, a material vat that holds the monomer or prepolymer blend to be processed, and the optically transparent window that allows for irradiation of the monomer blend to initiate polymerization.

Immediately after printing, samples were rinsed with isopropyl alcohol for 15 minutes to remove residual un-cured monomer from the printed sample. After solvent rinse to remove residual monomer, printed samples were removed from the solvent bath and dried in a forced air convection oven at 50 °C.

Printed samples are then thermally cured in a forced air convection oven. This research focuses on two thermal cure procedures, in Chapter three of this dissertation, BOX is thermally polymerized at 200 °C for increasing isothermal times. In the fourth chapter of this dissertation, BOX is thermally polymerized using a protocol of 100 °C for 30 minutes, 120 °C for 1 hr, 140 °C for 1 hr, 160 °C for 1 hr, and 180 °C for 2 hrs.

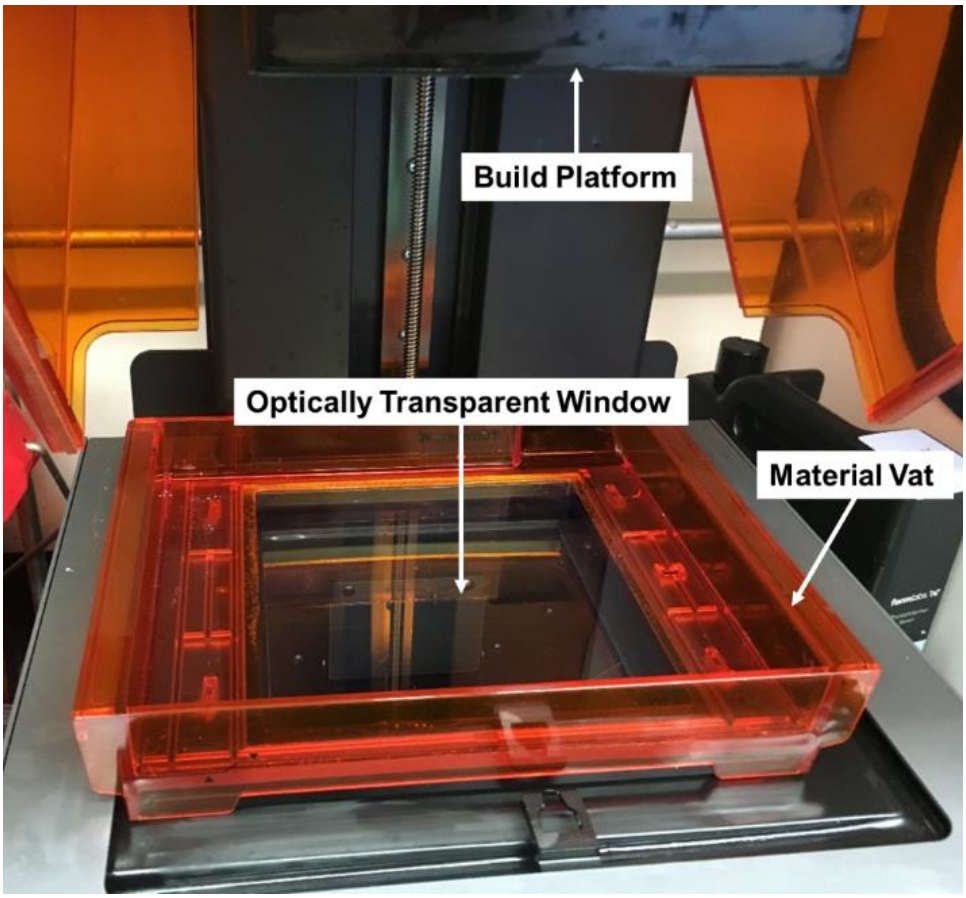

Figure 2.5 Form 2 SLA 3D Printer

2.4 Characterization

2.4.1 Proton Nuclear Magnetic Resonance Spectroscopy (^{1}H NMR)

Structures of the synthesized monomers were elucidated using ^{1}H NMR spectroscopy. Samples were dissolved in deuterated chloroform ($CDCl_3$) and a Varian Mercury Plus 600 MHz NMR spectrometer was used with tetramethylsilane added as an internal standard. Proton NMR spectra were acquired using 32 transients and a relaxation time of 5 s. For benzoxazine monomer characterizations via ^{1}H NMR, a singlet around

5.5 ppm and 4.5 ppm are representative of the protons on the two methylene linkages of the oxazine moiety (i.e. -O-CH2-N- and -N-CH2-Ar).

2.4.2 Rheological Experiments

Special care was taken to minimize sample light exposure prior to rheological experiments. All rheological experiments were carried out using a TA Instruments ARES-G2 rheometer.

Steady shear viscosity versus shear rate experiments were performed with a stainless steel 25 mm cone and plate geometry (0.1 rad) at 25 °C. Samples were pre-sheared at 10 s^{-1} prior to steady shear experiments to ensure homogeneous samples before monitoring steady state shear viscosity from 0.5 to 5 s^{-1}.

To investigate how the viscoelastic behavior of the acrylate and (meth)acrylate functional blends evolved upon light irradiation, photorheology was performed using an ARES-G2 rheometer equipped with a UV light guide accessory. UV intensity was calibrated at the sample location using an external radiometer. Unfiltered UV intensity was recorded as total intensity from 250 nm to 600 nm. Photorheology experiments were conducted by loading samples between an aluminum (bottom) and quartz (top) 20 mm diameter parallel plates with a sample thickness of 0.5 mm unless otherwise noted. Following a 15 s equilibration period, samples were irradiated by UV light at an intensity of 2 mW cm^{-2} unless otherwise noted from an unfiltered Omnicure S2000 UV light source via a fiber optic cable. Oscillatory shear experiments were conducted at room temperature, with an oscillatory strain within the linear viscoelastic regime. Exact strain values are reported with the results of photorheology experiments in each chapter. During

testing, automatic strain adjustment was employed at 10 Hz in "fast sampling" mode to resolve rheological behavior at fast cure speeds and to prevent over torque of the instrument.

Fourier transform mechanical spectroscopy (FTMS)[65] was also utilized during photorheology experiments where noted in order to estimate the gel point of samples by the Winter and Chambon criterion.[66] FTMS is based on the Boltzmann superposition principle, which states that multiple mechanical waves can simultaneously pass through a material independent of each other provided they stay within the linear viscoelastic regime. During FTMS experiments, a compound strain waveform is applied to the sample which allows for the simultaneously collection of G', G'', and tan delta data for multiple frequencies. Strain sweep experiments were conducted for each formulation tested by this method to ensure the compound strain signal amplitude remained within the viscoelastic range of the cured network. The compound waveform was calculated based on Equation (1):

$$\sum_{i=1}^{m} \gamma_i \sin(\omega_i t) \quad (1)$$

Where m is the number of frequencies in the compound waveform, γ_i, the amplitude of the ith component and ω_i is the frequency of the ith component, which is an integer multiple of the fundamental frequency ω and t is time.

The gel point of each sample is then estimated at the time which Tan Delta becomes independent of frequency. The critical relaxation exponent (n_c) of a given network was then calculated according to Equation (2).

$$n_c = \frac{2\delta}{\pi} \; ; \; \delta = \tan^{-1}\frac{G''}{G'} \quad (2)$$

2.4.3 Fourier Transform Infrared Spectroscopy

Real-time Fourier transform infrared monitoring (RT-FTIR) was performed to collect kinetic data for UV initiated free radical polymerization. Photopolymerizations were monitored using a Nicolet 8700 FTIR spectrometer having a KBr beam splitter and MCT/A detector. An OmicCure Exfo 1000 Series external light source provided filtered UV light in the range of 320−500 by way of a guided optical cable. After a 30 s rest period, samples were irradiated at 250 mW cm^{-2} for 5 min under nitrogen at ambient temperature while conversion of (meth)acrylate C=C double bond was monitored at 1637 cm^{-1}. Conversion of polybenzoxazine ring opening polymerization was monitored through the disappearance of the oxazine ring peak positioned at 931 cm^{-1}. Conversions were calculated by measuring the change in area under the (meth)acrylate C=C double bond peak at 1637 cm^{-1} and oxazine ring peak at 931 cm^{-1}.

Structural characterization and functional group analysis were carried out using attenuated total reflectance Fourier transform infrared spectroscopy (ATR-FTIR) where noted. Experiments utilizing ATR-FTIR were conducted using a PerkinElmer spectrometer with a KBr beam splitter and a DTGS detector where a total of four scans were collected to average the spectra for each sample. Samples for uncured formulations were taken as aliquots before printing and measurements taken on printed samples were taken from a portion of fractured DMA test specimen. The degree of cure (DOC)

achieved during the printing process was calculated by relating the absorbance of the double bonds to the aromatic absorbance using Equation (3):

$$DOC = \frac{\left(\frac{A_{1637}}{A_{1608}}\right)_{Un-Cured} - \left(\frac{A_{1637}}{A_{1608}}\right)_{Printed}}{\left(\frac{A_{1637}}{A_{1608}}\right)_{Un-Cured}} * 100 \quad (3)$$

Where A_{1637} represents the peak area associated with C=C stretching vibrations at 1637 cm^{-1} and A_{1608} represents the peak area of the aromatic absorption at 1608 cm^{-1}.

2.4.4 Thermogravimetric analysis

Thermal stability of 3D printed parts was determined via Thermogravimetric analysis (TGA) using a TA Instruments Q50 thermogravimetric analyzer with a platinum pan. Samples were heated at 20 °C/min from 25 °C to 600 °C under a nitrogen atmosphere. Mass loss was monitored as a function of temperature where temperatures at 5% and 10% weight loss were reported to monitor polymer network degradation.

2.4.5 Differential Scanning Calorimetry

Thermal polymerization of formulations was studied through differential scanning calorimetry (DSC) experiments. Experiments were conducted with a TA Q200 DSC using aliquots from formulations before printing for uncured samples and fractured DMA test specimen for printed samples with various thermal polymerization conditions. Samples were sealed in aluminum pans and heated from 10 °C to 300 °C at 10 °C/min under a nitrogen flow rate of 50 mL/min.

2.4.6 Dynamic Mechanical Analysis

Thermomechanical properties of printed rectangular bars were measured via dynamic mechanical analysis (DMA) using a TA Q800 DMA. Rectangular samples with dimensions 10 mm x 5 mm x 0.5 mm (length x width x thickness) were fixed in the instrument and tightened at 3 μNm torque and tested in tension mode with preload of 0.01 N and 0.05% oscillatory strain at 1 Hz frequency. Samples were equilibrated at -30 °C for two minutes before heating at 2 °C/min in air. Storage (E') and loss (E'') moduli were recorded as a function of temperature while Tan Delta was taken as a ratio of loss and storage moduli (E''/E'). Glass transition temperature was determined by the peak of the Tan Delta curve. The crosslink density (ν) of 3D printed parts was determined by storage modulus (E') values in the rubbery plateau according to Equation (4).[67,68]

$$\nu = \frac{E'}{3RT} \tag{4}$$

Where E' is obtained in the rubbery plateau, T is the temperature in K that corresponds to the E' value, and R is the universal gas constant.

Thermomechanical properties of photopolymerized films were studied during thermal polymerization using a TA Instruments ARES-G2 rheometer. Photopolymerized films from photorheology experiments were first quenched in liquid nitrogen to removed them from disposable quartz and aluminum plates. The 0.5 mm films were then loaded into the rheometer between 8 mm stainless steel disposable plates and trimmed to size. A normal force of 5 N was then applied with a 0.01% oscillatory strain at 1 Hz frequency.

Samples were then heated from 30 °C to 180 °C at 10 °C/min and held isothermally for 1 hr. Storage and loss moduli were recorded as a function of temperature while Tan Delta was taken as a ratio of G'' to G'. After isotherm, samples were cooled at 2 °C /min from 180 °C to 30 °C and the sample glass transition temperature was determined by the peak of the Tan Delta curve.

2.4.7 Mechanical Analysis

Uniaxial compression testing was conducted according to ASTM D695 using an MTS Systems Corporation Model 810 servo-hydraulic universal test frame equipped with a 10 kN load cell. Compression cylinders with a diameter of 5 mm and length of 10 mm were 3D printed and rinsed with isopropyl alcohol to remove unreacted monomer. The specimens were tested until failure at ambient conditions using a displacement-controlled test rate of 1 mm/min with a sampling rate of 10 Hz. A minimum of two specimens were tested and averaged to determine the Young's modulus at 2.5% strain.

2.5 Molecular Dynamics Simulation Methods

Molecular dynamics (MD) simulations were conducted using Schrödinger release 18-4 Materials Science Suite Maestro 2.9. Monomers were initialized randomly within the simulation box using the Disordered System Builder with the OPLS 2005 force field.[69–71] Each simulated system is composed of 200 monomers (~10,000 atoms), where the number of Bis GMA and UA monomers are systematically varied in order to allow us to study systems that closely match our experimental formulations. During initial placement of monomers, rotatable bonds are built inside the periodic cell using a self-

avoiding random walk algorithm that adjusts dihedrals and may re-grow part or all of a monomer, if necessary, to avoid contact with other monomers. Five simulation cells were built for each formulation to obtain statistical data of calculated cell properties. The resulting simulation cells were relaxed using the Materials Relaxation protocol within the Materials Science Suite. This protocol is composed of a 20 ps NVT Brownian dynamics step at 10 K, a 20 ps NPT Brownian dynamics step at 100 K, then a 100 ps NPT MD stage at 100 K. During this step, temperature was controlled by the Nose-Hoover thermostat and pressure was controlled with the Martyna-Tobias-Klein barostat. All MD simulations utilized a 2 fs time step unless otherwise noted.

Following the relaxation protocol, cells are further allowed to equilibrate during a 1.2 ns NPT MD stage at 300 K and a pressure of 1.01 bar. Cell density was monitored during the final equilibration to obtain a stable density before photopolymerization simulations.

2.5.1 Simulated Photopolymerization

After equilibrated cells reached a stable density, they were polymerized using the Crosslink Polymer builder within the Materials Science suite. A general photopolymerization is shown schematically in Scheme 2.3 where radicals are generated during photoinitiator decomposition and subsequently able to initiate monomer for chain growth polymerization. In order to define this free radical polymerization via SMARTS patterns, our simulations modeled this process using a fluorine atom. A fluorine atom was selected for this process due to its small size and the ability to distinguish it from other functional groups in the simulation cell. The SMARTS pattern used to describe a

phosphonyl radical was “[P][F]” while the carbon-carbon double bond in acrylate and methacrylate functional groups were defined as “[C;X3;H2]=[C;X3]”, see Figure 2.6. A carbon centered radical on an initiated monomer or growing polymer chain was defined as “[C][F]” which was then able to add across an acrylate or methacrylate double bond defined as “[C;X3;H2]=[C;X3]”. After crosslinking, fluorine was removed from the crosslinked cell and replaced with a hydrogen atom.

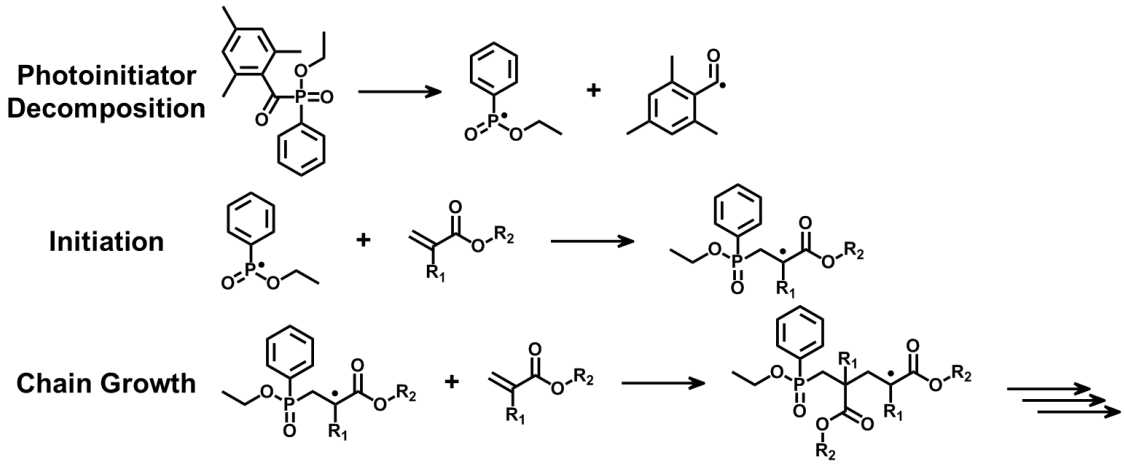

Scheme 2.3 General reaction scheme of a photoinitiated free radical polymerization

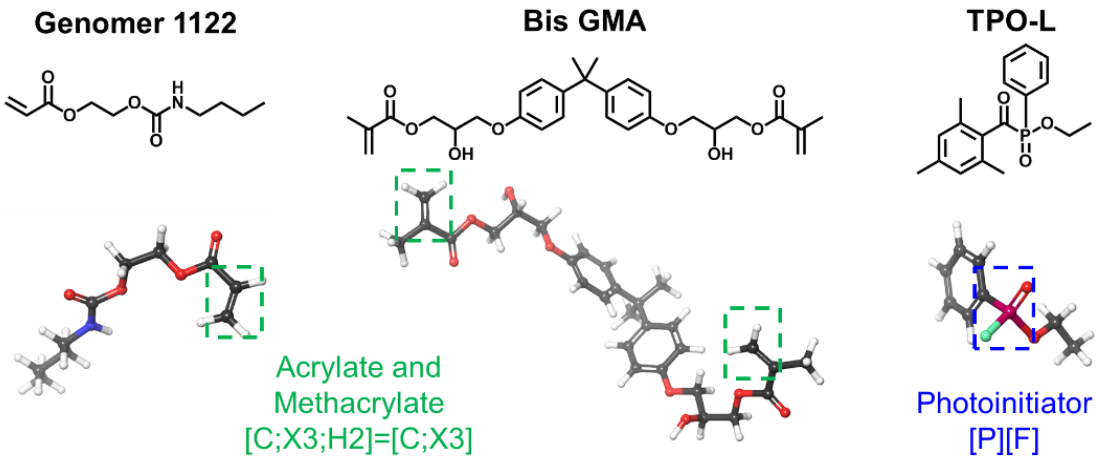

Figure 2.6 SMARTS Patterns used to define reactive sites during crosslinking simulations.

Within the Crosslink Polymer builder monomers were crosslinked iteratively where each reaction step and corresponding reaction site were defined using SMARTS patterns as discussed previously. A 50 ps NPT MD stage at 600 K and 1 atm was run after each bond forming iteration to allow newly formed bonds to relax and monomers to diffuse. The number of bonds formed per iteration was limited to five to reduce excessive strain during polymerization. The reaction threshold distance for each reaction step was set to 7 Å and a maximum of 20 unsuccessful crosslinking steps were allowed. The final target crosslink saturation of methacrylate crosslinking was set to 80%. The workflow of photopolymerization simulations is summarized in Figure 2.7.

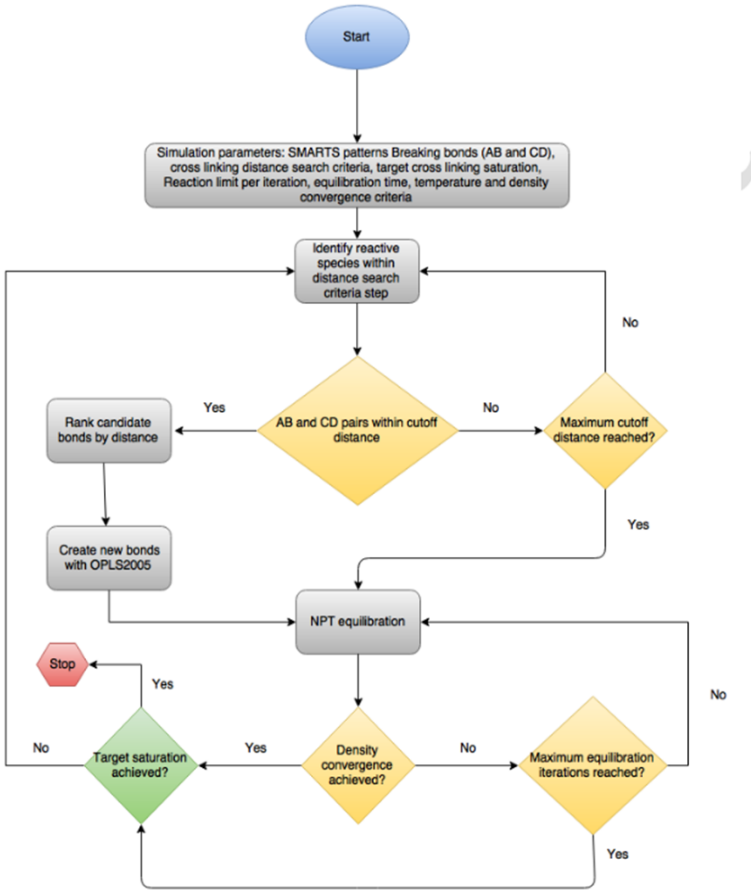

Figure 2.7 Simulated photopolymerization workflow[72]

2.5.2 Simulated Annealing

Crosslinked cell thermomechanical properties were calculated using the Thermophysical Properties module within Schrodinger's Materials Science. Within this module crosslinked cells are annealed from a temperature of 800 K to 150 K in steps of 15 K. This temperature range was selected to accurately capture both the glassy and rubbery behavior of the crosslinked cell before and after the glass transition. At each temperature, cells were simulated in an NPT ensemble for 5 ns per 15 K step to balance accurate T_g calculations and computational load.

Crosslinked cell density was calculated during this annealing process, which can then be plotted as a function of temperature during cooling. A maximum of 5 density simulations were run at each temperature to reach a density convergence. A hyperbolic curve may then be fit to the plot of density as a function of temperature and the T_g is taken as the intersection of the low and high temperature asymptotes of the hyperbola.

CHAPTER III - 3D Printing of Dual-Cure Benzoxazine Networks

3.1 Abstract

A novel 3D printing formulation based on a multifunctional benzoxazine (BOX) monomer possessing both photo and thermally polymerizable functional groups is reported. Printing formulation viscosity is readily tuned using a monofunctional-acrylate reactive diluent to enable SLA 3D printing. In the primary curing step, the printing formulation is UV cured by SLA 3D printing to prepare accurate parts on the millimeter size scale. The 3D printed parts are then heated in the secondary curing step to activate a thermally initiated BOX ring opening polymerization. Dynamic mechanical analysis demonstrated that the 3D printed parts exhibit a single Tan δ peak after both the primary UV cure and secondary thermal cure steps, suggesting the two polymerizations behave as one crosslinked network. The unique dual-cure strategy demonstrated in this research utilizes both photo and thermally initiated polymerizations to expand the library of materials available for high performance 3D printing applications.

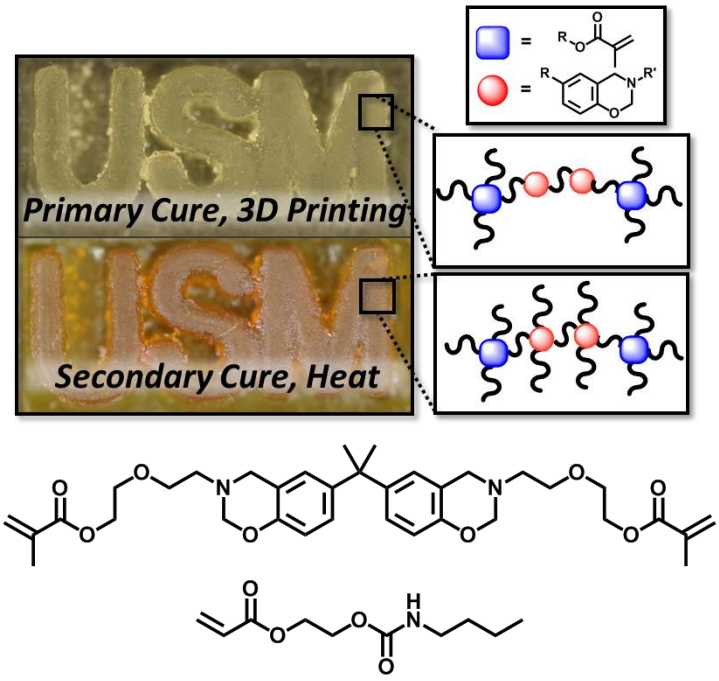

3.2 Results and Discussion

3.2.1 Printing Formulation Preparation and Rheological Characterization

Scheme 2.1 shows the overall synthetic scheme for the synthesis of di-(meth)acrylate functional BOX (DMBOX) monomer, which followed a two-step synthetic procedure previously established in the literature[25]. Synthesis of the di-hydroxy functional precursor was performed in xylenes at a temperature of 120 °C for 30 min. Xylenes was selected as the reaction solvent as it improved solubility of the reactants at elevated temperatures and its high boiling point favored oxazine ring closure by the removal of water, a condensation byproduct of BOX monomer synthesis, during the reaction. DMBOX was then synthesized by esterification of di-hydroxy functional BOX monomer using methacryloyl chloride and triethyl amine as a base catalyst to obtain a light-yellow viscous oil after purification. A detailed description of DMBOX monomer synthesis and monomer structure validation via ^{1}H-NMR and FTIR spectra are available in Section 2.2.

Viscous oil DMBOX was then blended with monofunctional urethane acrylate (Genomer 1122) as a reactive diluent. Genomer 1122 is a commercially available reactive diluent that is commonly formulated in VPP AM monomer blends due to its low viscosity, good reactivity, and flexibility.[73–78] Viscosity of DMBOX based blends are plotted as a function of reactive diluent loading levels as shown in Figure 3.1.

Viscosity data was collected using a rotational rheometer with a cone and plate geometry in air at ambient temperature while the shear rate was varied from 0.5 s^{-1} to 5 s^{-1}. The objective of this experiment was to establish viscosity data of DMBOX based blends at shear rates characteristic of the SLA 3D printing process. The DMBOX pure monomer viscosity initially is determined to be 190.4 Pa·s at a shear rate of 0.5^{-1} and decreases with increasing reactive diluent loading level, reaching 2.9 Pa·s at 40 wt% reactive diluent at the same shear rate. This trend of decreasing viscosity with increasing monofunctional urethane acrylate reactive diluent content is expected, as it is a less bulky molecule with a relatively lower viscosity compared to the DMBOX monomer.

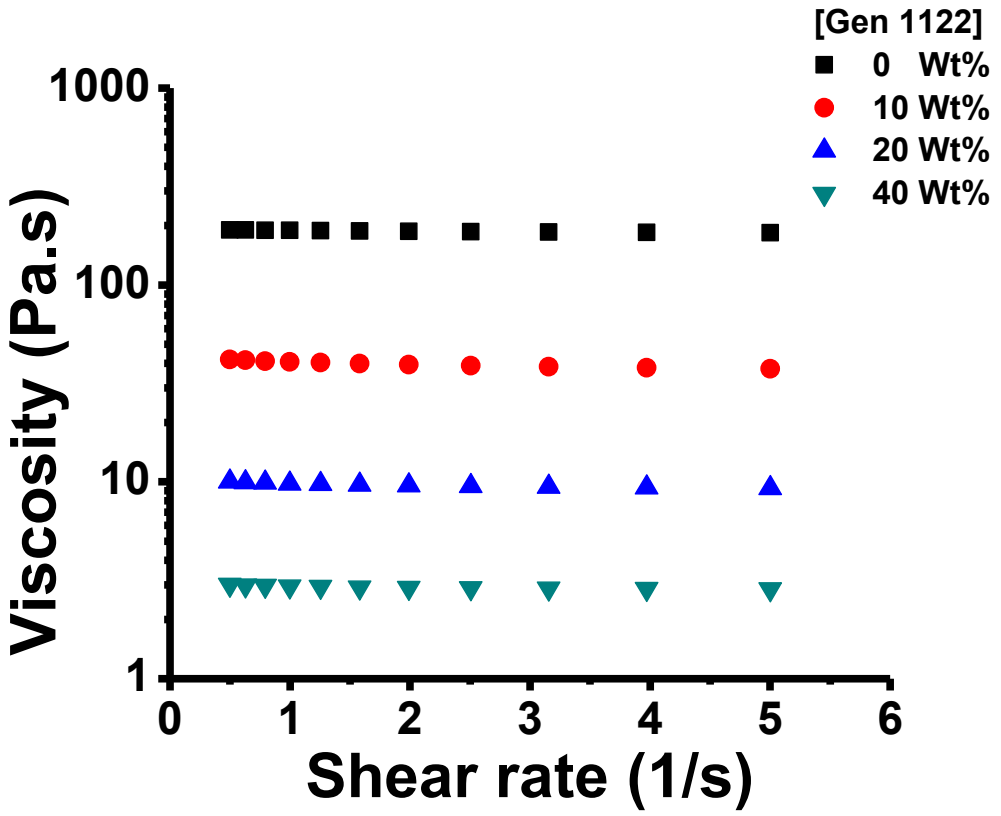

Figure 3.1 Plot of viscosity vs shear rate of DMBOX based blends

Using a similar SLA 3D printer to the Form 2 utilized in this study, Hasio and coworkers calculated the operating shear rate as the build platform moves into the bath of monomer to be approximately 1.7 s^{-1}.[79] Thus, to evaluate blend suitability for SLA 3D printing with increasing reactive diluent loading levels, a shear rate of 1.7 s^{-1} was utilized. Literature suggests viscosity of monomer or formulation should be ~5 Pa·s to be processable via vat photopolymerization 3D printing.[80,81] Above this practical upper viscosity target, monomer will not flow sufficiently to recoat the build platform evenly, leading to uneven layers and dimensional inaccuracy in the final part.

Figure 3.2 shows a plot of DMBOX based blend viscosities with increasing reactive diluent loading level at 1.7 s^{-1}. Blend viscosity at 1.7 s^{-1} is reduced from 187.9 Pa·s at 0 wt% reactive diluent to 2.9 Pa·s at 40 wt% reactive diluent. These results indicate that the viscosity of DMBOX blends may be readily tuned at shear rates characteristic of SLA AM according to the concentration of reactive diluent. Following this experiment, we will focus on a blend of 60 wt% DMBOX and 40 wt% reactive diluent (60:40 DMBOX:RD) as its viscosity is below the practical upper limit of 5 Pa·s and readily processable using SLA AM.

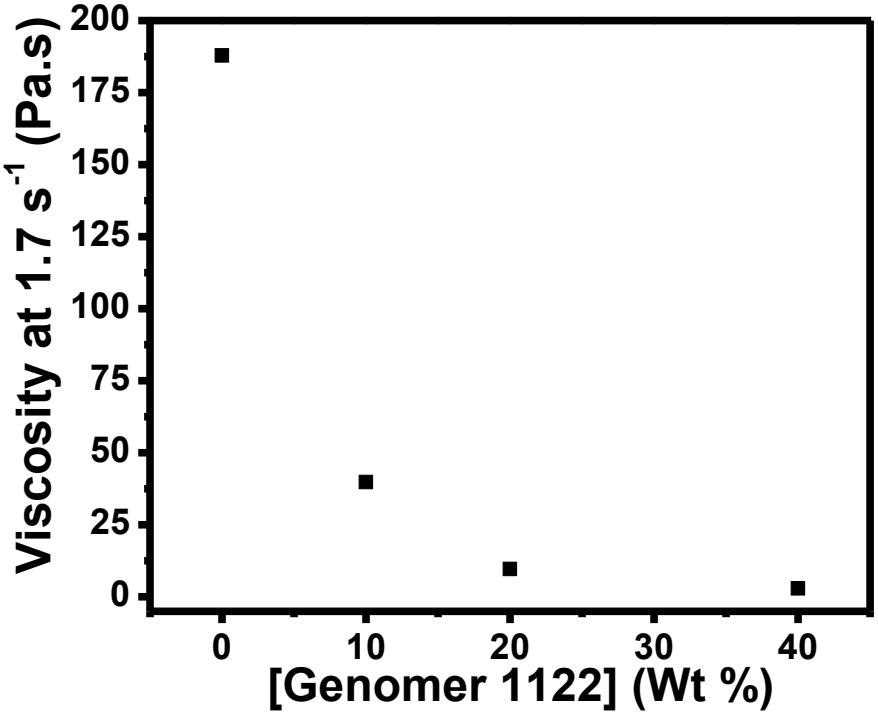

Figure 3.2 Plot of viscosities of DMBOX based blends at 1.7 s^{-1}

Figure 3.3 shows the storage (G') and loss (G'') moduli results of photorheology experiments studying 60:40 DMBOX:RD based blend as a function of photo initiator loading level under 5% oscillatory strain. The objective of photorheology experiments was to establish photopolymerization rates of DMBOX based blends at increasing photoinitiator concentrations. Results of these experiments were then used to guide appropriate photoinitiator concentrations to be used in blends for SLA AM.

The G'/G'' crossover point was used as an estimation of the gel point, where the sample transitions from a liquid to a gel upon network formation. While the gel point is generally determined when the loss tangent is independent of frequency in dynamic

measurement[82,83], the crossover point of storage and loss modulus is still often accepted to use in determination of gel points[84] and may be used to determine photopolymerization kinetics.

UV radiation is initiated 15 s after the start of the experiment where an increase in G' was observed for all samples, which indicates that the elastic property of samples was increased due to the photopolymerization of (meth)acrylate and acrylate functional groups in the samples. During the early stages of photopolymerization, G' was lower than G'', indicating the sample behaved as a viscous liquid. As photopolymerization continues, both G' and G'' increase as a function of irradiation time and eventually crossover, indicating gelation and a transition from viscous liquid to solid behavior.

Figure 3.4 plots time to the gel point after irradiation as a function of photoinitiator loading level. This plot shows rapid gelation in less than 5 seconds for all samples with a maximum in photo curing kinetics occurring at 1 wt% photoinitiator. Similar plateaued or reduced photopolymerization kinetics after a critical photoinitiator concentration have been reported in the literature.[58,80] Thus, to avoid radical coupling or

other chain termination events all future experiments were conducted using 1 wt% TPO-L.

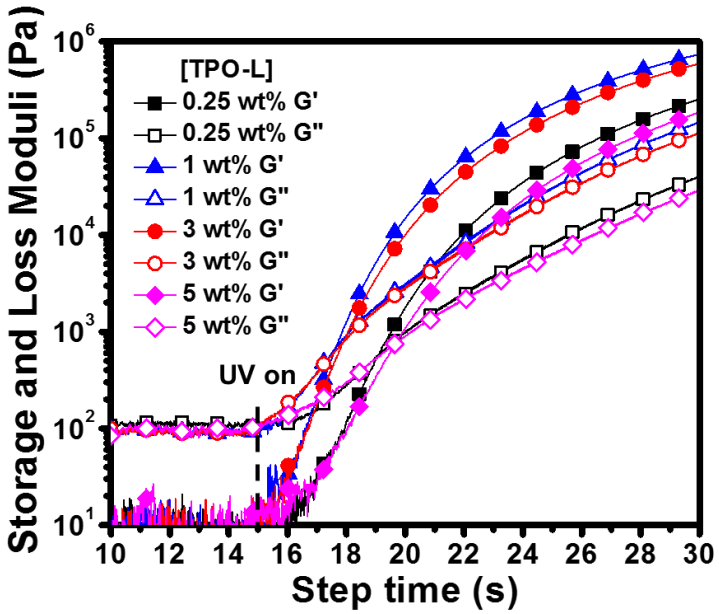

Figure 3.3 Storage (G') and loss (G'') moduli as a function of irradiation time with increasing [TPO-L] for 60:40 DMBOX:RD blend

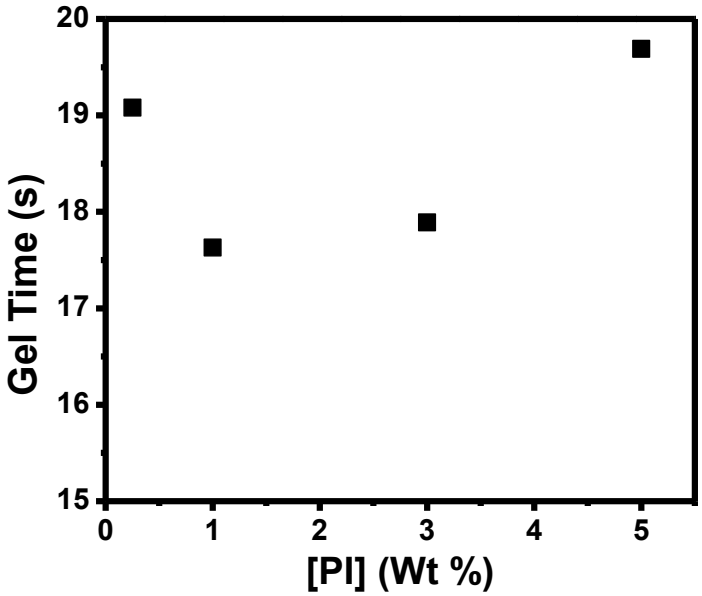

Figure 3.4 Gel time as a function of photoinitiator concentration for 60:40 DMBOX:RD blend

Another valuable approach to investigating the gel point of a crosslinking polymer is through the Winter-Chambon criteria.[85] Following this criterion, at the gel point G' and G'' follow the same power law dependency with respect to frequency and Tan Delta becomes independent of frequency:

$$G'(\omega) \sim G''(\omega) \sim \omega^n \tag{3}$$

$$\tan\delta = \frac{G''}{G'} = \tan\left(\frac{n\pi}{2}\right) \tag{4}$$

Where *n* is equal to the critical relaxation exponent of the polymer network at the gel point.[83] The *n* value of a given network at the critical gel point is able to give valuable information about the linear viscoelasticity at the critical gel where soft critical gels have large n values approaching 1 and stiff critical gels have low n values approaching 0.[86] In order to accurately determine the point of moduli frequency independence for a given network, dynamic mechanical measurements at constant frequencies for a range of frequency values would be required. This is a notoriously difficult characterization due to the transient nature of the polymer network during crosslinking and would typically require a new sample to be prepared for each frequency.

The most convenient characterization technique to aid in determining the gel point via the Winter-Chambon criteria is through the use of Fourier transform mechanical spectroscopy (FTMS).[65] This multiwave oscillatory time sweep measurement allows for a compound waveform to be applied to the sample such that multiple frequencies may be measured simultaneously as the polymer network evolves with time.[87] Results of FTMS

experiments studying 60:40 DMBOX:RD blend with 1 wt% TPO-L at 5, 10, and 15 Hz are depicted in Figure 1.12. During FTMS experiments, an applied oscillatory strain of 0.3% was used with a 0.5 mm gap. Samples were irradiated after 15 s, where after irradiation Tan Delta becomes independent of frequency at 21.7 s, indicating gelation. Additionally, using Equation (1) and the Tan Delta value at frequency independence, *n* was found to be equal to 0.78 for the photopolymerized 60:40 DMBOX:RD critical gel.

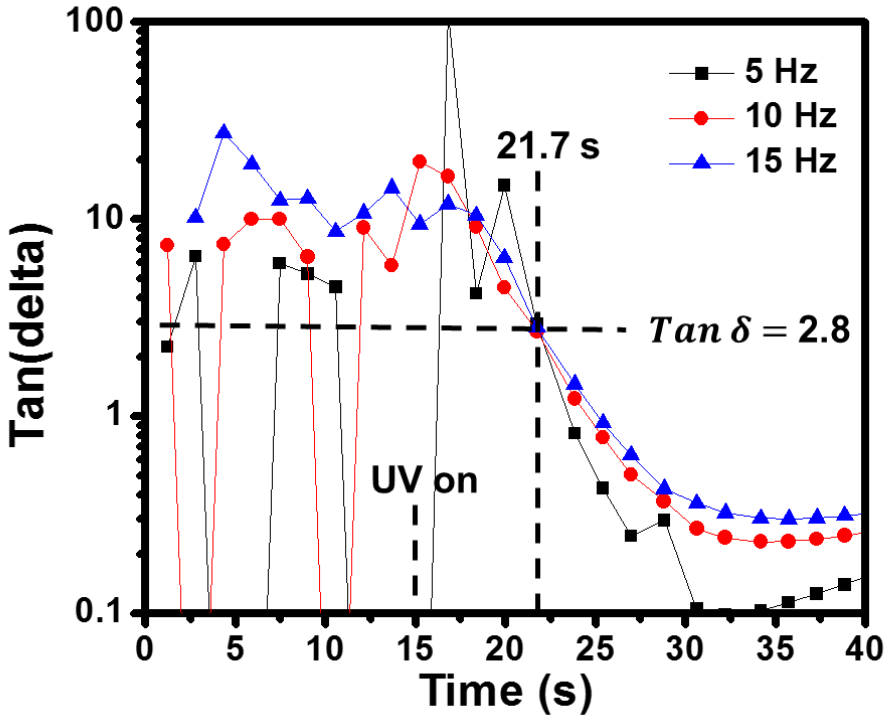

Figure 3.5 Tan Delta measured as a function of irradiation time for 60:40 DMBOX:RD blend with 1 wt% TPO-L

Figure 3.6 shows results of photorheology experiments studying photopolymerization rate of DMBOX:RD blends as a function of DMBOX concentration

with 1 wt% TPO-L photoinitiator. Before irradiation, samples exhibit liquid like behavior where the viscous modulus, G'' is greater than the elastic modulus, G'. Initially, samples follow a trend of increasing G'' with increasing DMBOX concentration, this trend may be explained by an increase in monomer blend viscosity as DMBOX concentration; is increased. This result correlates well with flow sweep experiments discussed previously, where increasing concentration of the relatively bulky and higher molecular weight DMBOX monomer resulted in an increased blend viscosity.

Upon irradiation, free radical polymerization is initiated and both G' and G'' increase as a function of reaction time and eventually cross over, indicating a transition from liquid-like to solid-like behavior. After G' / G'' crossover, G' continues to increase before reaching a final plateau, as expected upon the formation of a crosslinked network. Final G' plateau values of photopolymerized networks increase with increasing DMBOX concentration due to an increase in crosslink density with increasing DMBOX monomer concentration.

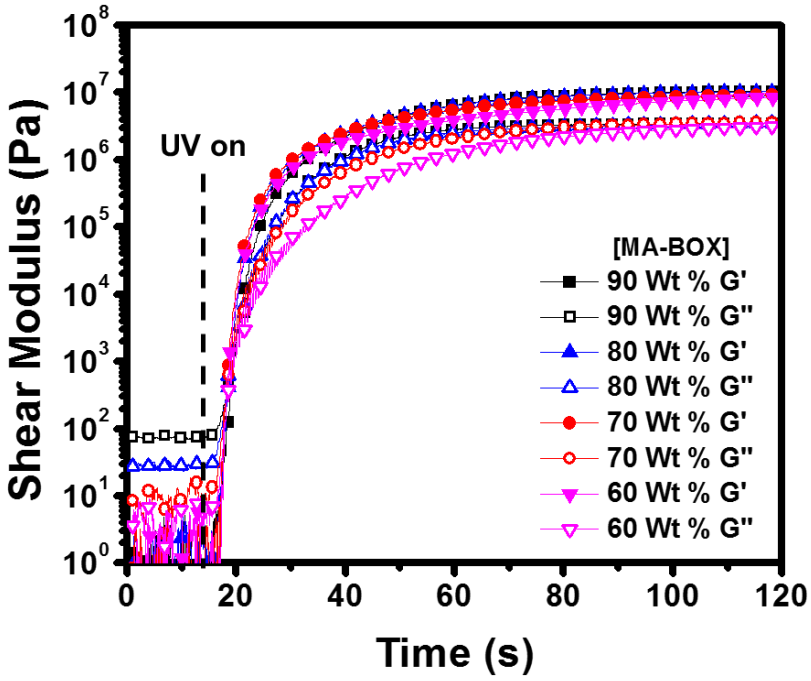

Figure 3.6 Shear storage and loss modulus of 3D printing formulations with 1 wt% TPO-L and increasing DMBOX concentration as a function of irradiation time

Table 3.1 Photorheology of 3D printing formulations with 1 wt% TPO-L and increasing DMBOX concentration

DMBOX Mol%	Initial G'' (Pa)	Initial Complex Viscosity (Pa·s)	G' / G'' Crossover (s)	Final G' (10^6 Pa)
90	74.8	12.1	20.1	10.6
80	27.5	4.4	18.8	10.3
70	9.64	1.4	17.9	9.2
60	5.29	0.79	18.0	8.4

During photopolymerization intermolecular distance between monomers is reduced by the conversion of van der Waals forces between monomers into covalent bonds.[88] This well studied phenomenon results in an overall volume reduction during

photopolymerization which can lead to internal stress in a photopolymerized network.[89,90] The relative volume reduction, or shrinkage, during photopolymerization of BOX blends was studied during photorheology experiments by monitoring the evolution of normal force during irradiation.

Figure 3.7 plots axial force as a function of irradiation time studying BOX blends with increasing DMBOX concentration. The onset of normal force buildup for each BOX blend corresponds well with the gel point as monitored by G', G'' crossover at ~ 18 s. As the relatively high molecular weight DMBOX monomer concentration is increased, the rate of shrinkage as measured by axial force is reduced. Similar results have been observed in the literature where increasing the concentration of a relatively low molecular weight reactive diluent increases shrinkage during photopolymerization.[91] This trend has been explained as an increase in the concentration of reactive C=C double bonds available as the concentration of a relatively low molecular weight reactive diluent is increased.[92] Thus, while increasing reactive diluent concentration readily decreases the viscosity of BOX blends, it results in an overall increase in shrinkage during photopolymerization. This is an important consideration, as shrinkage upon photopolymerization may result in cure induced strain or dimensional accuracy in the printed structure.

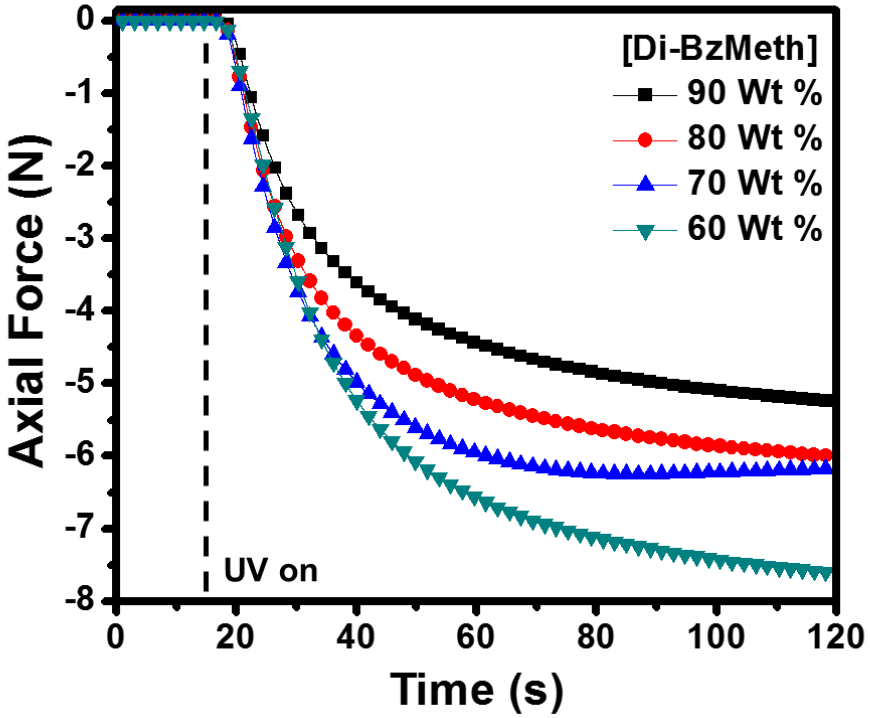

Figure 3.7 Axial force as a function of irradiation time for BOX blends with 1 wt% TPO-L and increasing DMBOX concentration as a function of irradiation time

3.2.2 Thermal Stability of Printed Parts

TGA was performed to investigate the thermal stability of 60:40 DMBOX:RD blend after each stage of polymerization. TGA experiments studied the un-cured monomer blend, parts photopolymerized during SLA AM, and dual-cured samples that have been photopolymerized and thermally treated to activate BOX polymerization. TGA weight loss profiles are shown in Figure 3.8 and decomposition temperatures are summarized in Table 3.2.

TGA results indicated that the initial degradation temperatures ($T_{5\%}$ and $T_{10\%}$) for un-cured 60:40 DMBOX:RD blends are 155 °C and 175 °C respectively. Both the $T_{5\%}$

and $T_{10\%}$ temperatures of samples increased significantly after free radical photopolymerization during SLA AM to 277 °C and 303 °C respectively. These initial degradation temperatures are consistent with reports in the literature studying the thermal degradation of poly(methyl methacrylate) networks.[93] Interestingly, The $T_{5\%}$ and $T_{10\%}$ degradation temperatures of photopolymerized samples after thermal polymerization of BOX at 200 °C for 1 hr only slightly increased to 285 °C and 307 °C respectively.

The similar thermal degradation behavior between photopolymerized samples and dual-cured samples may be explained by similar thermal initiation temperatures of poly(methyl methacrylate) network degradation and onset of BOX network degradation. Mannich base cleavage is known to initiate thermal degradation of polybenzoxazine networks derived from aliphatic amines in the temperature range of 260-300 °C.[38] In addition to Mannich base cleavage, another explanation for the similar thermal stabilities of photopolymerized samples and dual-cured samples could be thermally initiated polymerization of BOX taking place during the temperature ramp. After initial degradation, weight loss profiles for all samples also show a second thermal degradation step at 400 °C. This second stage of degradation near 400 °C is attributed to thermal decomposition of main-chain polymer chains and substituted phenolic units.[38]

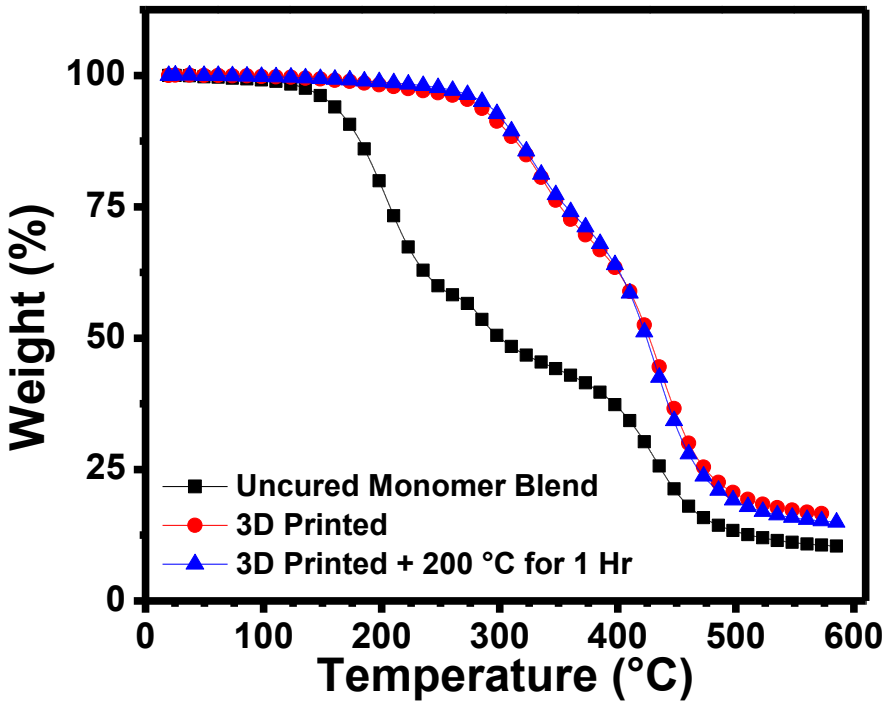

Figure 3.8 weight loss profiles of 60:40 DMBOX:RD un-cured monomer blend, 3D printed networks, and 3D printed networks with secondary cure at 200 °C for 1 hr

Table 3.2 Decomposition temperatures of 60:40 DMBOX:RD un-cured monomer blend, 3D printed networks, and 3D printed networks with secondary cure at 200 °C for 1 hr.

Sample	**$T_{5\%}$ (°C)**	**$T_{10\%}$ (°C)**
Un-Cured Monomer Blend	155	175
3D Printed	277	303
3D Printed + Thermal Cure	285	307

Figure 3.9 depicts isothermal TGA results investigating weight loss as a function of time for photopolymerized 60:40 DMBOX:RD samples at 200 °C: Samples were first ramped at 20 °C/min from ambient temperature to the isotherm temperature of 200 °C where they were held isothermally for 3 hrs. Samples exhibit a weight loss of 3.85 wt% during a 20 °C/min ramp from ambient temperature to 200 °C before reaching a stable degradation rate of 0.03 wt %/min and a final weight loss of 9.74 wt% after 3 hrs. These experiments may be compared to the thermal degradation behavior or volatilization of BOX monomers during BOX polymerization as reported in the literature.[94–96] A weight loss range of 1.6 – 8.5 wt% at 180 °C after 3 hrs depending on the substituent attached to the oxazine ring has been reported for bisphenol A based BOX monomers.[94] This is in contrast to 3D printed 60:40 DMBOX:RD monomer blend studied during isothermal TGA experiments which exhibited a final weight loss of 9.74 wt% after 3 hrs at 200 °C.

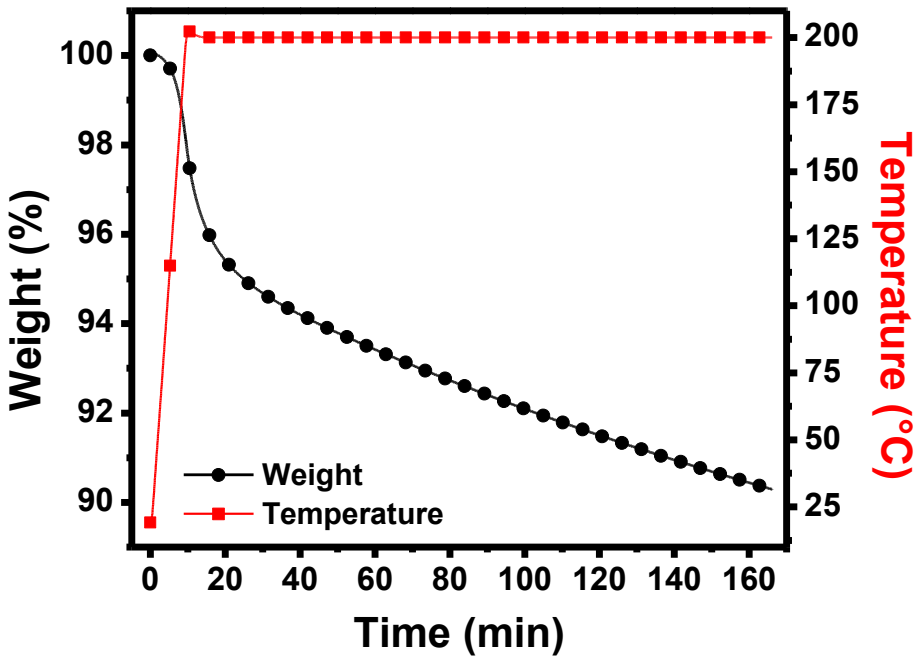

Figure 3.9 3D printed 60:40 DMBOX:RD blend held isothermally at 200 °C for 150 min

3.2.3 DSC Studies of Primary and Secondary Cure

Thermal polymerization behavior of 60:40 DMBOX:RD formulation was studied using DSC. The DSC thermograms of un-cured monomer blend, samples photopolymerized during SLA AM, and photopolymerized samples with a thermal cure at 200 °C are presented in Figure 3.10. DSC of un-cured monomer blend showed two exothermic peaks at 145 °C (onset 112 °C) and 244 °C (onset 193 °C), attributed to the thermal polymerization of acrylate and benzoxazine functional groups, respectively,[29,31] exhibiting heats of polymerization of 73 J/g and 176 J/g respectively .

Samples that have been free radically polymerized by UV radiation during 3D printing showed only one exothermic peak with an onset at 213 °C and a peak maximum at 247 °C, indicating that acrylate and (meth)acrylate functional groups were polymerized by UV radiation during the 3D printing process. The increased onset and peak temperatures of BOX ring opening polymerization exotherm observed in samples after photopolymerization of acrylate functional groups during 3D printing is attributed to restricted mobility due to the UV-cured network.[29] With increasing heating time at 200 °C, the residual heat of polymerization of the benzoxazine ring opening polymerization exotherm decreases to 99, 69, 19, and 2 J/g for 0, 30, 60, and 90 minute heating time, respectively. The absence of the exothermic peak at 145 °C suggests high conversion of acrylate and (meth)acrylate functional groups by UV radiation, while the significant reduction in heat of polymerization at the high temperature exothermic peak at 244 °C suggests high conversion of thermally initiated BOX polymerization.

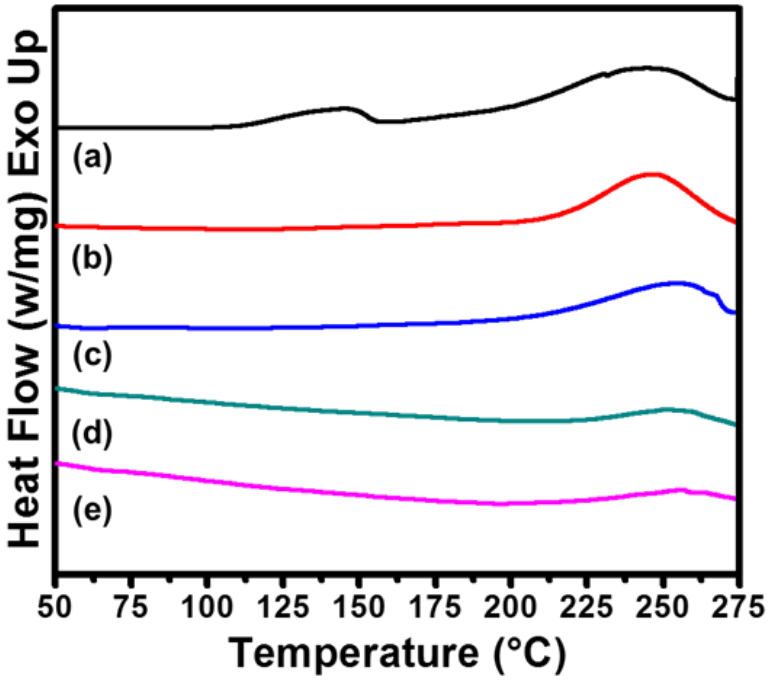

Figure 3.10 DSC thermograms for (a) un-cured 60:40 DMBOX:RD monomer blend, (b) after 3D printing, and after thermal treatment at 200 °C for (c) 30 (b) 60 and (e) 90 minutes

3.2.4 Spectroscopic Studies of Primary and Secondary Cure

ATR-FTIR spectroscopy was utilized to further investigate both the UV and thermally initiated polymerizations in our dual-cure DMBOX-based formulations. ATR-FTIR results are shown in Figure 3.11, where neat un-reacted 60:40 DMBOX:RD monomer blend shows peaks representative of both photo and thermally reactive functionality wherein the photo-polymerizable methacrylate alkene is assigned at 1637 cm^{-1} and the benzene ring which is attached on the oxazine ring is assigned at 931 cm^{-1}.[29,97] To thermally polymerize the unreacted BOX present after SLA AM, a cure protocol of 200 °C for 1 hr was selected. The temperature of 200 °C was found to be above the

onset temperature of the BOX polymerization exotherm observed in DSC experiments discussed previously. The peak at 1637 cm^{-1} associated with the methacrylate double bond is absent after photopolymerization during SLA AM as expected, while the BOX associated peak at 931 cm^{-1} is still present. The BOX-related peak at 931 cm^{-1} does show a slight reduction in intensity as compared to the uncured monomer blend. This result agrees with the reduced heat of polymerization in the BOX exothermic peak after 3D printing observed in DSC experiments. Following a 1-hr thermal cure of the 3D printed part at 200 °C acrylate, (meth)acrylate, and BOX polymerizations completed conversion as observed by the absence of both the peak at 1637 cm^{-1} and the peak at 931 cm^{-1}.

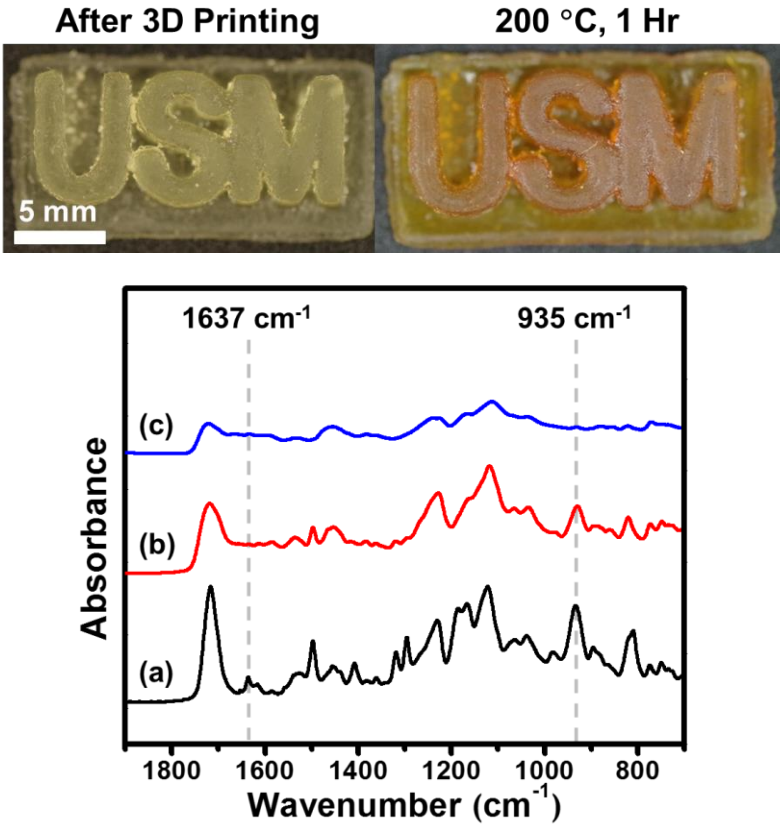

Figure 3.11 Images of 3D printed parts and ATR-FTIR spectra of 60:40 DMBOX:RD formulation before printing (a), after 3D printing (b), and after 1-hr at 200 °C (c)

Real-time FTIR (RT-FTIR) was used to monitor the kinetics of UV initiated free radical polymerization and thermally initiated ring opening BOX polymerization of 60:40 DMBOX:RD blend. Figure 3.12 shows the results of RT-FTIR experiments where polymerization conversion is plotted as a function of time for 60:40 DMBOX:RD blend with 1 wt% TPO-L. This photoinitiator loading level was selected based on photorheology results where it was found that this loading level maximized photopolymerization kinetics as discussed in Section 3.1. During this experiment, samples were sandwiched between two NaCl plates followed by irradiation with unfiltered UV light for 5 minutes. UV-polymerizable methacrylate alkene peak positioned at 1637 cm^{-1} was used to monitor UV polymerization and the BOX-related peak positioned at 931 cm^{-1} was used to monitor thermal polymerization as described previously.

RT-FTIR results show no conversion of methacrylate polymerization until samples are irradiated, upon which full conversion is reached in less than 2 minutes, indicating rapid photopolymerization kinetics. After UV irradiation, the peak at 931 cm^{-1} representative of the BOX oxazine ring shows near 10% conversion which is consistent with results from Ishida et al.[29] Photopolymerized samples were then transferred to a heated cell where samples were heated to 200 °C, which was found to be the onset temperature of BOX ring opening polymerization during DSC experiments. Thermally initiated ring opening polymerization of BOX shows relatively slower kinetics as compared to UV initiated free radical polymerization reaching 98% conversion after 50 min.

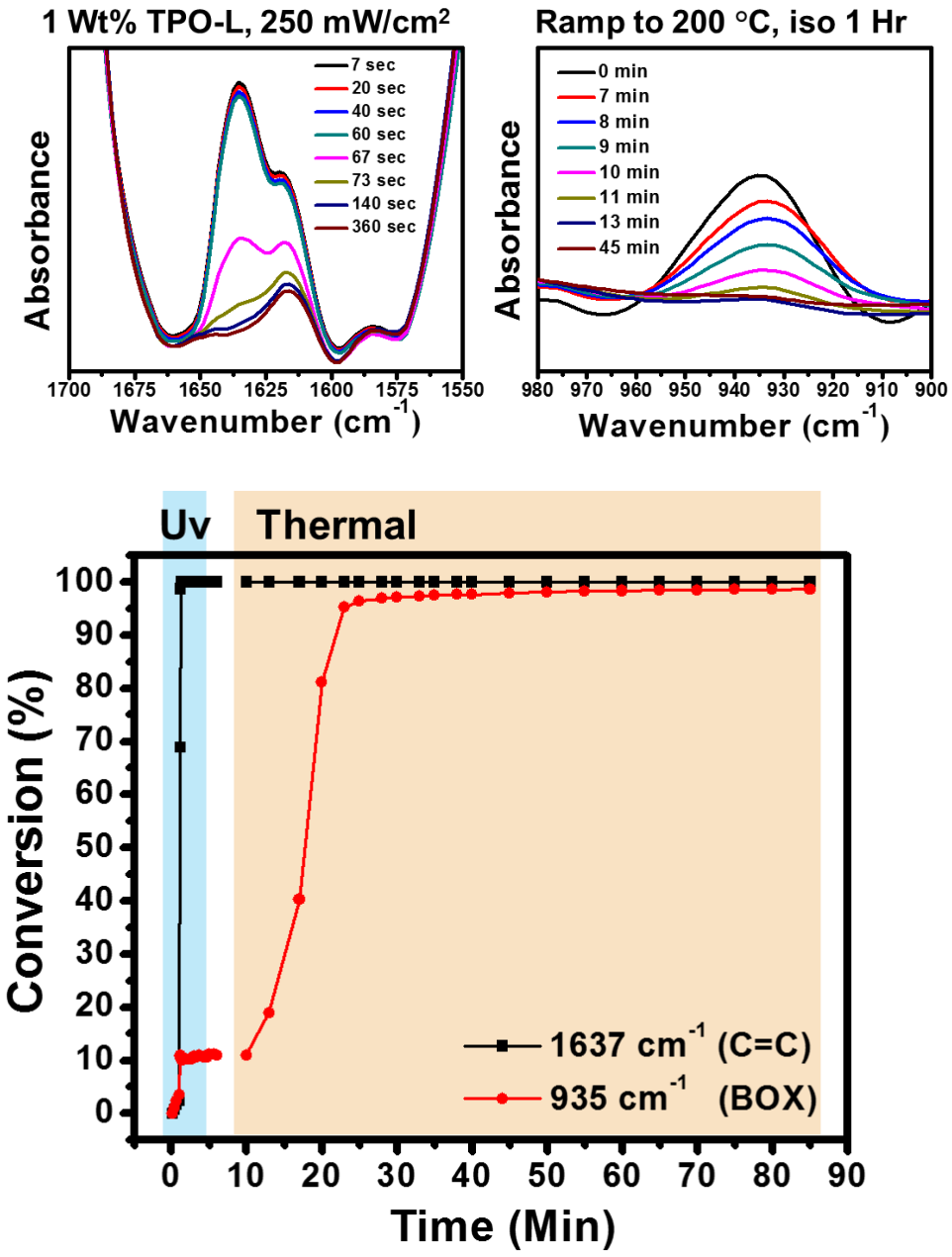

Figure 3.12 Real-time conversion plots of acrylate photopolymerization (1 wt% TPO-L photoinitiator, 250 mW cm^{-2}) and benzoxazine ring opening polymerization (200 °C)

3.2.5 Thermomechanical Properties After Primary and Secondary Cure

Dynamic mechanical analysis (DMA) was performed to study thermomechanical behavior of UV and thermally polymerized sample of 60:40 DMBOX:RD blends. Figure 3.13 shows Tan Delta plotted as a function of temperature where the maximum of the Tan Delta curve is used to determine the network T_g.

Samples tested after SLA 3D printing show a single Tan Delta peak at 32 °C attributed to the acrylate network photopolymerized during SLA 3D printing. After a 1 hr isotherm at 200 °C to thermally polymerize BOX moieties the unimodal Tan Delta peak of the sample increases in temperature from of 32 °C to 106 °C. This clear increase in T_g of 74 °C after thermal polymerization further supports the dual-cure nature of the printing formulation observed in DSC and FTIR experiments.

The unimodal Tan Delta peak after thermally initiated polymerization suggests both BOX and acrylate network are behaving as a single crosslinked network, which indicates an HPN was established from a dual-cure process composed of SLA AM and thermal cure. The heterogeneity of networks before and after secondary cure may be quantified by using the full width at half maximum (FWHM) of their respective Tan Delta curves. A broad Tan Delta peak suggests a heterogeneous network consisting of both highly crosslinked and loosely crosslinked regions, resulting in a broad distribution of relaxation times.[98,99] Photopolymerized acrylate and (meth)acrylate networks are known to be heterogeneous, exhibiting broad FWHM values.[99] Photopolymerized 60:40 DMBOX:RD blends exhibit a relatively narrow FWHM of 28.9 °C that increases significantly to 71.5 °C after heating for 1 hr at 200 °C. This increase in FWHM value

may be attributed to the increased network heterogeneity after thermally initiated polymerization of BOX.

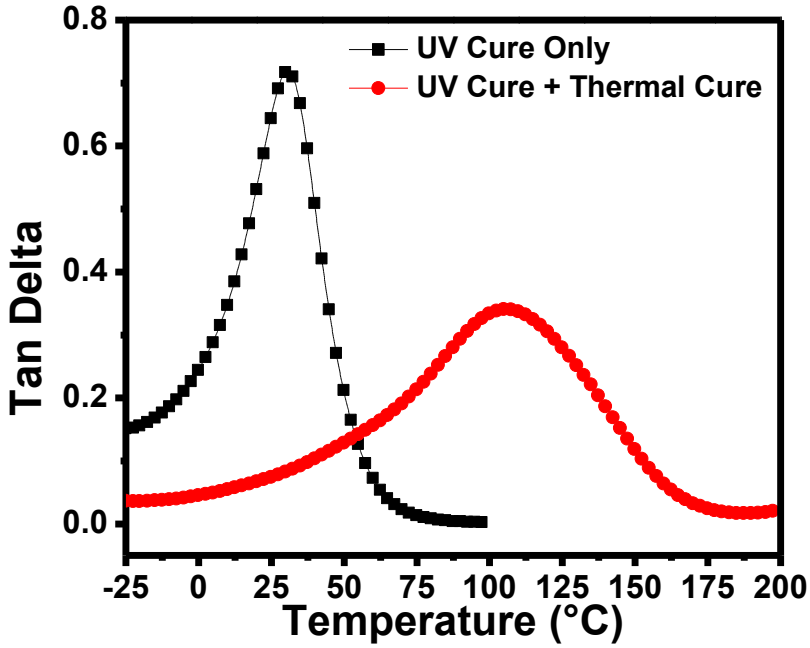

Figure 3.13 Tan Delta plotted as a function of temperature 60:40 DMBOX:RD 3D printed parts before and after thermally initiated BOX ring opening polymerization

Figure 3.14 shows the storage modulus plotted as a function of temperature for 60:40 DMBOX:RD 3D printed parts before and after thermally initiated BOX ring opening polymerization. The storage modulus of the 60:40 DMBOX:RD blend as printed is initially 3.3 GPa at -25 °C before sharply decreasing and ultimately reaching a rubbery modulus of 10.0 MPa at 72 °C. After thermally initiated polymerization of BOX moieties, the storage modulus is increased to 4.7 GPa at -25 °C before gradually decreasing to a rubbery modulus of 43.3 MPa at 146 °C. This increase in rubbery modulus after thermal polymerization is expected as a result of increased crosslink

density which was calculated using equation (4).[99] The crosslink density of UV cured 60:40 DMBOX:RD blends after SLA AM is initially 1.16 x 10^{-3} mol/cm^3 and increases to 4.11 x 10^{-3} mol/cm^3 after thermally initiated BOX polymerization.

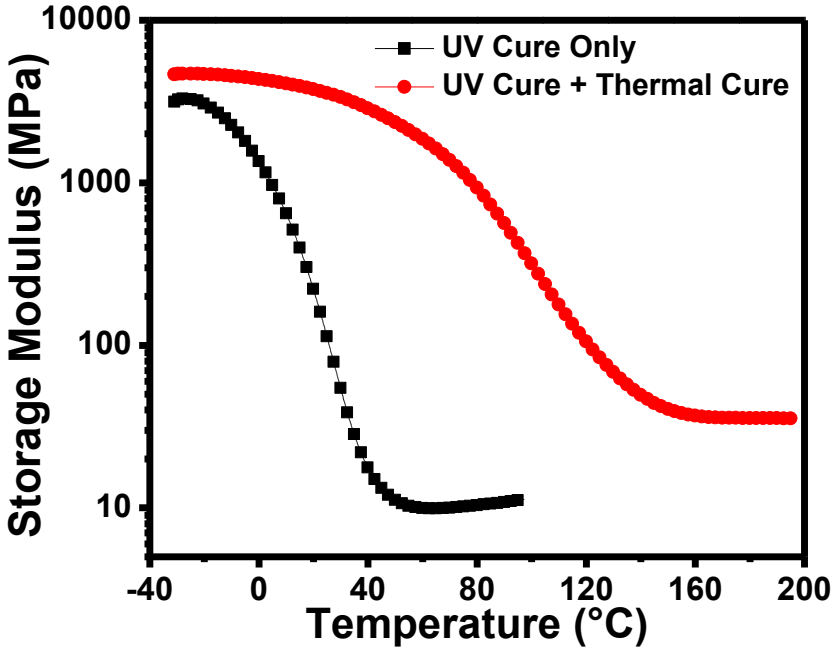

Figure 3.14 Storage modulus plotted as a function of temperature 60:40 DMBOX:RD 3D printed parts before and after thermally initiated BOX ring opening polymerization

Table 3.3 Summary of 60:40 DMBOX:RD thermomechanical data before and after thermally initiated BOX ring opening polymerization

Sample	**Tg °C**	**FWHH (°C)**	**E'$_{Glassy}$ (GPa)**	**E'$_{Rubbery}$ (MPa)**	**Crosslink Density (mol/cm^3)**
UV Cured	32	28.9	3.3	10	1.16 x 10^{-3}
UV Cure + 200 °C 1 hr	106	71.5	4.7	43	4.11 x 10^{-3}

Figure 3.15 shows the results of uniaxial compression testing of 3D printed 60:40 DMBOX:RD blends before and after thermally initiated BOX polymerization. The average Young's modulus of 3D printed BOX samples with no post cure is 35.6 MPa and samples exhibit ductile failure at an average yield strain of 0.375 mm/mm. After thermally initiated BOX polymerization, the average Young's modulus increases to 2.9 GPa and samples exhibit brittle failure at an average yield strain of 0.06 mm/mm. This trend of increasing Young's modulus and decreasing yield strain after thermally initiated BOX polymerization is expected considering the increased crosslink density determined during DMA experiments.

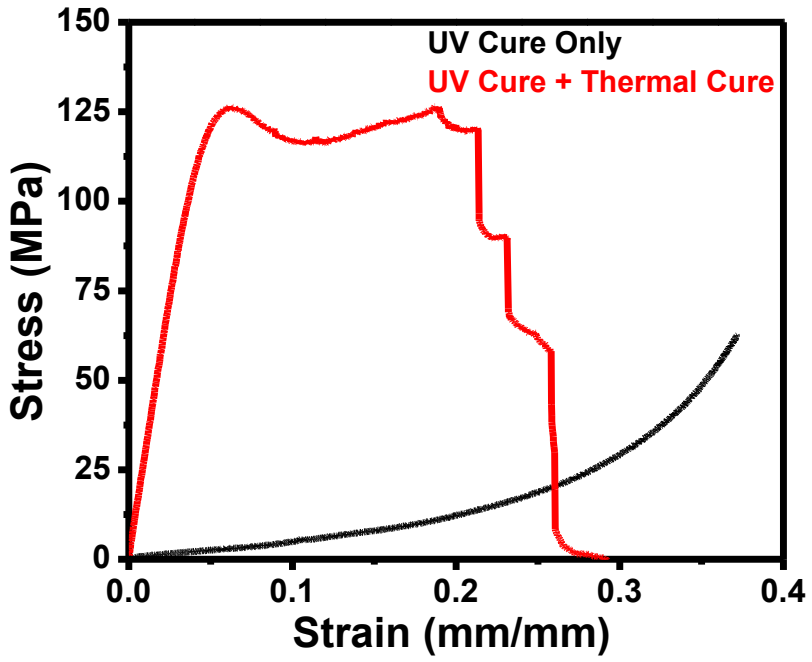

Figure 3.15 Uniaxial compression stress vs strain for 60:40 DMBOX:RD 3D printed parts before and after thermally initiated BOX ring opening polymerization

3.2.6 Conclusion

We have synthesized a multifunctional BOX monomer with both UV and thermal curing mechanisms to prepare blends suitable for SLA 3D printing. The viscosity of BOX-based printing blends is readily controlled using a reactive diluent to enable SLA 3D printing. 60:40 DMBOX:RD blends exhibit rapid UV cure kinetics at low photoinitiator loading levels exhibiting rapid gelation and high alkene conversion. After SLA AM, parts are subsequently heated to activate the thermally initiated BOX ring opening polymerization, demonstrating the application of a dual-cure nature of the printing formulation. UV and thermal initiated polymerizations were distinguished through monitoring polymerization exotherms by DSC, which were supported by the results of ATR-FTIR and RT-FTIR analysis, showing significant change of alkene and characteristic BOX absorption peaks by the UV-cure and thermal cure, respectively. The dual-cure nature of this novel printing blend was further confirmed by studying crosslinked network properties of 3D printed parts before and after thermal treatment to activate BOX ring opening polymerization. Dual-cured 3D printed parts exhibited both an increased T_g and an increased storage modulus compared to those of only UV-cured 3D printed parts, suggesting a significant increase in crosslink density with secondary thermal cure after 3D printing with primary UV cure.

The dual-cure strategy employed here may also be applied to a wide range of thermosetting chemistries to expand the range of 3D printing applications. The modular nature of BOX monomer synthesis may also be exploited to design additional dual-cure BOX monomers tailored for specific 3D printing applications. This study should be

expanded to further investigate how this dual-cure strategy may impact part mechanical properties and how properties vary with print orientation.

CHAPTER IV – Dual Cure Benzoxazine Blends

4.1 Abstract

We report the use of methacrylate functional benzoxazine (BOX) monomers for Stereolithography (SLA) 3D printing at room temperature. This was enabled by blending a di-(meth)acrylate functional BOX monomer with a novel (meth)acrylate functional BOX dual cure RD. Methacrylate groups were first photopolymerized during SLA 3D printing followed by thermal post processing to initiate BOX ring opening polymerization, resulting in a dual-cured thermoset network. Rheological experiments were conducted to determine the viscosity of di- and mono- functional BOX monomers before SLA 3D printing. UV cure kinetics were examined using photorheology and real time Fourier transform-infrared spectroscopy (RT-FTIR), where rapid UV curing kinetics at low photo initiator concentrations were observed. After photopolymerization via SLA

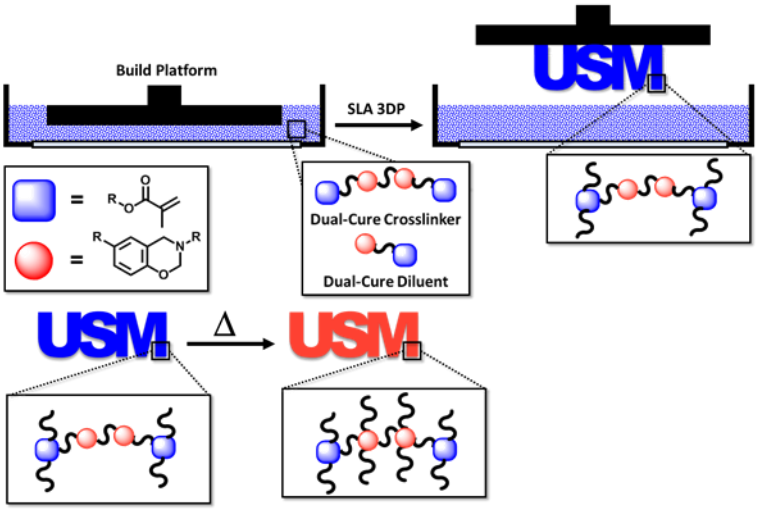

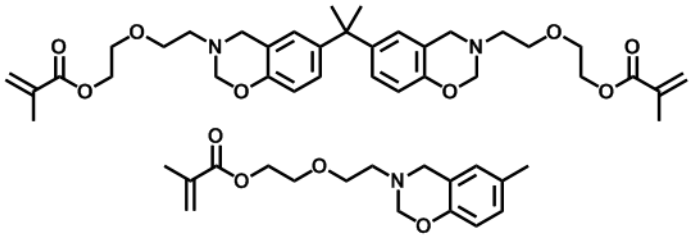

3D printing, high BOX monomer conversion was achieved at elevated temperatures as studied by FTIR and differential scanning calorimetry (DSC). Dynamic mechanical analysis (DMA) revealed that 3D printed parts exhibited a single T_g that increased 118 °C after heating, from an initial value of 50 °C which is attributed to increased network rigidity post BOX ring opening polymerization. The overarching goal of this work was to demonstrate a new class of dual-cure SLA 3D printing materials and enable the manufacture of complex thermoset geometries utilizing benzoxazine chemistries.

4.2 Results and Discussion

4.2.1 Printing Formulation Preparation and Rheological Characterization

Synthesis of di-(meth)acrylate functional BOX monomer (D-BOX) followed the synthetic procedures described in Sections 2.2 and Section 3.2. Scheme 2.2 shows the overall synthetic scheme for the synthesis of mono-(meth)acrylate functional BOX (M-BOX) monomer. Synthesis of the mono-hydroxy functional BOX precursor was performed in the bulk at a temperature of 90 °C for 90 min. M-BOX monomer was then synthesized by esterification of mono-hydroxy functional BOX monomer using methacryloyl chloride and triethyl amine as a base catalyst to obtain a green oil after purification. A detailed description of M-BOX monomer synthesis and monomer structure validation via ^{1}H-NMR and FTIR spectra are available in Section 2.2.

Viscous oil DMBOX was then blended with MBOX reactive diluent at room temperature using magnetic stirring to obtain a low viscosity homogeneous mixture. Viscosity of DMBOX, MBOX, and a 50 mol% blend of DMBOX and MBOX monomers are shown in Figure 4.1. The objective of this experiment was to establish viscosity data

of (meth)acrylate functional BOX monomers at shear rates characteristic of the SLA AM process. Viscosity data was collected using a rotational rheometer with a cone and plate geometry in air at ambient temperature (~28 °C) while the shear rate was varied from 0.5 s^{-1} to 5 s^{-1}. This shear rate range was determined to be representative of the SLA 3D printing process based on calculations done by Hsiao and coworkers.[79] The DMBOX and MBOX pure monomer viscosities were 187.9 Pa·s and 0.1 Pa·s, respectively while a 50 : 50 mol% blend of DMBOX and MBOX monomers resulted in a viscosity of 7.2 Pa·s. Monomer blends exhibit Newtonian behavior over the shear rates tested, this is expected due to the combination of relatively low molecular weight monomers and low shear rates tested.

Literature suggests viscosity of monomer or formulation should be ~5 Pa·s to be processable VPP AM techniques such as SLA.[81] Above this practical upper viscosity target, monomer will not flow sufficiently to recoat the build platform evenly, leading to uneven layers and dimensional inaccuracy in the final part. Due to this practical processing limit, a 50 mol% blend of DMBOX : MBOX monomers were utilized for the remainder of this study to ensure processability while maximizing network properties. Results of this experiment suggest that using our dual-cure approach, the viscosity of BOX monomer blends may be readily controlled for VPP AM at room temperature.

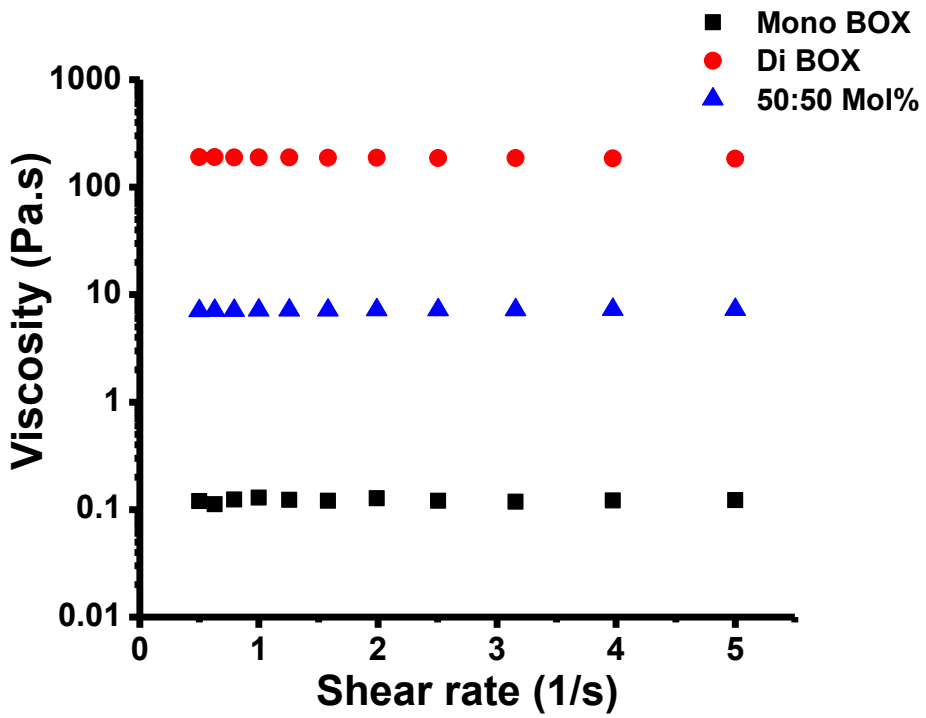

Figure 4.1 Plot of viscosity vs shear rate of DMBOX based blends

Figure 4.2 depicts the storage modulus (G') during UV irradiation for a 50 mol% blend of DMBOX and MBOX monomers with increasing TPO-L photoinitiator loading level. The objective of this experiment was to determine the minimum TPO-L loading level to achieve rapid photopolymerization kinetics. UV radiation is initiated 15 s after the start of the experiment where, as irradiation time increased, an increase in G' was observed for all samples, which indicates that the elastic property of samples was increased due to the photopolymerization of (meth)acrylate functional groups in the samples. The gelation point of a thermoset network is generally determined in rheological experiments as the time when the loss tangent becomes independent of frequency during crosslinking [82,83] Often, however, the time when G' and G'' crossover and G' becomes

greater than G'' is used as an estimation of the gel point.[84] This time point is representative of the transition from liquid like to solid like behavior of the sample during crosslinking, and is commonly used to determine photopolymerization rates.

Figure 4.3 plots time to the gel point, estimated using the G', G'' crossover point, during irradiation as a function of TPO-L photoinitiator loading level. Rapid photopolymerization kinetics and gel points in less than 10 s after irradiation are observed for all samples above 0.25 wt% TPO-L with a maximum in photo curing kinetics (fastest to gel) occurring at minimum 1 wt% TPO-L. Increasing TPO-L concentration above 1 wt% resulted in negligible differences in gel times. Thus, to avoid radical coupling or other chain termination events all future experiments and VPP AM were conducted using 1 wt% TPO-L. Curves showing G' G'' crossover are presented in Figure A.7.

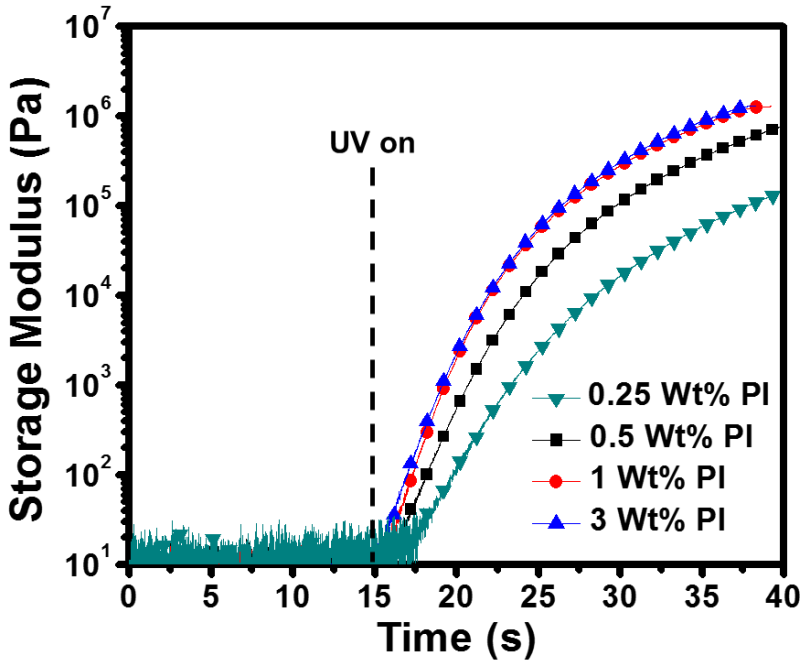

Figure 4.2 Storage modulus of 3D printing formulations with increasing TPO-L loading level as a function of time

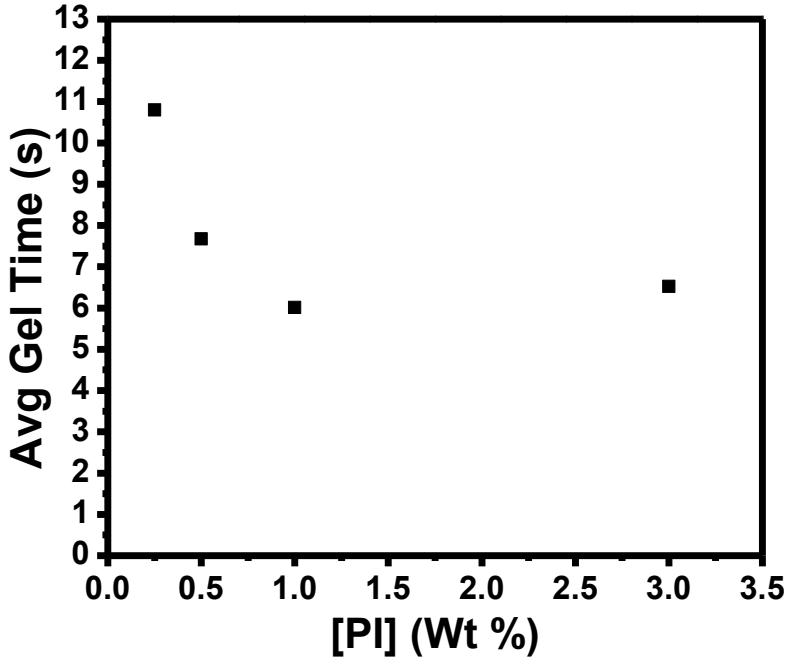

Figure 4.3 Gel time as a function of TPO-L concentration.

Gel points of BOX blends during photopolymerization were also investigated through the Winter-Chambon criteria.[85] Following this criterion, at the gel point G' and G'' follow the same power law dependency with respect to frequency and Tan Delta becomes independent of frequency, as discussed previously in Chapter IV. The crosslinking behavior of 50 mol% DMBOX : MBOX blends were investigated via the Winter-Chambon criteria using FTMS following similar methods discussed in Chapter IV.[65]

Results of FTMS experiments studying 50 mol% DMBOX : MBOX blend irradiated with 2 mW/cm^2 unfiltered UV light for 2 mins are depicted in Figure 4.4. BOX blends with 1 wt % TPO-L photoinitiator polymerized too rapidly to accurately capture

the Tan Delta crossover. In order to study BOX blends photopolymerization kinetics through the Winter-Chambon criteria samples were formulated with 0.25 wt% TPO-L, slowing photopolymerization kinetics and allowing for more time to accurately capture the Tan Delta crossover. Samples were irradiated after 15 s where after irradiation Tan Delta becomes independent of frequency at 20.1 s, indicating gelation. Additionally, using Equation (1) and the Tan Delta value at frequency independence, *n* was found to be equal to 0.96 for the photopolymerized 50 mol% DMBOX : MBOX monomer blend critical gel, which would indicate a soft critical gel.

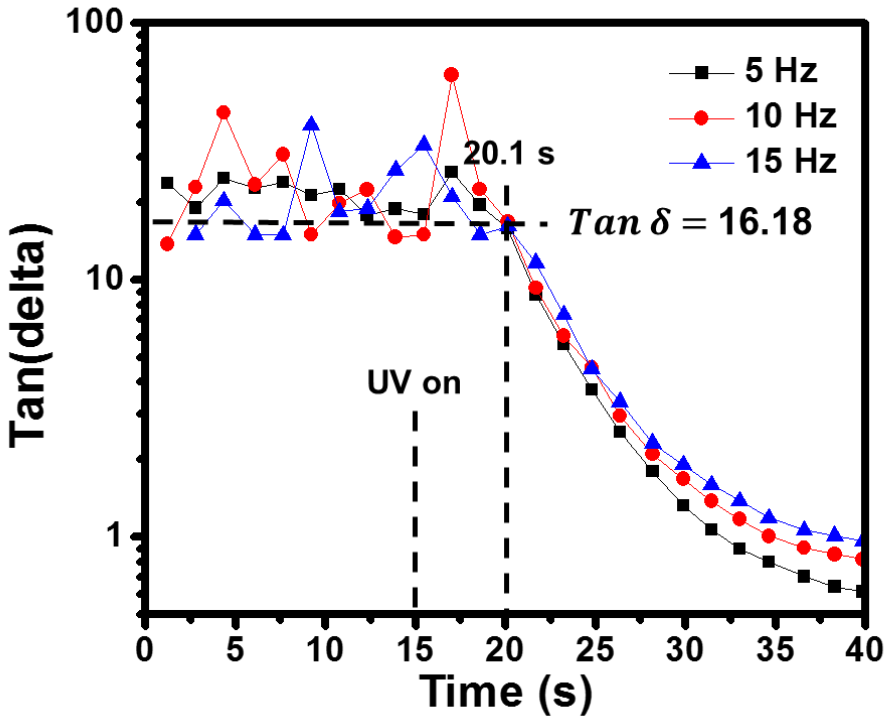

Figure 4.4 Tan Delta measured as a function of irradiation time for 50 mol% DMBOX : MBOX blend with 0.25 wt% TPO-L

Figure 4.5 shows results of photorheology experiments studying photopolymerization kinetics of DMBOX : MBOX blends as a function of DMBOX concentration with 1 wt% TPO-L photoinitiator. Before irradiation, samples exhibit liquid like behavior where the viscous modulus, G'' is greater than the elastic modulus, G'. Initially samples follow a trend of increasing G'' with increasing DMBOX concentration; this trend may be explained by an increase in monomer blend viscosity as DMBOX concentration is increased.

Upon irradiation, free radical polymerization is initiated and both G' and G'' increase as a function of reaction time and eventually cross over, indicating a transition from liquid-like to solid-like behavior. The blends follow a trend of increasing photopolymerization kinetics with increasing DMBOX concentration; this trend may be observed in Table 4.1 where the time to G' / G'' crossover decreases with increasing DMBOX concentration. This trend of increasing photopolymerization kinetics with increasing DMBOX concentration is expected due to a higher concentration of photopolymerizable (meth)acrylate functional groups available. After G' / G'' crossover, G' continues to increase before reaching a final plateau, as expected upon the formation of a crosslinked network. Final G' plateau values of photopolymerized networks increase with increasing DMBOX concentration due to an increase in crosslink density with increasing DMBOX monomer concentration.

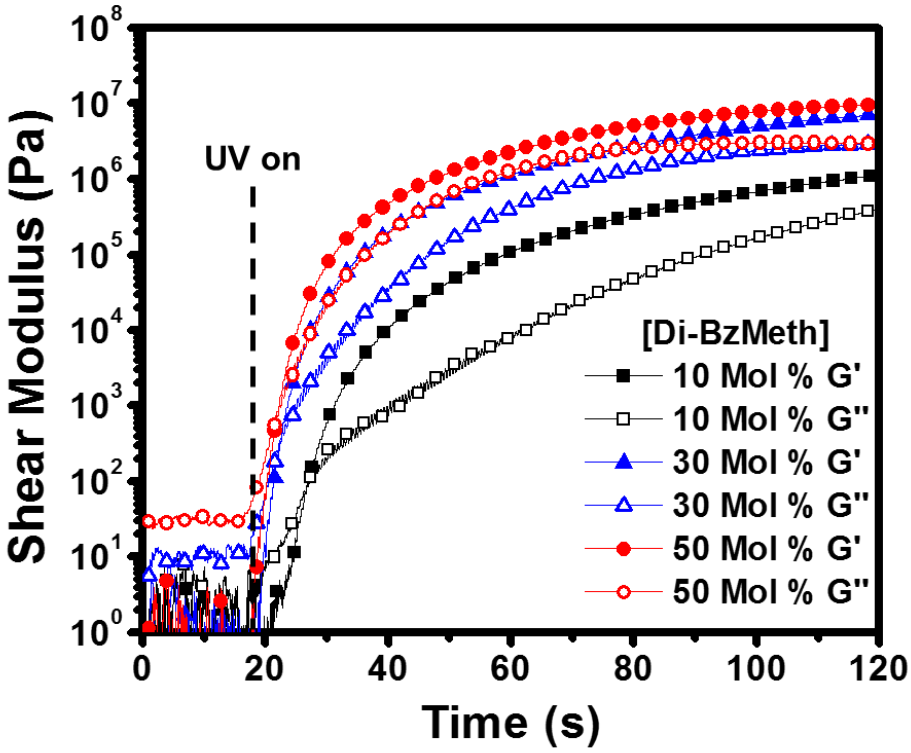

Figure 4.5 Shear storage and loss modulus of 3D printing formulations with 1 wt% TPO-L and increasing DMBOX concentration as a function of irradiation time

Table 4.1 Photorheology of 3D printing formulations with 1 wt% TPO-L and increasing DMBOX concentration

Sample (DMBOX Mol%)	Initial G'' (Pa)	Initial Complex Viscosity (Pa·s)	G' / G'' Crossover (s)	Final G' (10^6 Pa)
10	2.8	0.6	26.8	1.1
30	10.0	1.6	22.3	7.3
50	30.5	4.9	21.8	9.8

Real-time FTIR (RT-FTIR) was also used to monitor the kinetics of UV initiated free radical polymerization of the 50 mol% DMBOX : MBOX monomer blend with 1 wt% TPO-L. This photoinitiator loading level was selected based on photorheology results where it was found that this loading level maximized photo polymerization rates as discussed in section 3.1. During RT-FTIR measurements, samples were sandwiched between two NaCl plates and irradiated with un-filtered UV light at 250 mW cm^{-2}. Typically, a low concentration of UV absorber is added to a printing formulation to improve print resolution. To ensure rapid photopolymerization kinetics are maintained with the addition of the UV absorber, 0.07 wt% of commercially available Tinuvin Carboprotect UV absorber was added to samples studied during RT-FTIR experiments.

Figure 4.6 shows the results of RT-FTIR experiments where polymerization conversion is plotted as a function of irradiation time. During RT-FTIR experiments, the conversion of (meth)acrylate C=C double bonds is calculated using the C=C stretching at 1637 cm^{-1} and the conversion of BOX groups is calculated using the out of plane C-H vibration of the benzene ring attached to the oxazine ring at 935 cm^{-1}. RT-FTIR results show no conversion of (meth)acrylate C=C double bond polymerization until samples are irradiated, upon which a final conversion of 87% is reached after 5 minutes. BOX functional groups also begin to be consumed upon UV irradiation, reaching a final conversion of 34% after 5 minutes of irradiation. Similar results for (meth)acrylate functional BOX monomers have also been observed by Ishida et al.[29] These results may be due to UV irradiation initiating BOX ring opening polymerization or heat due to the exothermic (meth)acrylate free radical photopolymerization.

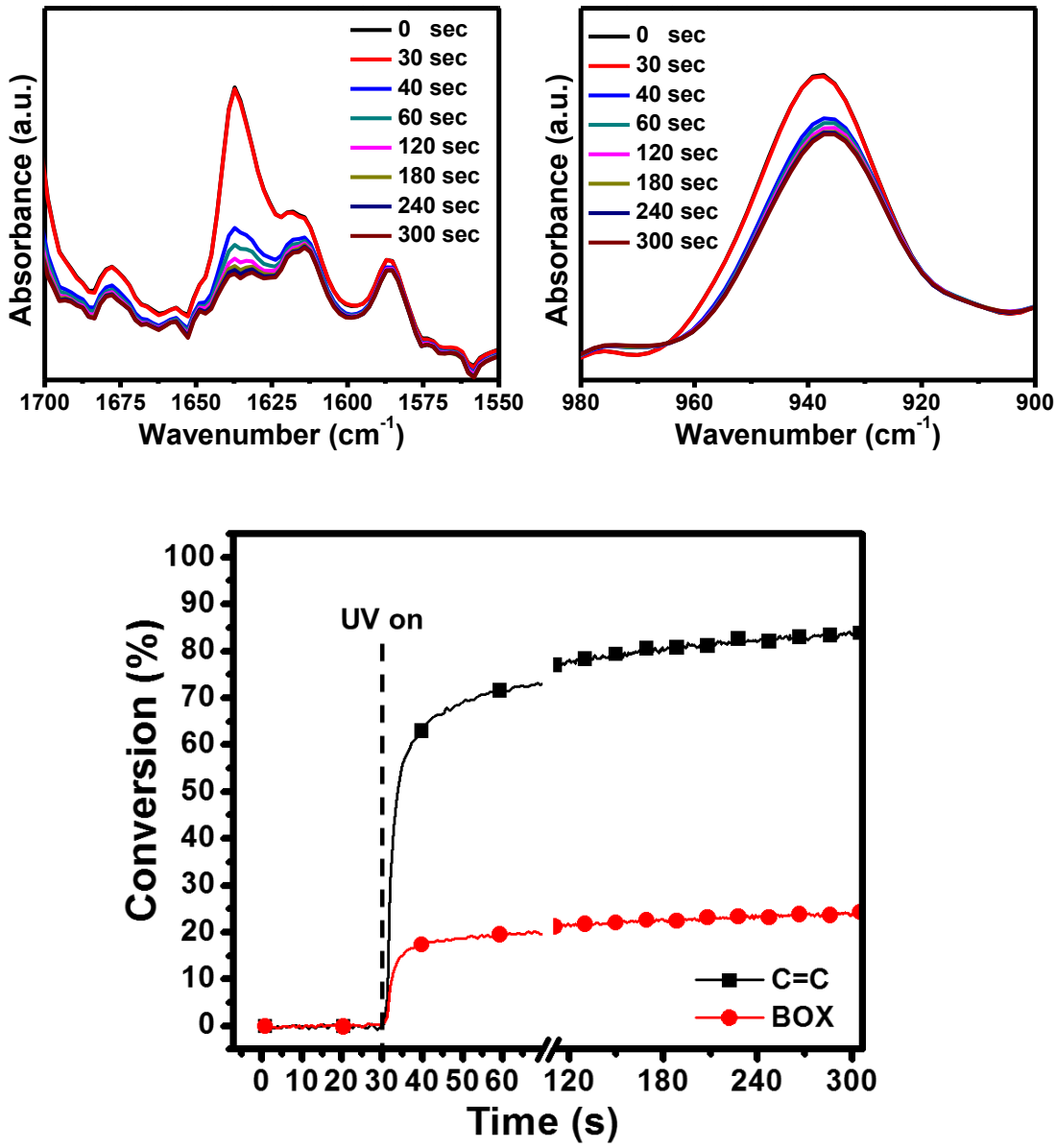

Figure 4.6 Conversion of (meth)acrylate C=C double bond and BOX as a function of irradiation time.

4.2.2 Thermal Stability and Ring Opening Polymerization of BOX

TGA was used to determine the mass loss as a function of temperature for 50 mol% DMBOX : MBOX un-cured monomer blend, 3D printed parts, and 3D printed parts with a secondary thermal cure. TGA weight loss profiles are shown in Figure 4.7 and the data are summarized in Table 4.2. The initial degradation temperatures ($T_{5\%}$ and $T_{10\%}$) for the uncured monomer blend are 206 °C and 225 °C respectively and increase significantly after 3D printing to 266 °C and 287 °C respectively. The $T_{5\%}$ and $T_{10\%}$ degradation temperatures of parts photopolymerized after VPP AM are similar to reports in the literature studying the thermal degradation of structurally similar poly(methyl methacrylate) networks.[93] The $T_{5\%}$ and $T_{10\%}$ degradation temperatures of 3D printed parts with a secondary thermal cure to initiate BOX polymerization further increase to 289 °C and 312 °C, respectively. The thermal degradation profiles observed in this study for 3D printed samples tested after thermal cure show good agreement with the degradation of polybenzoxazine networks derived from aliphatic amines.[38] All samples studied exhibit a two stage thermal degradation mechanism, where after initial degradation events, weight loss profiles for all samples also show a second thermal degradation step at 400 °C. The second stage of thermal decomposition begins near 400 °C is attributed to the thermal degradation of substituted phenolic units and main-chain polymer chains.[38]

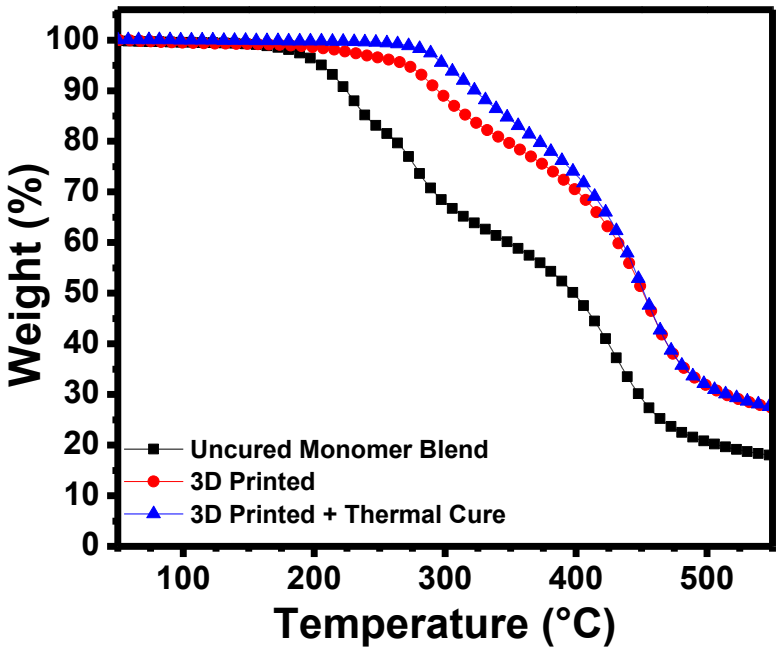

Figure 4.7 TGA weight loss profiles of 50 mol% DMBOX : MBOX un-cured monomer blend, 3D printed networks, and 3D printed networks after thermal cure

Table 4.2 Summary of Thermal Degradation Temperatures of BOX Blends

Sample	**$T_{5\%}$ (°C)**	**$T_{10\%}$ (°C)**
Un-Cured Monomer Blend	206	225
3D Printed	266	287
3D Printed + Thermal Cure	289	312

Figure 4.8 depicts isothermal TGA studies conducted to investigate the maximum curing temperature of 3D printed 50 mol% DMBOX : MBOX monomer blend. Samples were first held isothermally at 100 °C for 30 mins before heating at 1 °C/min to 120, 140, 160, 180, 200, and 220 °C. Samples were held isothermally at each temperature for 1 hr to monitor weight loss as a function of time. Weight loss values after each 1 hr isotherm are 0.41, 0.58, 0.50, 0.57, 1.31, and 3.00 wt % respectively for each temperature. A

maximum curing temperature of 180 °C was selected due to the increase in thermal degradation from 0.57 wt % at a 180 °C 1 hr isotherm to 1.31 wt % at a 200 °C 1 hr isotherm.

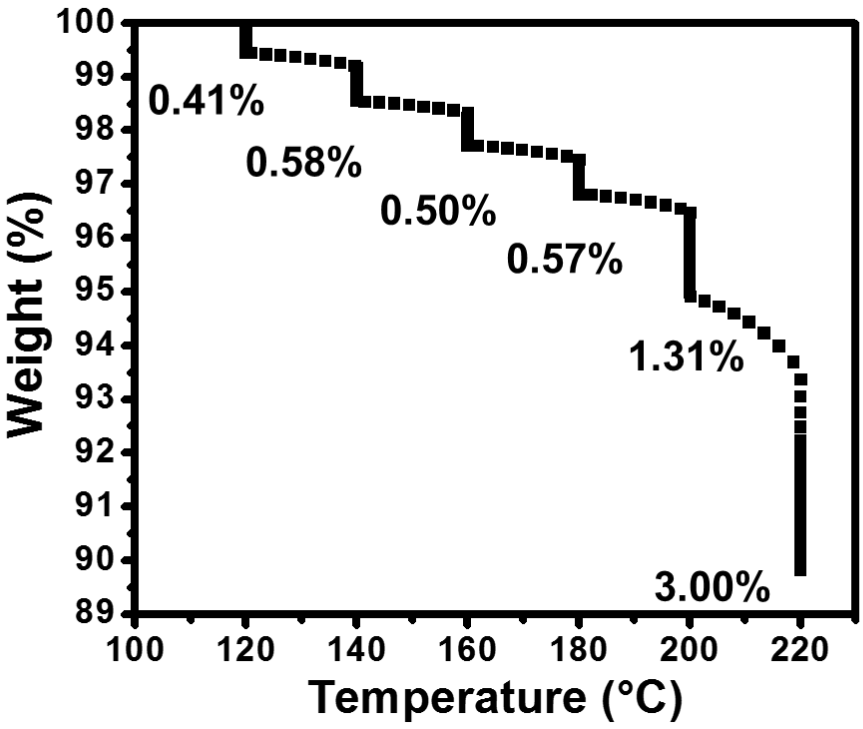

Figure 4.8 3D printed 50 mol% DMBOX : MBOX blend held isothermally for 1 hr at increasing temperatures. Labels indicate weight loss % at each temperature

Figure 4.9 presents isothermal TGA experiments at 180 °C performed to monitor weight loss as a function of time at the sample maximum cure temperature. Samples exhibit a weight loss of 1.44 wt% during a 20 °C/min ramp from 20 °C to 180 °C before reaching a stable degradation rate of 0.003 wt%/min. These studies may be compared to the thermal degradation behavior or volatilization of BOX monomers during cure as reported in the literature, where during isothermal heating at 180 °C for 3 hrs a weight

loss of 1.6 – 8.5 wt % has been observed for bisphenol A based BOX monoemrs.[94–96] This is in contrast to 3D printed 50 mol% DMBOX : MBOX monomer blend studied during isothermal TGA experiments which exhibited a final weight loss of 3.4 wt % after 8 hrs at 180 °C. The photopolymerized (meth)acrylate network during 3D printing may contribute to the thermal stability of 3D printed 50 mol% DMBOX : MBOX monomer blend.

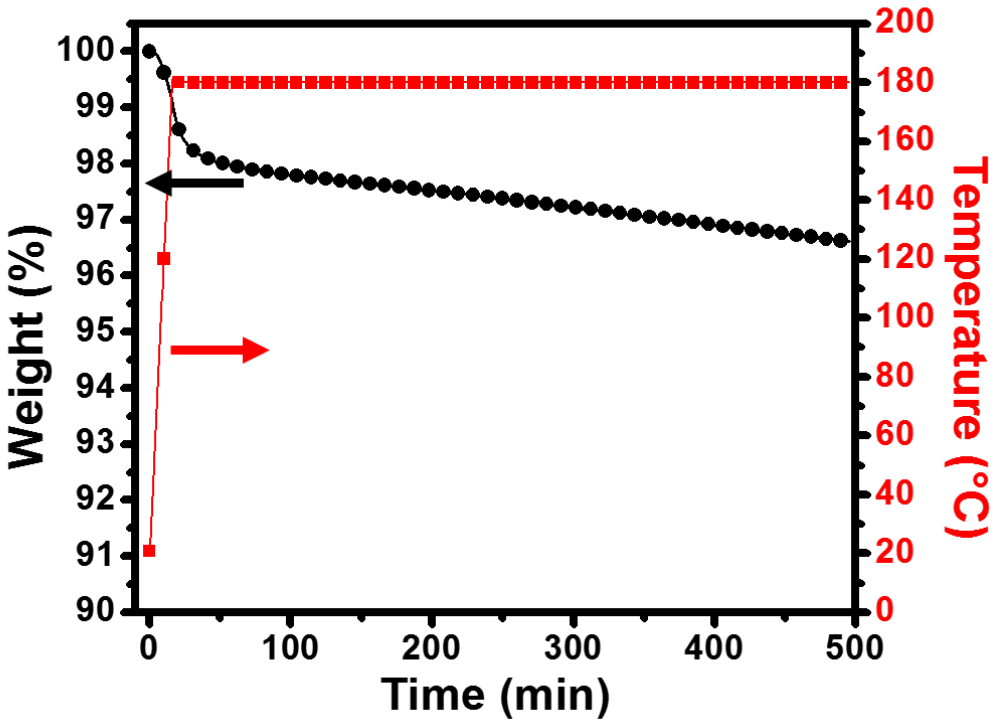

Figure 4.9 3D printed 50 mol% DMBOX : MBOX blend held isothermally at 180 °C for 8 hrs

The thermal polymerization behavior of 50 mol% DMBOX : MBOX monomer blend was studied using DSC. Thermograms of the uncured monomer, after 3D printing,

and after thermal cure of the 3D printed part are depicted in Figure 4.10. Thermograms of the un-cured monomer blend showed two exothermic peaks with peak maxima at 142 °C and 256 °C which exhibited heats of polymerization of 120 J/g and 274 J/g, respectively . The exotherm at 142 °C was attributed to the thermal polymerization of (meth)acrylates while the exotherm at 256 °C was attributed to the thermally initiated cationic ring opening polymerization of BOX.[29,31]

Samples that have been free radically polymerized by UV radiation during 3D printing showed one broad exothermic peak with two peak maxima, the first at 175 °C and the second at 261 °C. The exotherm at 175 °C after 3D printing is attributed to polymerization of residual (meth)acrylate functional groups with hindered molecular mobility due to UV-cured (meth)acrylate network. The increased onset and peak temperatures of BOX cationic ring opening polymerization exotherm observed in samples after 3D printing may be also be attributed to restricted mobility due to the UV-cured (meth)acrylate network.[29]

Photopolymerized samples were then heated step-wise at 100 °C for 30 minutes, 120 °C for 1 hr, 140 °C for 1 hr, 160 °C for 1 hr, and 180 °C for 2 hrs. The thermal polymerization procedure investigated in this study was selected following isothermal TGA studies discussed previously where it was found that above 180 °C samples begin to undergo significant thermal degradation (see Figure 4.7). After the thermal polymerization procedure, only one exothermic peak is present at 254 °C, where the absence of the exothermic peak at 175 °C suggests residual (meth)acrylate groups have been polymerized during the thermal polymerization procedure. The exothermic peak at 254 °C attributed to BOX polymerization shows a significant reduction in heat of

polymerization from 240 J/g to 110 J/g. The remaining exotherm is attributed to polymerization of residual BOX moieties after thermal cure and may also be complicated by degradation processes near the $T_{5\%}$ at 289 °C observed in TGA experiments (see Figure 4.6).

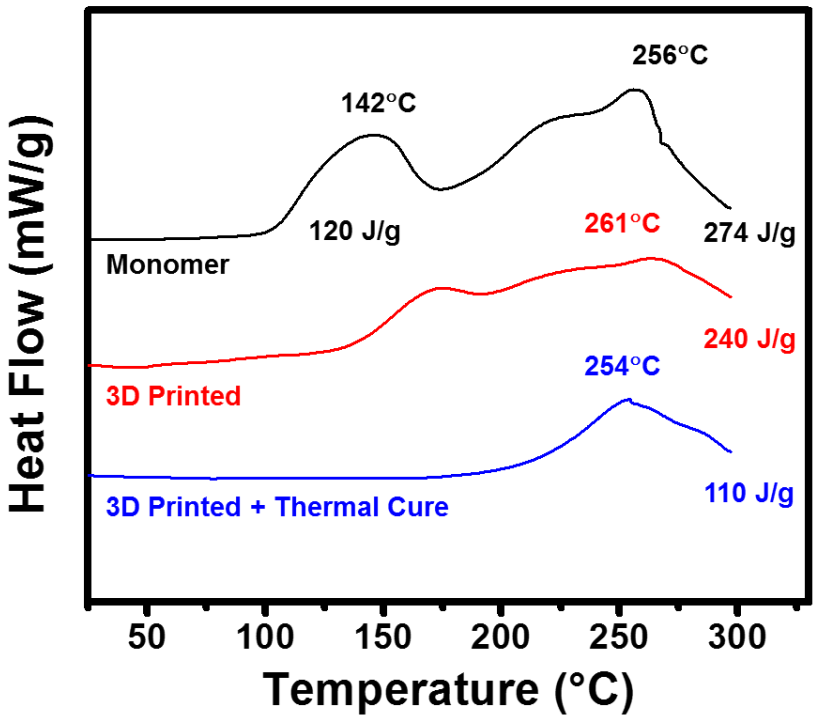

Figure 4.10 DSC thermograms for 50 mol% DMBOX : MBOX monomer blend, after 3D printing, and after thermal cure

RT-FTIR was used to monitor the polymerization rate of thermally initiated ring opening BOX polymerization of 50 mol% DMBOX : MBOX monomer blend. Conversion of BOX ring opening polymerization is calculated using the out of plane C-H bending vibration of the benzene ring attached to the oxazine ring at 935 cm^{-1}. This IR

absorbance has been shown to be directly related to the BOX characteristic oxazine ring and may be used to monitor BOX polymerizations.[100] Figure 4.11 shows the results of RT-FTIR experiments where BOX polymerization conversion is plotted as a function of heating time. Samples photopolymerized between NaCl plates during RT-FTIR experiments in Section 4.2.1 were placed in a heated cell to monitor BOX ring opening polymerization rate. The step wise heating protocol was selected based on DSC and TGA experiments discussed previously.

Photopolymerized samples were heated step wise to 100 °C for 30 minutes, 120 °C for 1 hr, 140 °C for 1 hr, 160 °C for 1 hr, and 180 °C for 2 hrs. During the first heating stage at 100 °C BOX polymerization initiates, and gradually continues, reaching >5% conversion after 30 mins. As temperature is increased to 120 °C, BOX conversion increases rapidly before gradually plateauing after ~15 mins. BOX conversion again increases with increasing isothermal temperature, reaching 20% conversion after 1 hr at 120 °C, 47% after 1 hr at 140 °C, 74% after 1 hr at 160 °C, and finally reaching near full conversion of >95% after 2 hrs at 180 °C.

High BOX polymerization conversions observed during our studies after heating at 180 °C for 2 hrs are consistent with similar BOX polymerizations in the literature.[100] The behavior of increasing BOX polymerization rate with an increase in isothermal temperature before gradually plateauing seems to be consistent with all isothermal temperatures studied. This behavior may be due to an increase in molecular mobility, which would allow for increased polymerization rate, before a subsequent decrease in mobility due to an increase in crosslink density as BOX polymerization continues.

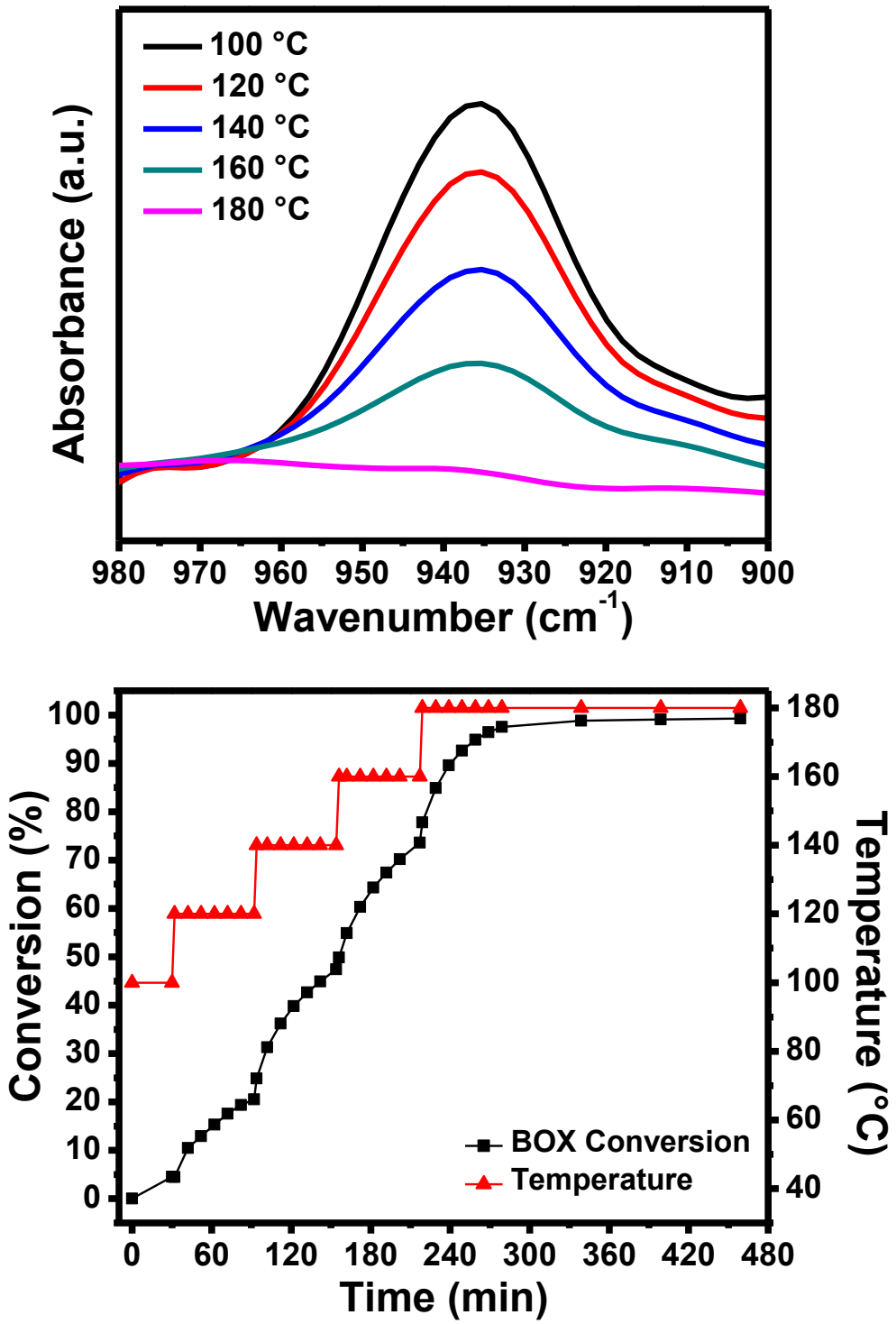

Figure 4.11 Conversion of BOX ring opening polymerization at increasing isothermal temperatures

The thermal intiated ring opening polymerization of BOX moieties was further studied through rheological experiments. Photopolymerized 50 mol% DMBOX : MBOX films studied during photorheology experiments were quenched in liquid nitrogen and collected for thermal curing. Photopolymerized sample was placed between 8 mm stainless steel plates and trimmed to size at a gap of 0.5 mm. A normal force of 5 N was then applied before heating samples from ambient temperature to 180 °C at a ramp rate of 10 °C/min.

Figure 4.12 plots the storage modulus and temperature during the thermal cure of dual-cure BOX films. As the temperature is increased, a decrease in the storage modulus is initially observed as the photopolymerized film enters the rubbery state. During isothermal heating at 180 °C the storage modulus begins to increase with increasing BOX polymerization time, eventually reaching a plateau at 10^7 Pa. This increase in storage modulus is expected as increasing crosslinking due to BOX polymerization would increase the magnitude of the rubbery storage modulus.

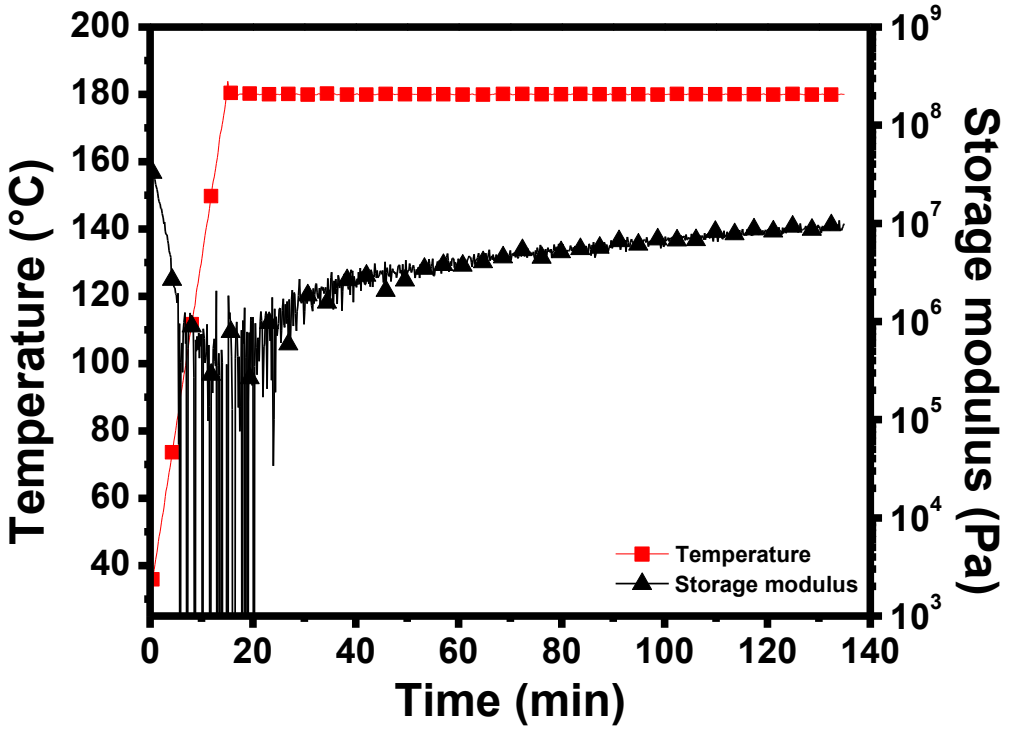

Figure 4.12 Rheological characterization of thermally intiated BOX polymerizatio

4.2.3 Thermomechanical Properties

Dynamic mechanical analysis (DMA) was performed to study thermomechanical behavior of 3D printed and thermally polymerized samples of DMBOX and MBOX 50 mol% blends. Figure 4.13 shows Tan Delta plotted as a function of temperature where the maximum of the Tan Delta curve is used to determine the network T_g. Samples tested after SLA 3DP show a Tan Delta peak at 50 °C attributed to the acrylate network photopolymerized during SLA 3D printing. After thermally polymerizing BOX moieties, the Tan Delta peak increases by 118 °C to 168 °C, which is ~10 °C higher than the T_g of commercially available bisphenol-a based BOX produced by Huntsman Corporation.[101,102]

The unimodal nature of the Tan Delta peak after thermal polymerization also suggests both BOX and (meth)acrylate networks do not phase separate, but are homogeneous and behave as a single crosslinked network. The homogeneity or heterogeneity of networks before and after secondary cure may be quantified by using the full width at half maximum (FWHM) of their respective Tan Delta curves. A broad Tan Delta peak suggests a heterogeneous network consisting of both highly crosslinked and loosely crosslinked regions, resulting in a broad distribution of relaxation times.[98,99] Photopolymerized (meth)acrylate networks are known to be heterogenous, exhibiting broad FWHM values.[99] Photopolymerized 50 mol% DMBOX : MBOX blends exhibit a FWHM of 43.1 °C that slightly decreases to 37.4 °C after thermal polymerization of BOX. This improvement of network homogeneity may be attributed to the hybrid nature of the (meth)acrylate and BOX network that are covalently crosslinked together. Similar network uniformities have been observed in other epoxy-(meth)acrylate hybrid network structures in the literature.[103]

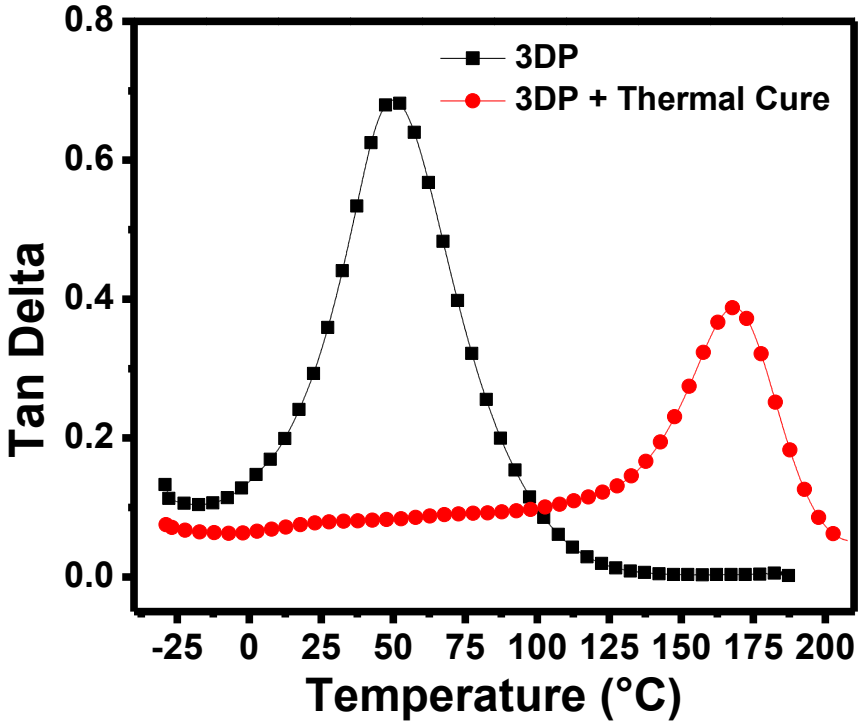

Figure 4.13 Tan Delta plotted as a function of 50 mol% DMBOX : MBOX 3D printed parts before and after thermally initiated BOX ring opening polymerization

Figure 4.14 plots the storage modulus as a function of temperature for 50 mol% DMBOX : MBOX 3D printed samples before and after thermally initiated BOX ring opening polymerization. The storage modulus of the 50 mol% DMBOX : MBOX blend as printed is initially 3.8 GPa at -25 °C before sharply decreasing and ultimately reaching a rubbery modulus of 20.3 MPa at 90 °C. After reaching a rubbery plateau, continued heating of the 3D printed BOX sample results in a gradual increase in E', suggesting additional crosslinking. 3D printed samples tested after thermal polymerization of BOX moieties show a slightly increased glassy storage modulus of 3.9 GPa at -25 °C before gradually decreasing to a rubbery modulus of 63.6 MPa at 207 °C. This increase in

rubbery modulus after thermal polymerization is expected, as a result of increased crosslink density from 2.24 x 10^{-3} mol/cm^3 after VPP AM to 5.30 x 10^{-3} mol/cm^3 after thermally initiated BOX polymerization.[68]

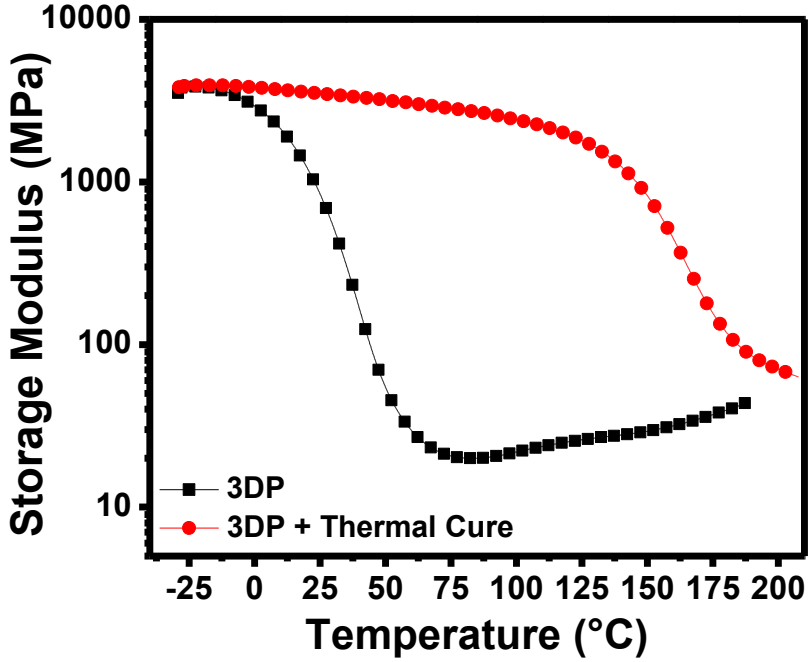

Figure 4.14 Storage modulus plotted as a function of temperature 50 mol% DMBOX : MBOX 3D printed parts before and after thermally initiated BOX ring opening polymerization

Table 4.3 Summary of 50 mol% DMBOX : MBOX thermomechanical data before and after thermally initiated BOX ring opening polymerization

Sample	**T_g °C**	**FWHH (°C)**	**E'$_{Glassy}$ (GPa)**	**E'$_{Rubbery}$ (MPa)**	**Crosslink Density (mol/cm^3)**
UV Cure	50	43.1	3.8	20.3	2.24 x 10^{-3}
UV Cure + Thermal Cure	168	37.4	3.9	63.6	5.30 x 10^{-3}

4.2.4 SLA 3D Printing Performance

A 50 mol% DMBOX : MBOX monomer blend with 1 wt% TPO-L and 0.07 wt% UV absorber was selected for SLA 3D printing. An example of a structure printed using the SLA style Form 2 3D printer is shown in Figure 4.15. Printed structures exhibited reasonable dimensional accuracy on the micrometer size scale and these features were maintained after thermal cure. Surface topology of printed objects were investigated using optical light microscopy where micron scale surface defects were observed. These surface defects may be due to incomplete photopolymerization during SLA 3DP, residual solvent from monomer synthesis, or imparted during solvent rinse post SLA 3DP. Further optimization of 3DP parameters such as UV expose time or intensity will be further investigated to improve printed part surface features.

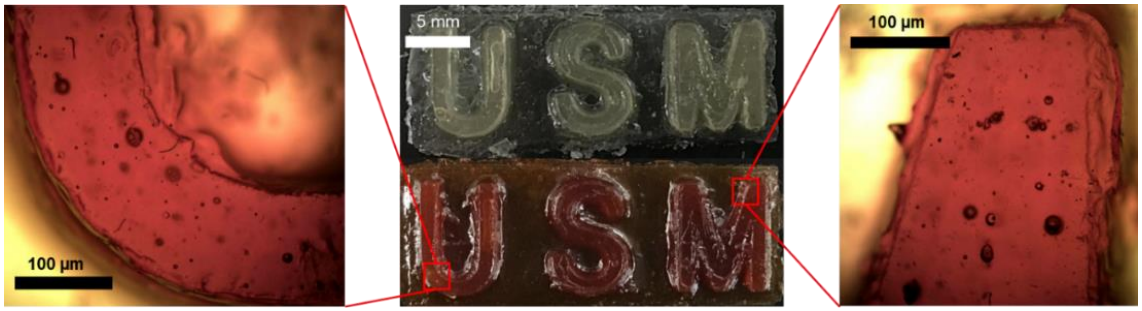

Figure 4.15 SLA 3D printed object example from the 50 mol% DMBOX : MBOX monomer blend with 1 wt% TPOL and 0.07 wt% UV absorber before and after thermal polymerization of BOX.

4.2.5 Conclusions

This research has demonstrated the synthesis of di- and mono- functional BOX monomers with both UV and thermal polymerization mechanisms to prepare blends suitable for SLA AM at room temperature. The viscosity of BOX monomer blends is readily controlled by modifying DMBOX : MBOX ratio to enable SLA AM.

BOX blends exhibit fast photopolymerization rates at low photoinitiator loading levels resulting in rapid gelation and high alkene conversion as monitored by photorheology and RT-FTIR respectively. TGA experiments studying the thermal stability of photopolymerized networks were used to guide thermal polymerization conditions that would result in minimal thermal degradation but maximize BOX polymerization conversion. BOX polymerization was studied in detail using DSC and RT-FTIR to track BOX polymerization conversion. After thermal polymerization of BOX, parts exhibited thermomechanical properties similar to, or exceeding that, of commercially available bisphenol-A based BOX networks. In addition, dimensional accuracy of printed features on the micrometer size scale were maintained after thermal polymerization.

The dual-cure strategy employed here has enabled the processing of BOX networks using SLA AM to expand the material base available for the popular AM method. Future studies should continue to take advantage of the modular nature of BOX monomer synthesis to prepare additional dual-cure monomers with increased T_g values while maintaining low viscosities and rapid polymerization rates at room temperature.

CHAPTER V – Molecular Dynamics Simulations of Acrylate Networks

5.1 Abstract

Additive manufacturing (AM) , also known as 3D printing, has emerged as a powerful manufacturing technique for the rapid production of highly complex parts. Stereolithography (SLA) is an AM approach which selectively exposes liquid resin to a rastering UV laser to build parts in a layer-by-layer approach. While SLA offers manufacturing advantages, the continued use of SLA in a variety of applications necessitates the development of new materials for this innovative process. Our methods utilize a combined experimental and computational approach, utilizing Molecular Dynamics (MD) simulations to study the photo initiated free radical polymerization of an acrylate during SLA 3D printing at an atomistic level. After simulated crosslinking, network properties including crosslink density and glass transition temperature are calculated. Simulation results are found to be in good agreement with results determined experimentally. The methods presented in this work provide new insights into the use of MD simulations for the study and design of new 3D printing materials.

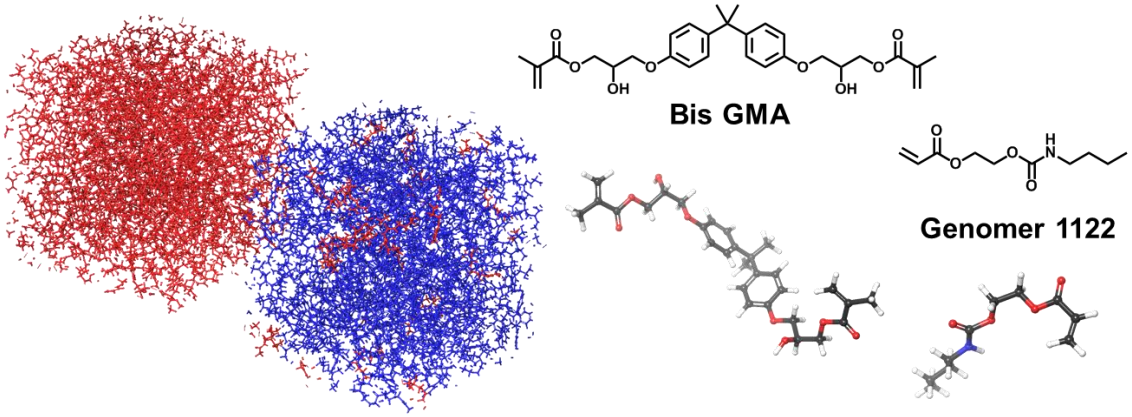

5.2 Results and Discussion

5.2.1 Viscosity and Cure Kinetics of Printing Formulations

SLA and other similar vat photopolymerization (VPP) based AM techniques rely on the ability of monomers or prepolymers to freely flow in the monomer or prepolymer bath to cover the previously printed layer. Considering this, a given printing formulation should have a viscosity in the range of 10 Pa.s to be considered processable via a VPP AM method.[104] Above this practical upper viscosity target, monomer will not flow sufficiently to recoat the build platform evenly, leading to uneven layers and dimensional inaccuracy in the final part. Hsiao and coworkers, using a similar vat photopolymerization AM technique, calculated that the operating shear rate is approximately 1.7 s^{-1}.[79] To quantify the viscosity of our printing formulations at similar shear rates to the calculated value of 1.7 s^{-1}, we conducted shear sweeps from 0.1 s^{-1} to 5 s^{-1} using cone and plate rheology.

In Figure 5.1 we present the results of these experiments for formulations of bisphenol A diglycidyl ether dimethacrylate (BisGMA), with increasing loading levels of 2-(((butylamino) carbonyl)oxy)ethyl ester (UA), a mono-functional urethane acrylate reactive diluent. BisGMA is a viscous, high molecular weight difunctional (meth)acrylate monomer with a rigid bisphenol a based backbone. The viscosity of blends were systematically reduced as bisGMA is diluted with increasing loading level of the relatively lower molecular weight UA monomer. For all formulations viscosity remains constant over the tested shear rates and no shear thinning or thickening behavior is observed. Additionally, we observe that formulations with a UA mol % of 50% and above exhibit a viscosity below 10 Pa.s and are considered to be processable via SLA.

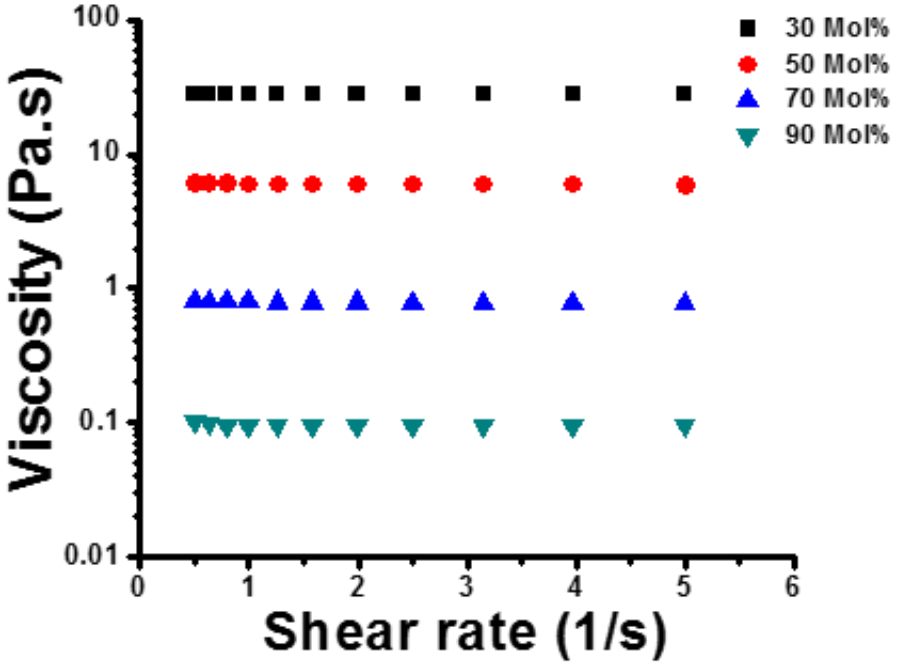

Figure 5.1 Viscosity as a function of shear rate for printing formulations, Mol% indicates UA loading level

During the SLA process a printed layer must achieve a high degree of cure (DOC) rapidly to ensure the printed layer has enough mechanical integrity to support the part during the AM process. In order to rapidly achieve a high DOC a AM formulation must exhibit rapid UV cure kinetics. The UV cure kinetics of printing formulations were studied using photorheology experiments where complex viscosity (η*), storage (G') and loss (G'') shear moduli were monitored upon applied oscillatory strain during photopolymerization. In Figure 5.2 we present the results of photorheology experiments studying BisGMA formulations with increasing UA loading level where η* is plotted as a function of irradiation time. Initially, all blends show a stable viscosity that decreases with increasing UA loading level. Upon UV irradiation at 15 s photopolymerization is

initiated and η* begins to increase as a function of irradiation time. A clear trend of increasing UV cure kinetics with an increase in UA mol% is observed where η* increases slowly during the irradiation time for 50 mol% formulation but increases rapidly as UA mol% is increased. Formulation photopolymerization kinetics are also quantified by monitoring their shear storage (G') and loss (G'') modulus as a function of irradiation time. The modulus crossover time where G' and G'' are equal is commonly used to describe the point at which a photopolymerizing network begins to behave more solid like than liquid like. The time to modulus crossover was used to compare reaction kinetics between formulations with increasing UA reactive diluent loading level in Figure 5.3. We observe that for an increasing UA mol% there is a decrease in the modulus cross over time. This decrease in time may be attributed to the increased mobility (decreased viscosity) of systems with higher UA mol% as observed in Figure 5.1. The results of photorheology experiments indicate rapid gelation in <10 s for blends with 50, 70, and 90 mol % UA, confirming that these blends have cure kinetics that are suitable for SLA 3D printing.

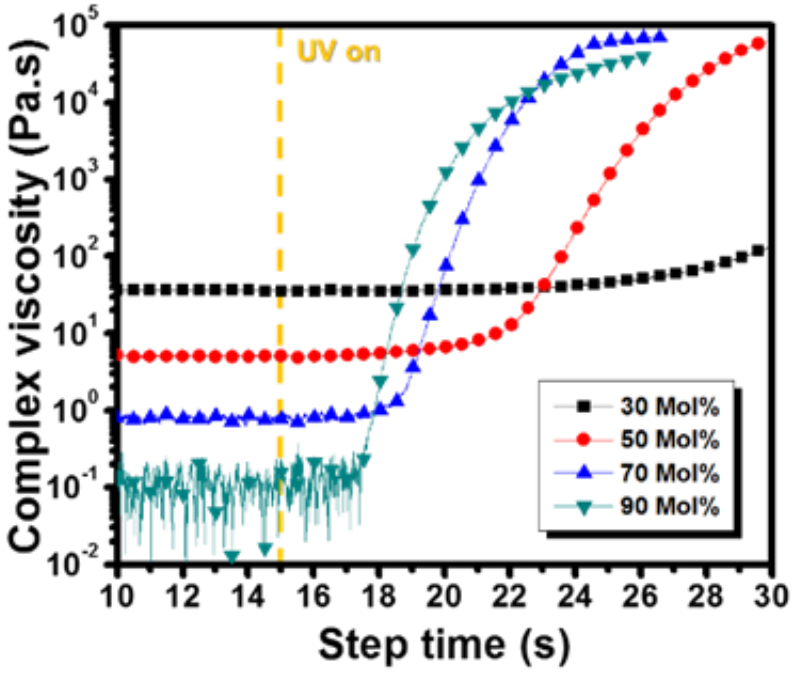

Figure 5.2 Complex viscosity plotted as a function of step time, Mol% indicates UA loading level

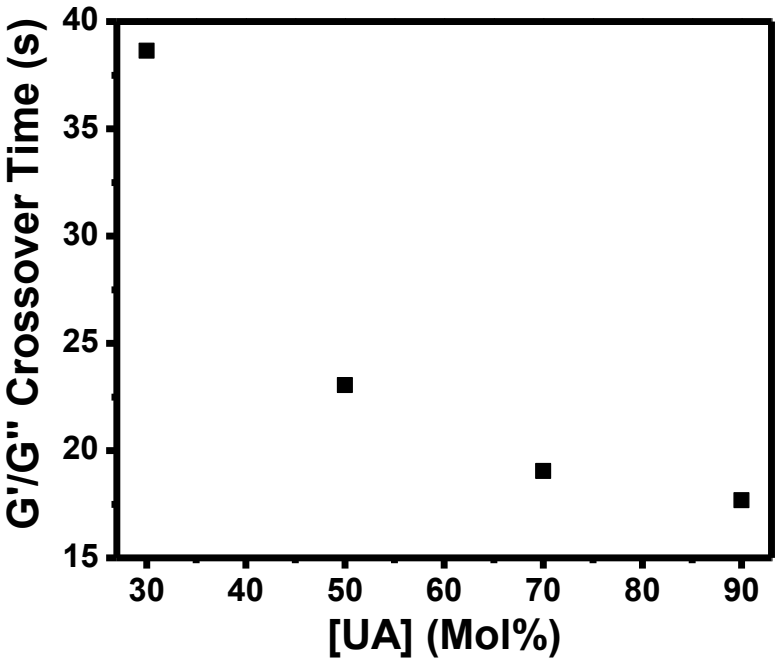

Figure 5.3 Average gel time plotted as a function of UA loading level.

5.2.2 Degree of Cure After 3D Printing.

Differences in both reactive diluent loading level and cure kinetics can lead to significant differences in the final DOC of a given network. These differences may also then significantly influence both experimental and simulation results. To account for this, ATR-FTIR spectroscopy was utilized to calculate the final degree of cure achieved in each 3D printed network. In Figure 5.4 we present the results of ATR-FTIR experiments where aliquots taken from printing formulations before 3D printing show peaks representative of polymerizable alkene is positioned at 1637 cm^{-1}.[67] Aliquots also exhibit an absorption at 1608 cm^{-1} which literature has shown may serve as an internal standard for DOC calculations in Bis GMA based formulations.[105] The DOC achieved during the printing process was calculated by relating the absorbance the double bonds to the aromatic absorbance using Equation 2. Representative spectra of a printing blend before and after printing (left) and peaks used for DOC calculations (right) are displayed in Figure 5.4. The DOCs calculated for each printing formulation are displayed in Table 5.1. Calculated DOC values remain relatively constant until 70 mol% UA where DOC values increase until 94.0% at 90 mol% UA. This trend may again be attributed to an increase in mobility during polymerization as the mol% of UA is increased.[106] The results of these experiments can then be used to guide appropriate calculated crosslink saturation values for simulations.

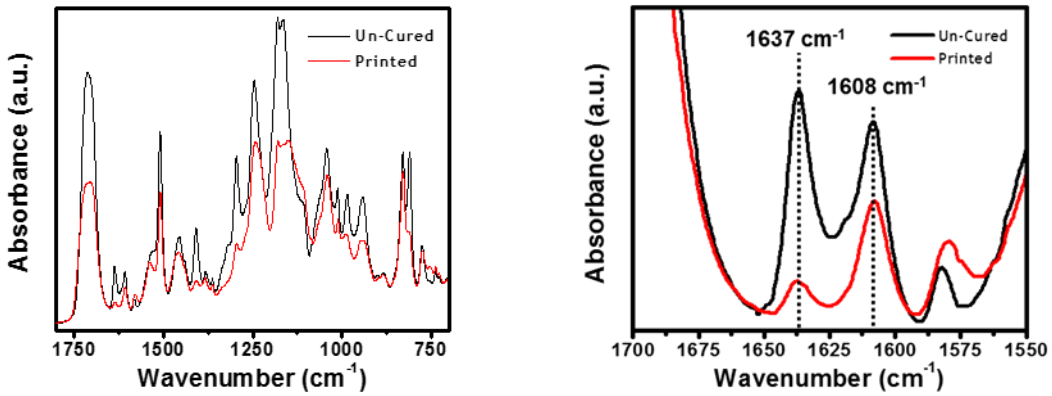

Figure 5.4 Left, full FTIR spectra of 60mol% 3D printed sample. Right, comparison of C=C stretch absorbance before and after 3D printing.

Table 5.1 DOC calculated for each UA loading level

UA Loading Level (Mol %)	Average DOC (%)
50	81.2
60	76.6
70	78.9
80	90.2
90	94.0

5.2.3 Disordered Cell Preparation and Simulated Crosslinking

Monomers were initialized randomly within the simulation cell using the Disordered System Builder within Schrödinger Materials Science Suite. Each simulated system is composed of 200 molecules (~10,000 atoms), where the number of Bis GMA and UA monomers are systematically varied to allow for the study of systems that closely match our experimental formulations. Table 5.2 summarizes the simulation cell composition of each formulation.

Table 5.2 Summary of simulation cell compositions and the associated experimental formulation. Note: 20 TPO-L photoinitiator molecules were added to each cell

Simulation Cells		**Experimental Printing Formulation**	
# Molecules UA	**# Molecules Bis GMA**	**Mol % UA**	**Mol % Bis GMA**
90	90	50	50
108	72	60	40
126	54	70	30
144	36	80	20
162	18	90	10

The resulting amorphous simulation cells were then equilibrated to allow for electrostatic reorganization of monomers followed by a compression step to condense the cell, removing unwanted inner volume. Details of amorphous cell construction and equilibration are described in detail in Section 2.5. Cell density was monitored during equilibration to ensure a stable density was reached before crosslinking. Figure 5.5 shows a representative plot of density as a function of simulation time over the last 5 ns of equilibration of a simulation cell with 90 Bis GMA monomers and 90 UA monomers. These simulations revealed that cells reach a stable, average room temperature density of 1.13 g/cm^3. This simulated result agrees well with experimental densities, where the density of Bis GMA is listed as 1.16 g/cm^3 and UA genomer 1122 is listed as 1.07 g/cm^3 in their respective technical data sheets.

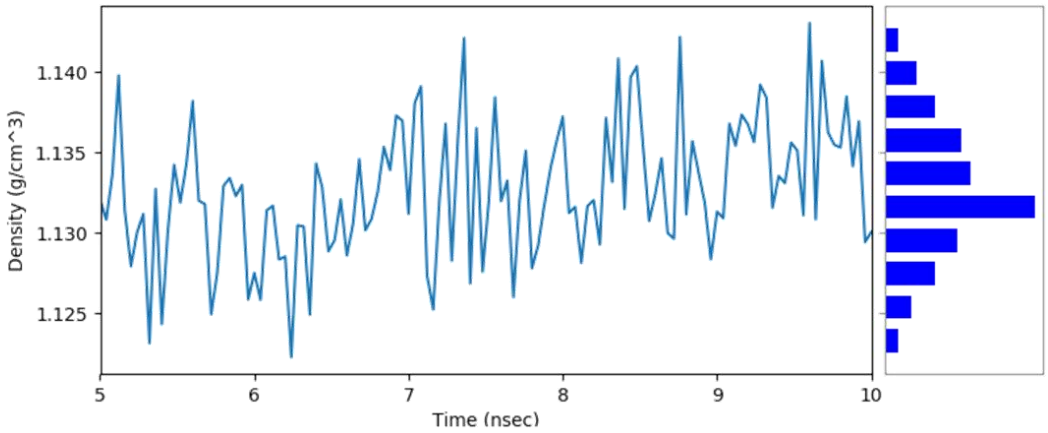

Figure 5.5 Representative plot of density as a function of simulation time at 300K for a disordered system composed of 90 Bis GMA monomers and 90 UA monomers.

Simulations used Schrodinger's crosslink analysis tool to quantify the gelation point of 3D printing formulations with increasing UA loading level. These simulations track the molecular weight of the two largest structures during crosslinking to monitor gelation. Figure 5.6 plots the average reduced molecular weight of the largest and second largest fragment in each formulation. The point at which the molecular weight of the largest fragment begins to diverge from that of the second largest fragment during the crosslinking simulation is used to define the gelation point of each system.[107,108] We observe that as UA mol% is increased the crosslink saturation at the gel point is increased, where crosslink saturation increases from 37.03, to 61.97, and 79.29 %, respectively , for formulations with 50, 70, and 90 UA mol%. This data is compared to gel points obtained experimentally during photorheology experiments in Table 5.2. Experimentally, gel points decrease from 23.05, to 19.04, and 17.69 s, respectively for samples with 50, 70, and 90 UA mol%.

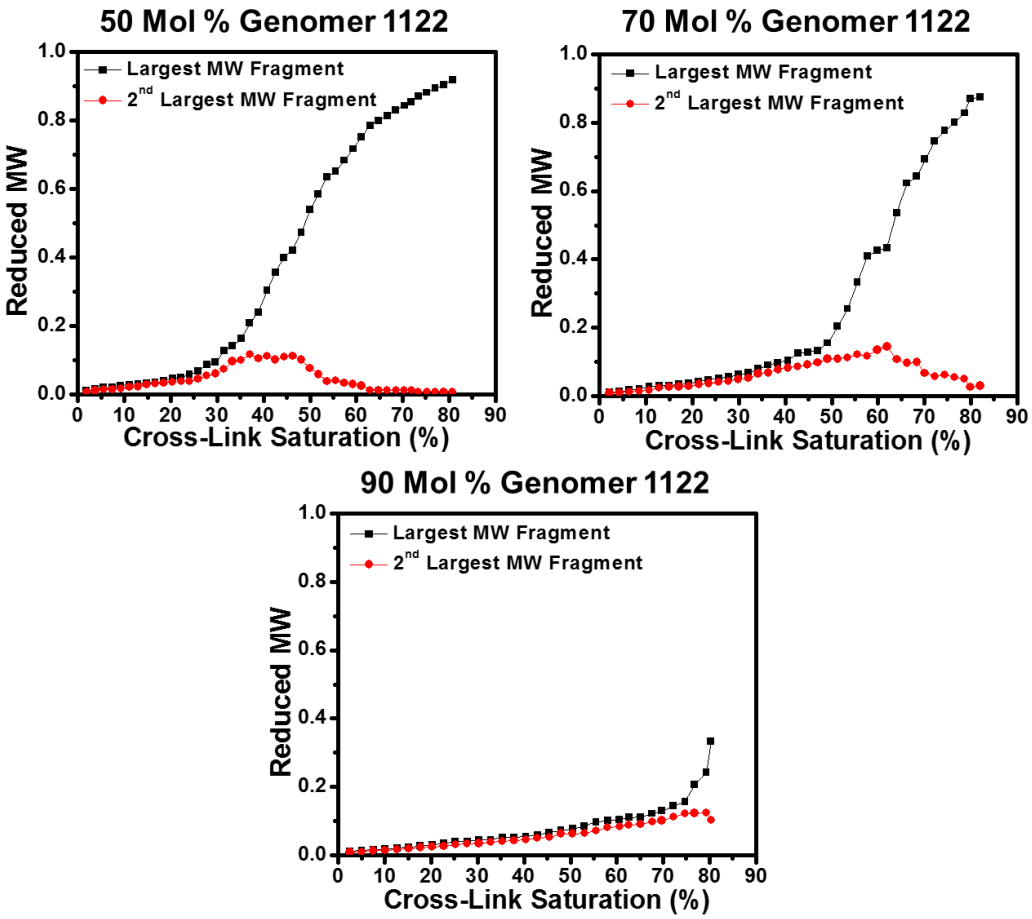

Figure 5.6 Largest molecular weight fraction and 2nd largest molecular weight fraction plotted as a function of cross-link saturation for formulations with increasing UA loading level.

Table 5.3 Crosslinking simulations compared to photorheology results

Mol % UA	Simulated Crosslink Saturation at Gel Point (%)	Experimental Gel Time (s)
50	37.03	23.05
70	61.97	19.04
90	79.29	17.69

During simulated crosslinking, the number of C=C double bonds available was tracked as a function of each crosslinking simulation iteration. All formulations initially show a linear decrease in C=C double bonds as a function of simulation crosslinking attempt, plotted in Figure 5.7 as simulation iteration. This linear decrease continues until significant molecular weight builds and diffusivity of monomers is reduced, limiting further reaction. Our crosslinking simulations neglect chain termination events and instead stop reaction at a pre-defined value of 95 % crosslink saturation. We observe however that at ~90 % degree of conversion mobility of reactive species becomes limited for all formulations, limiting further reaction. Formulations with increasing UA mol % reach this mobility limited conversion first, however these cells also inherently have the least amount of reactive C=C double bonds available due to decreasing di-functional bis GMA monomer concentration.

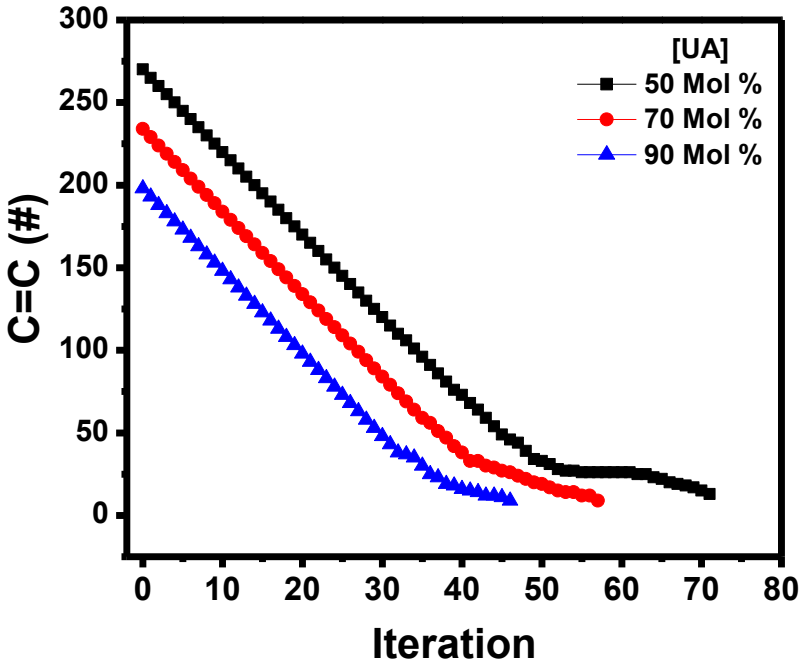

Figure 5.7 C=C double bond conversion profiles for formulations with increasing UA mol %

5.2.4 Experimental and Simulated Network Properties

Thermomechanical transitions of 3D printed networks with increasing UA loading level were investigated using dynamic mechanical analysis (DMA) in tension mode. Figure 5.8 shows results of these experiments where Tan Delta and storage modulus of blends with increasing UA mol % are plotted as a function of temperature. The ratio of the loss and storage moduli (E''/E') is used to calculate Tan Delta. This term relates energy dissipation relative to energy stored upon a periodic deformation. Estimating the T_g from the maximum of Tan Delta plotted as a function of temperature, experimental results follow a trend of decreasing T_g with increasing UA mol %. A similar trend is also observed in the rubbery plateau region, where as UA mol % is increased a systematic decrease in the rubbery plateau is observed. This trend is expected, as increasing the amount of mono-functional UA reduces the amount of available crosslinking sites thus reducing the overall network crosslink density.

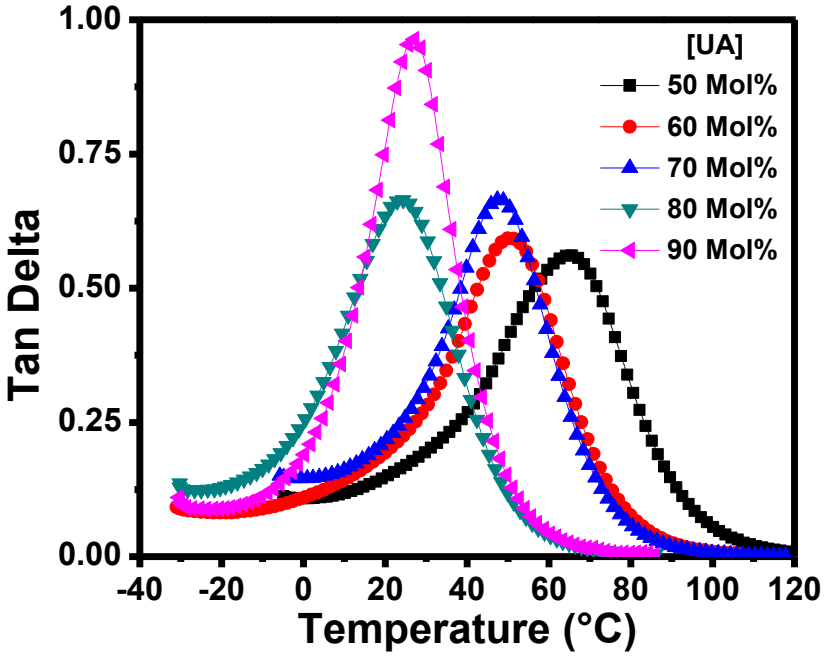

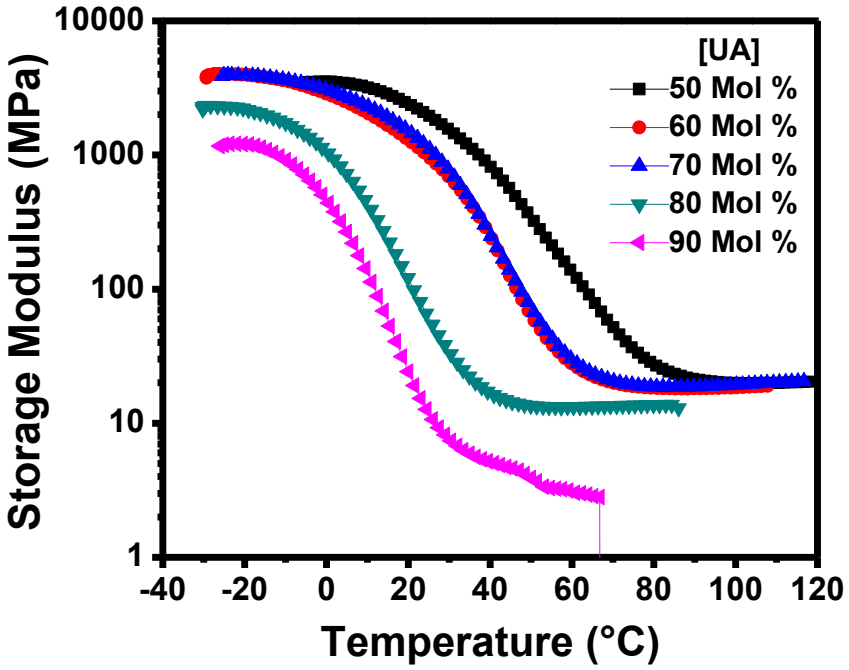

Figure 5.8 Plots of Tan Delta and storage modulus as a function of temperature with increasing UA mol %

The density of crosslinks may be calculated by using the storage modulus in the rubbery plateau. A higher E' value in the rubbery plateau would indicate a higher concentration of crosslinks. Results of DMA experiments are presented in Figure 5.9 plotted as rubbery E' as a function of UA loading level. The results of these experiments show a relatively constant rubbery E' value until 70 mol% UA where rubbery E' shows a significant decrease. The corresponding ν values calculated from the rubbery E' are summarized in Table 5.4. The crosslink density for 50 mol% UA blends are calculated to be 2.34×10^{-3} mol/cm^3 and begin to decrease after 70 mol% UA, reaching 5.47×10^{-4} mol/cm^3. This trend of decreasing ν with increasing UA mol% is expected as it is accompanied by a decrease in di-functional methacrylate BisGMA which behaves as a

crosslinking agent. This reduction in ν is also captured in simulations by a reduction in average simulated crosslinks from 216.4 at 50 mol% UA to 159.4 at 90 mol% UA. The reduction in simulated crosslinks can also be observed in the simulated crosslinked cells as a distribution of molecular weight in the cell. Crosslinked cells for each UA loading level in Figure 5.9 show a trend of increasing low molecular weight species as UA mol% increases.

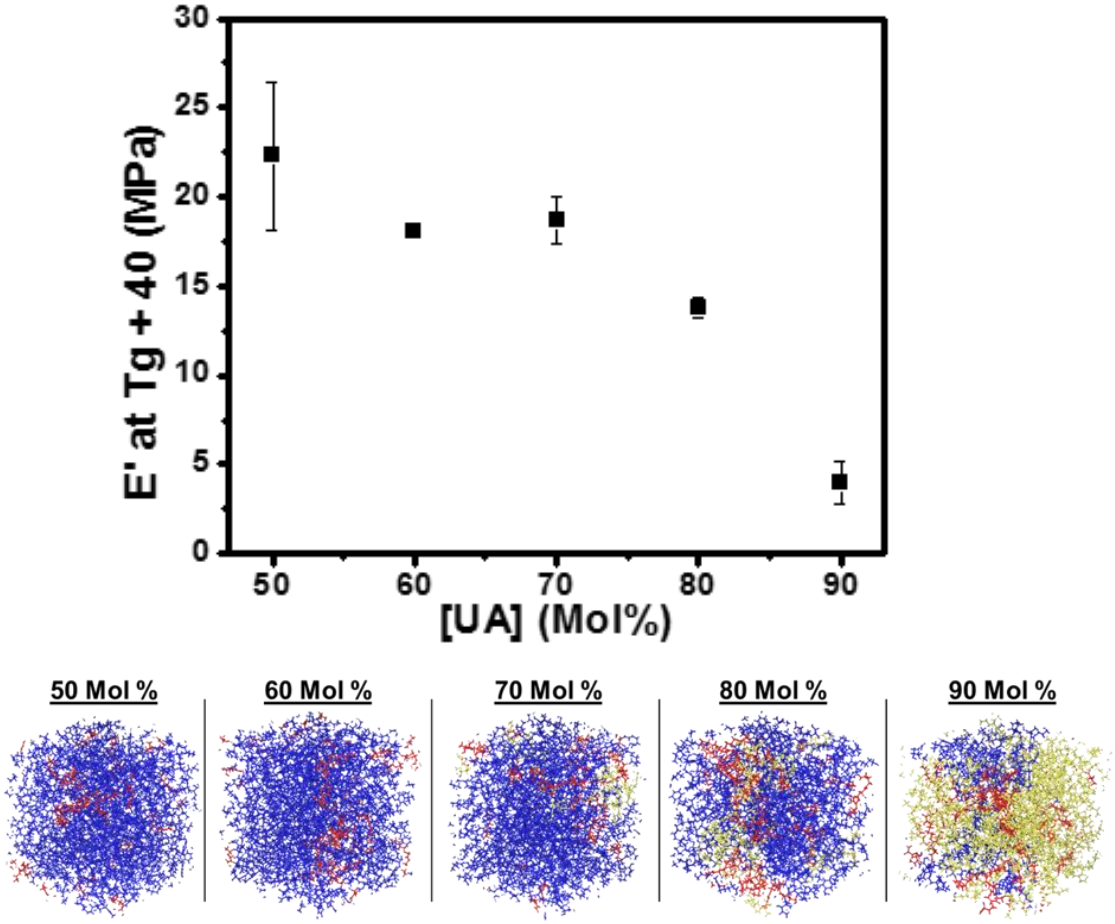

Figure 5.9 Rubbery modulus as a function of UA mol% and images of crosslinked cells from simulations with increasing UA mol% where unreacted monomer and oligomers are colored red and yellow respectively

Table 5.4 Calculated crosslink densities for each formulation compared to number of crosslinks achieved in each simulation

UA Loading Level (Mol %)	**E'Rubbery (MPa)**	**Crosslink Density (mol/cm^3)**	**Avg Total Simulated Crosslinks (#)**
50	22.32	2.34×10^{-3}	216.4
60	18.09	2.00×10^{-3}	202.4
70	18.65	2.07×10^{-3}	187.2
80	13.81	1.63×10^{-3}	174.2
90	4.00	5.47×10^{-4}	159.4

The T_g of simulated blends with increasing UA mol% were compared to 3D printed parts where the T_g was determined during DMA experiments. The T_g of a given polymer network is determined in molecular simulations by monitoring network density as a function of temperature during simulated annealing. A detailed description of the model utilized to calculated T_g during simulated annealing and uncertainty quantification of the results is described elsewhere in the literature.[109] Figure 5.10 shows a representative plot of density as a function of temperature for a crosslinked network composed of 50 mol% UA cooled from 800 K to 150 K. A hyperbolic curve may then be fit to the plot of density as a function of temperature and the T_g is taken as the intersection of the low and high temperature asymptotes of the hyperbola.

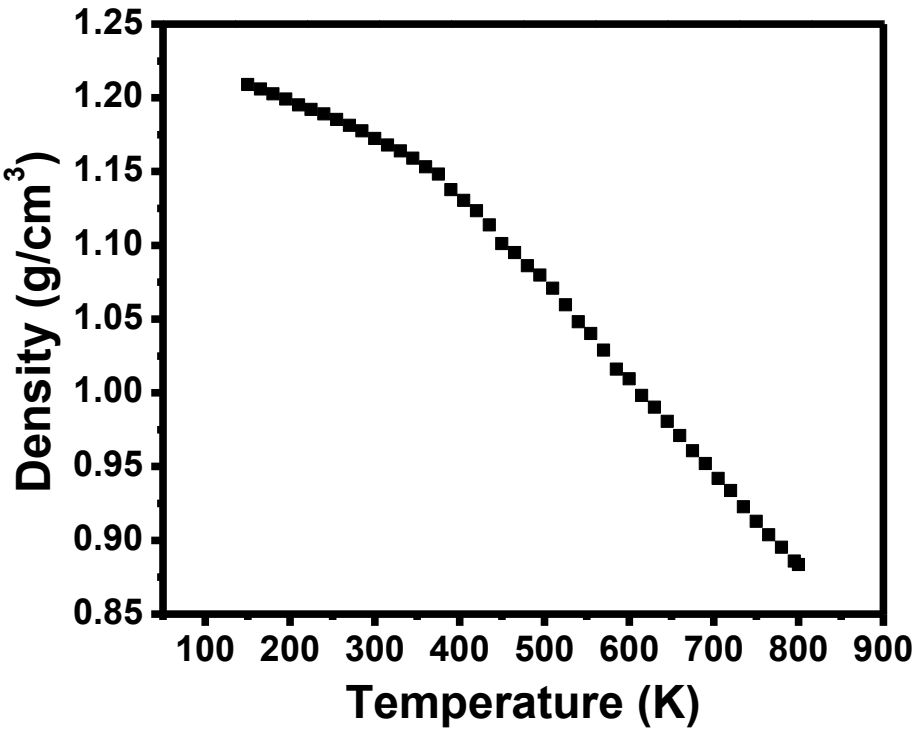

Figure 5.10 Representative density vs temperature plot obtained during simulated annealing of a 50 mol% UA network

Simulated and experimentally obtained T_g values are shown in Figure 5.11, plotted as a function of UA mol%. The T_g of each sample was determined during simulations as the intersection of the low and high temperature asymptotes of a hyperbola fit and during DMA experiments as the peak of Tan Delta plotted as a function of temperature. Each simulated T_g value is presented as an average of at least five simulations ± one standard deviation. It has been shown in the literature that the T_g of a polymer network is over estimated by MD simulations due to differences between simulated and experimental cooling rates.[110] Experimentally the T_g of a given polymer network is typically determined using heating and cooling rates on the order of seconds,

however during simulations heating and cooling is done on the order of nanoseconds.[111] Data presented in Figure 5.11 shows an agreement of <50 °C between simulations and experimental values, thus showing good agreement between simulated and experimentally obtained T_g values.

Simulations calculating network T_g values follow a trend of decreasing T_g with increasing UA mol %, the same trend observed experimentally. This trend also agrees well with the trend of decreasing simulated crosslinking sites with increasing UA mol % as discussed previously. This trend is anticipated, as an overall decrease in crosslink density would be expected to be accompanied by a decrease in T_g.

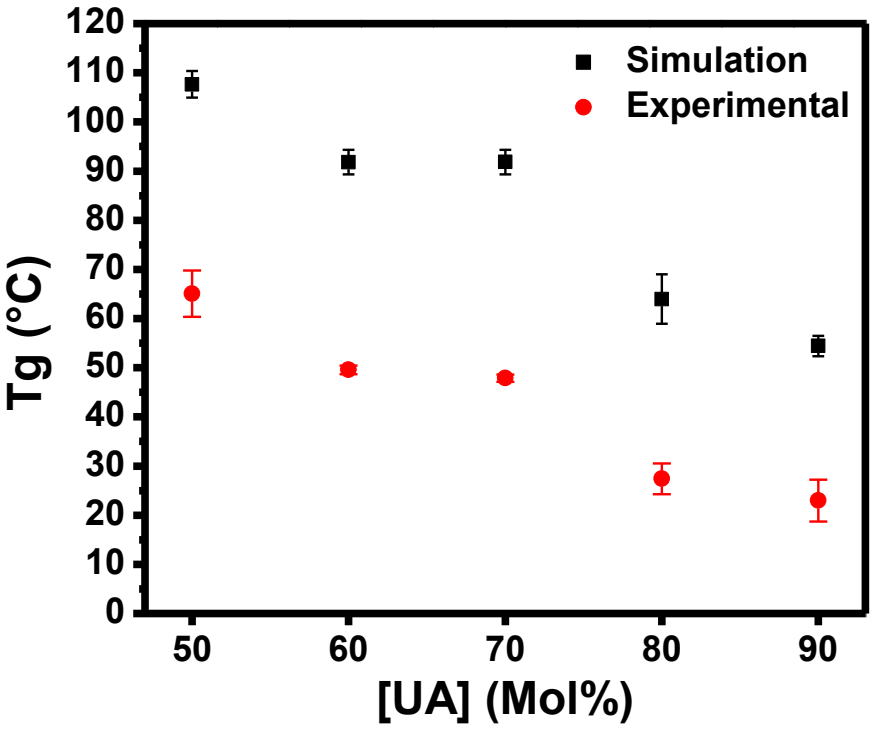

Figure 5.11 Glass transition temperature plotted as a function of UA mol%

5.3 Conclusions

The work presented herein has characterized the cure kinetics and flow viscosity of an acrylate printing formulation, printed parts, determined the degree of cure achieved during the printing process, and studied thermomechanical properties using DMA. We were are then able to model the printing process using a fluorine atom to simulate a free radical polymerization and calculate the glass transition temperature at similar degrees of cure to those achieved experimentally. The printing formulation was studied as a function of increasing monofunctional acrylate loading level to observe the trend of decreasing T_g, rubbery modulus, and crosslink density both in simulations and experimentally. The work presented demonstrates MD simulations as a tool to model the behavior of 3D printed acrylate networks. Future work may utilize this approach to aid in the design of new monomers and formulations thereof for VPP 3D printing.

CHAPTER VI – Conclusions and Future Work

While AM materials development has gained significant attention, the increasing demand for performance from parts produced using AM necessitates the development of new materials tailored for the innovative process. This dissertation has addressed the limitations of AM materials by demonstrating a new class of dual-cure VPP AM printing materials that enable the manufacture of complex thermoset geometries utilizing BOX chemistries at ambient temperatures. This has been accomplished by fundamentally studying photopolymerizable BOX monomers blended with commercially available reactive diluents and a novel dual-cure reactive diluent. The last chapter of this dissertation addresses the limitation of AM materials through a computational approach, where we aimed to develop simulation methods of studying new AM materials.

In the third chapter of this dissertation, the viscosity of BOX based blends at room temperature was readily controlled using a commercially available urethane-acrylate reactive diluent, enabling SLA AM at ambient conditions. The SLA AM printing blends exhibited rapid photopolymerization kinetics at low photoinitiator loading levels, resulting in rapid gelation and high alkene conversion. Dual cured AM parts exhibited a significant increase in crosslink density, T_g, and compression modulus with secondary thermal cure after SLA AM. To the best of the authors knowledge, this is the first example of a BOX chemistry processed via SLA and demonstrates the potential for other BOX chemistries to be processed using a dual cure approach. Future work expanding upon this study should exploit the modular nature of BOX monomer synthesis to design additional dual-cure BOX monomers tailored for specific AM methods and applications.

Further characterization of how this dual-cure strategy may impact part mechanical properties and how properties vary with print orientation should also be conducted.

Building upon the third chapter, the fourth chapter of this dissertation demonstrates the synthesis of a novel dual cure BOX reactive diluent with both UV and thermal reactivity. This diluent is blended with a difunctional dual cure BOX monomer to prepare 100% dual cure BOX alloys for room temperature SLA AM of BOX networks. The viscosity of BOX monomer blends is readily controlled by modifying the concentration of the dual cure diluent to enable SLA AM at ambient conditions. BOX monomer blends photopolymerization kinetics were studied in detail, where high alkene conversion was observed after UV cure and high BOX conversion was observed after thermal polymerization. After thermal polymerization of BOX, AM parts exhibited thermal stability and T_g values similar to, or exceeding that of, commercially available bisphenol-A based BOX networks. Future work building upon this study should continue to lean on the modular nature of BOX monomer synthesis to design additional dual cure BOX monomers to further increase network T_g's and modulus values. In addition, methods of lowering the BOX polymerization temperature should be explored to allow for increased BOX polymerization conversion while limiting (meth)acrylate thermal degradation.

The fifth chapter in this dissertation aims to develop MD simulation methods to study photopolymerized networks after VPP AM. Simulations model a photopolymerization using a fluorine atom to simulate a free radical which is used to crosslink a blend of acrylate and (meth)acrylate monomers. The printing formulation was studied as a function of increasing mono functional acrylate loading level to observe a

trend of decreasing T_g and crosslink density both in simulations and experimentally. The work presented demonstrates MD simulations as a tool to model the behavior of AM parts based on acrylate and (meth)acrylate networks. Future work may utilize this approach to aid in the design of new monomers and formulations thereof for VPP AM. In addition, these simulations should be expanded to further study monomers with dual cure functionality. These simulations would aid in understanding how incorporating a secondary cure functionality may influence key parameters such as degree of cure, network architecture, and thermomechanical properties.

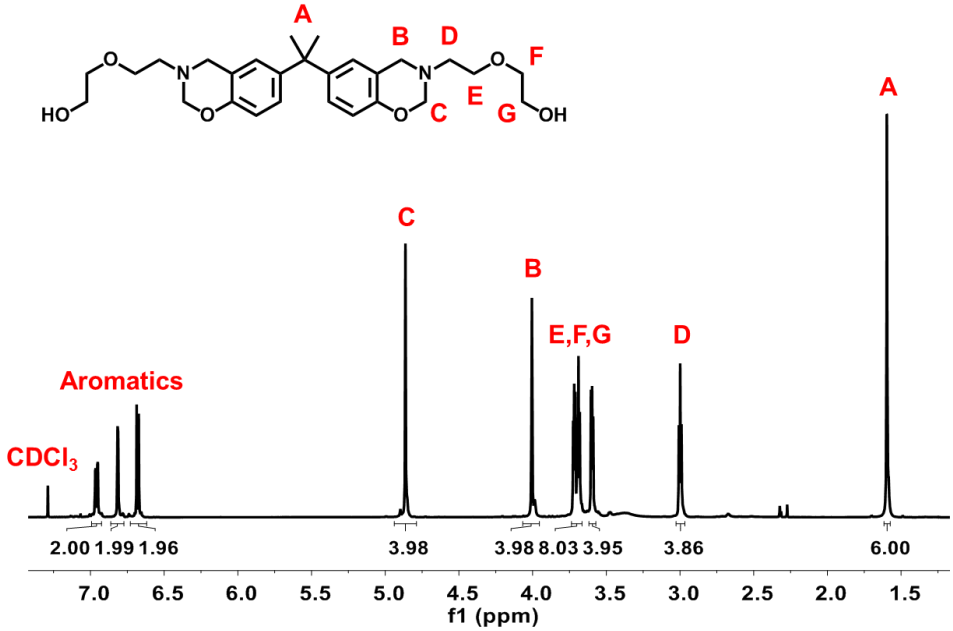

Figure A.1 H^1 NMR (600 MHz) spectrum of Di-Hydroxy Functional Benzoxazine Monomer

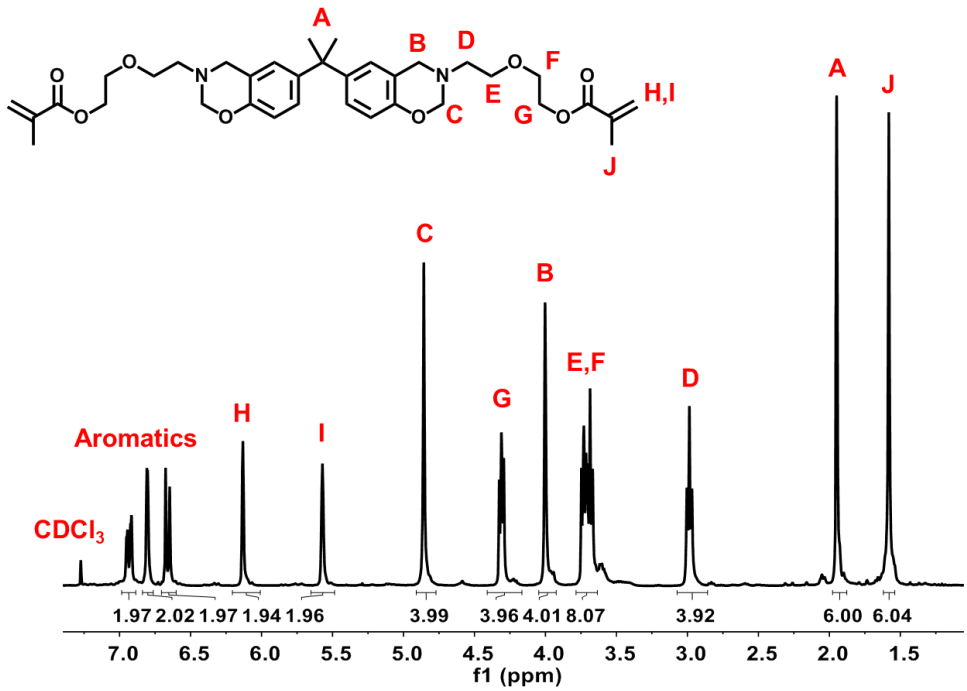

Figure A.2 H^1 NMR (600 MHz) spectrum of Di-(meth)acrylate Functional Benzoxazine Monomer (DMBOX)

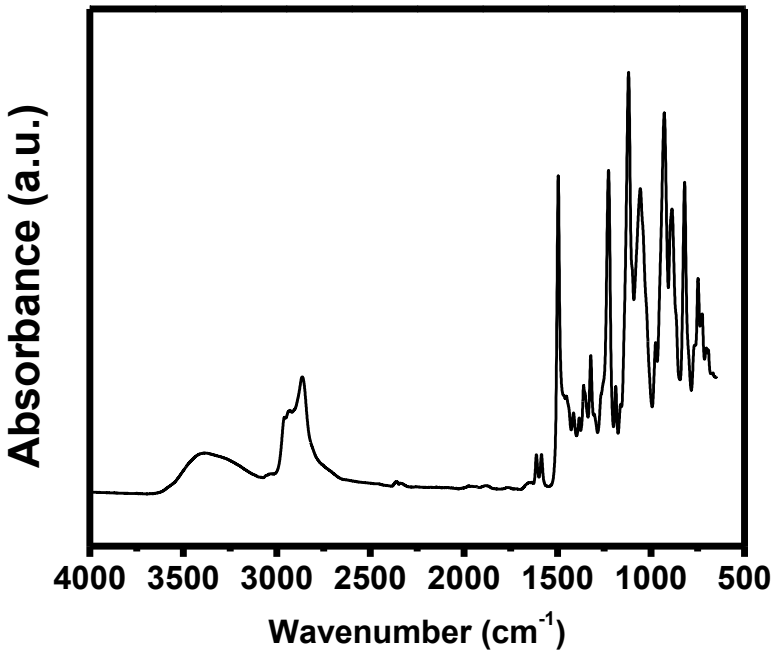

Figure A.3 ATR-FTIR spectrum of Di-Hydroxy Functional Benzoxazine Monomer

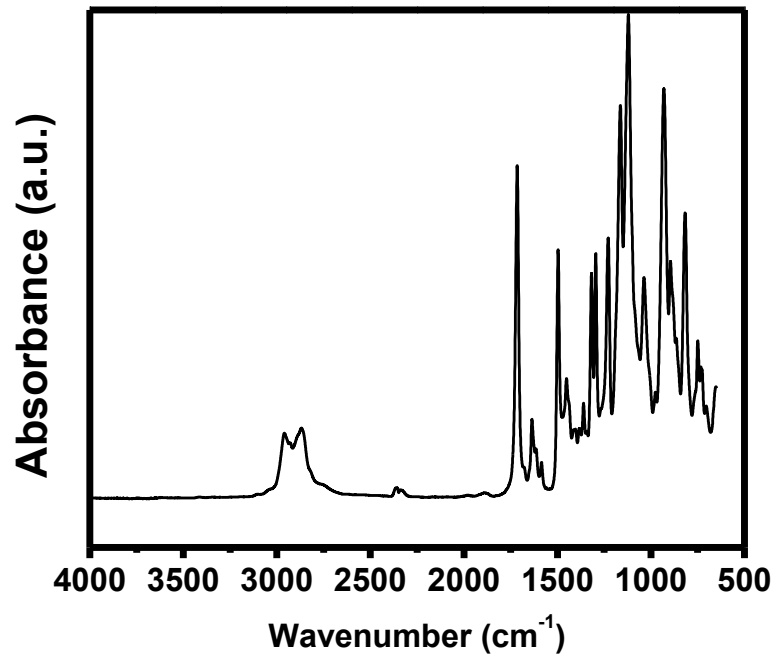

Figure A.4 ATR-FTIR spectrum of Di-(meth)acrylate Functional Benzoxazine Monomer (DMBOX)

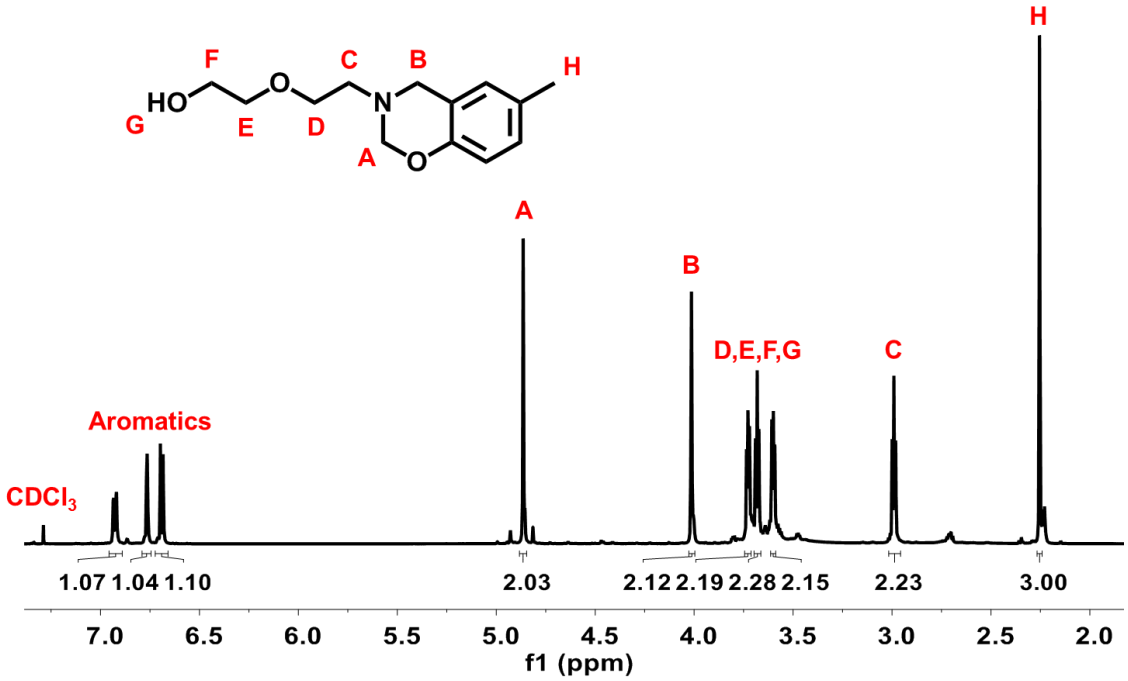

Figure A.5 H^1 NMR (600 MHz) spectrum of Mono-Hydroxy Functional Benzoxazine Monomer

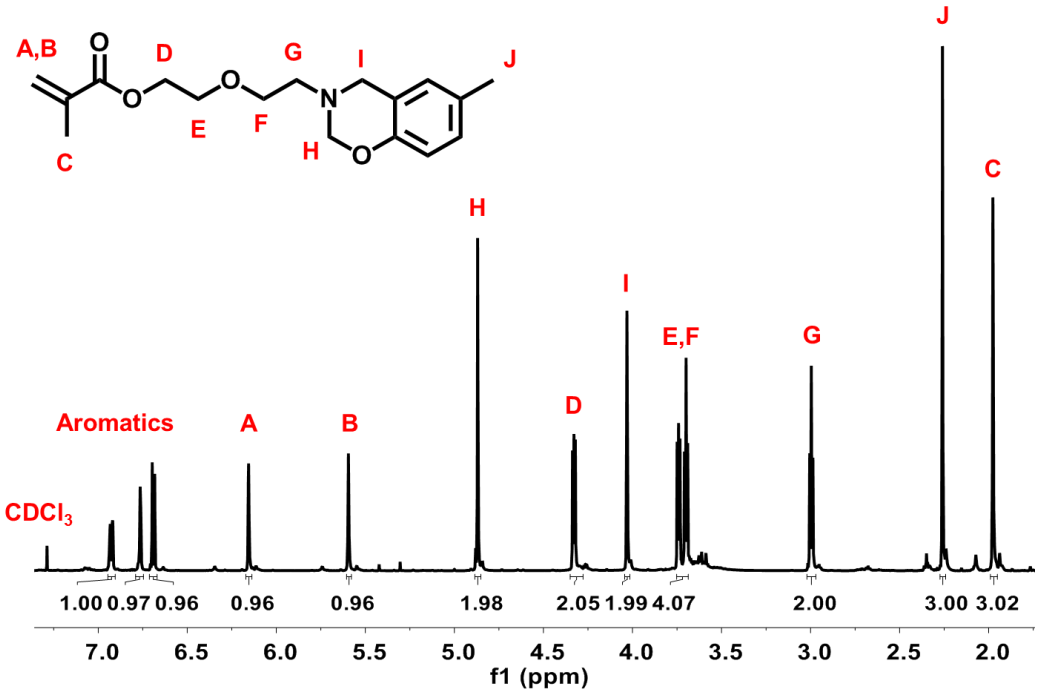

Figure A.6 H^1 NMR (600 MHz) spectrum of Mono-(meth)acrylate Functional Benzoxazine Monomer (MBOX)

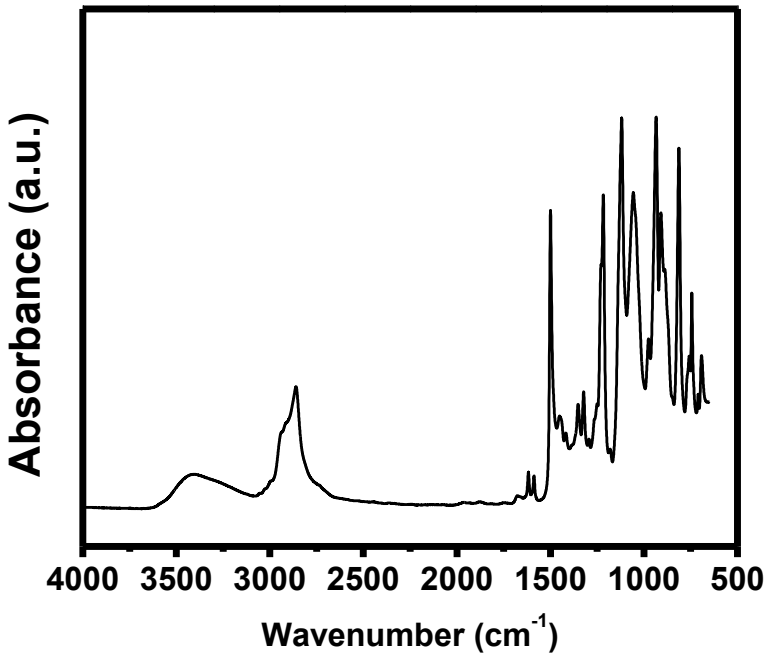

Figure A.7 ATR-FTIR spectrum of Mono-Hydroxy Functional Benzoxazine Monomer

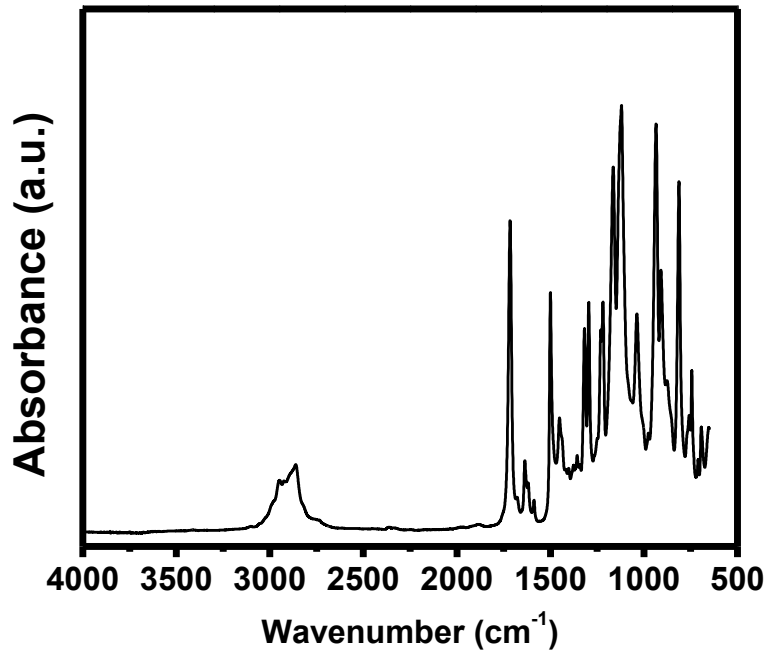

Figure A.8 ATR-FTIR spectrum of Mono-Hydroxy Functional Benzoxazine Monomer and Mono-(meth)acrylate Functional Benzoxazine Monomer (MBOX)

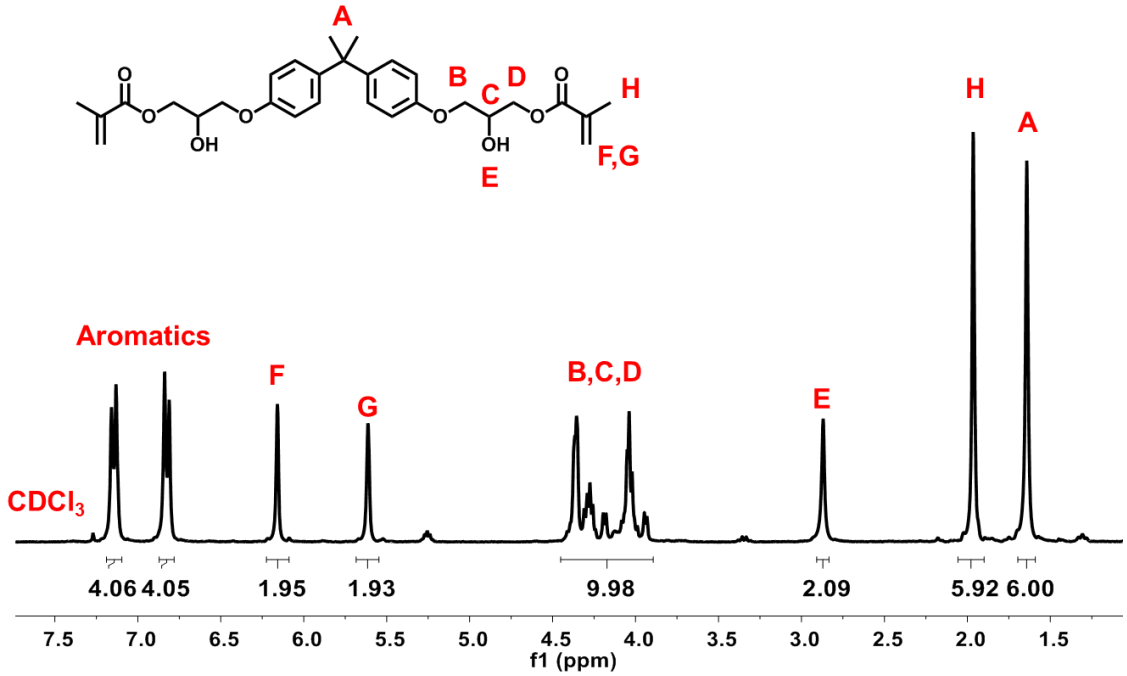

Figure A.9 H^1 NMR (300 MHz) spectrum of Bis-GMA Monomer

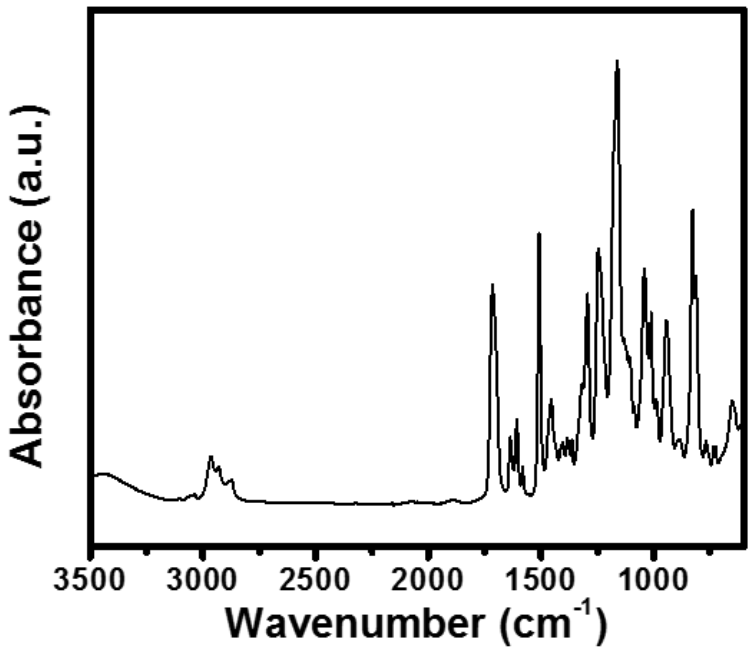

Figure A.10 ATR-FTIR spectrum of Bis-GMA Monomer

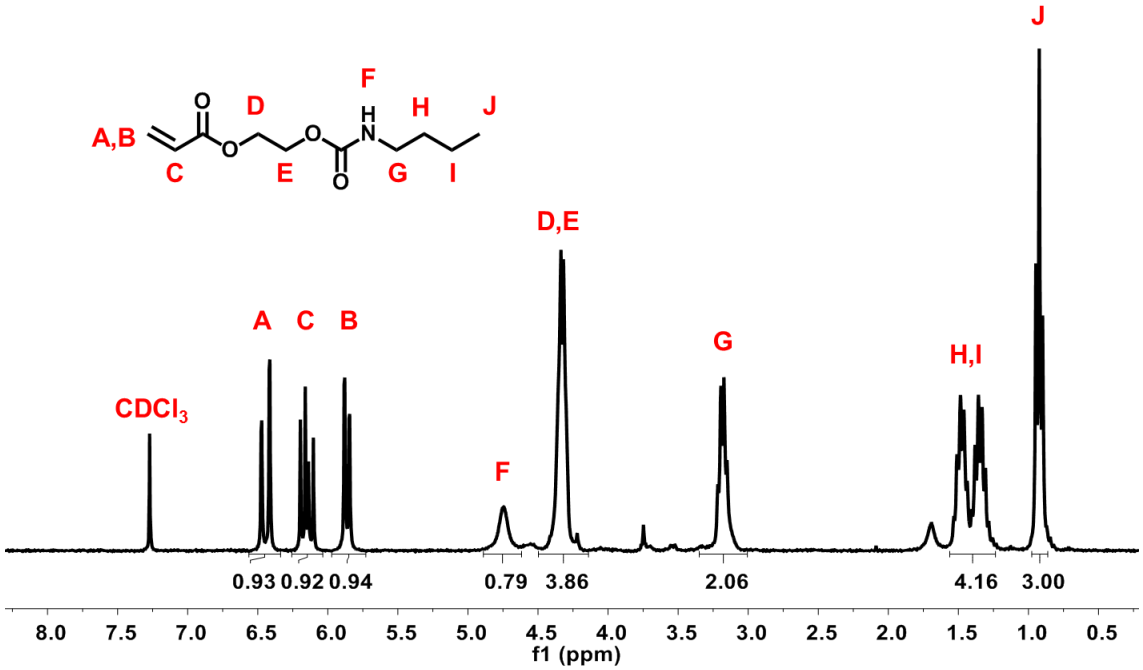

Figure A.11 H^1 NMR (300 MHz) spectrum of Genomer 1122 Monomer

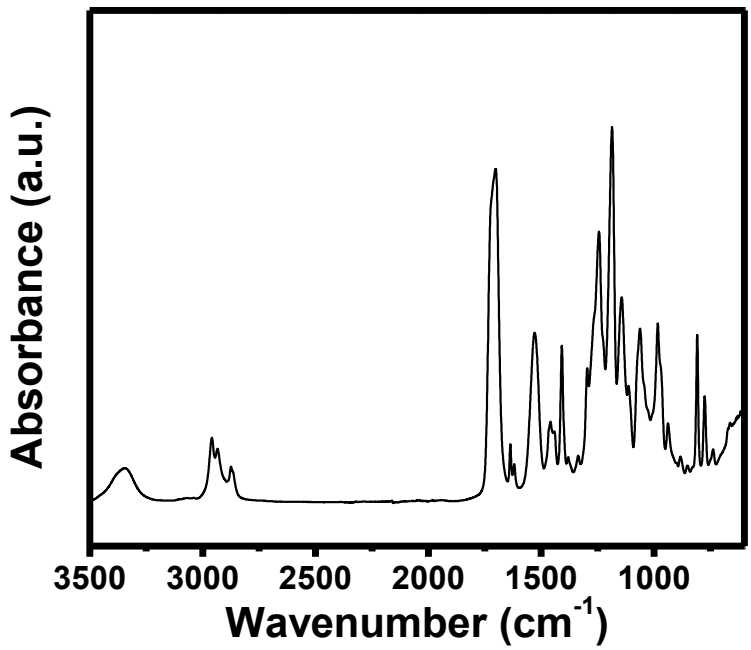

Figure A.12 ATR-FTIR Spectra of Genomer 1122 Monomer

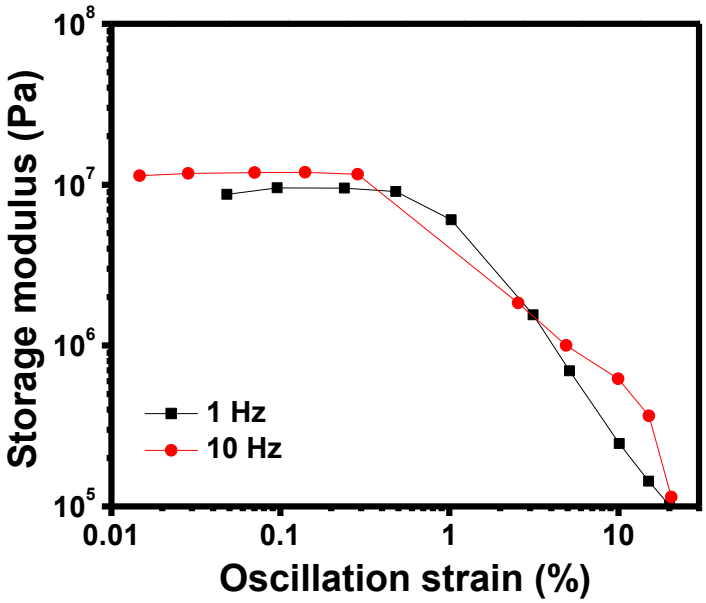

Figure B.1 Strain sweep of 60:40 DMBOX:RD blend with 1 Wt% TPO-L and a 0.5 mm gap

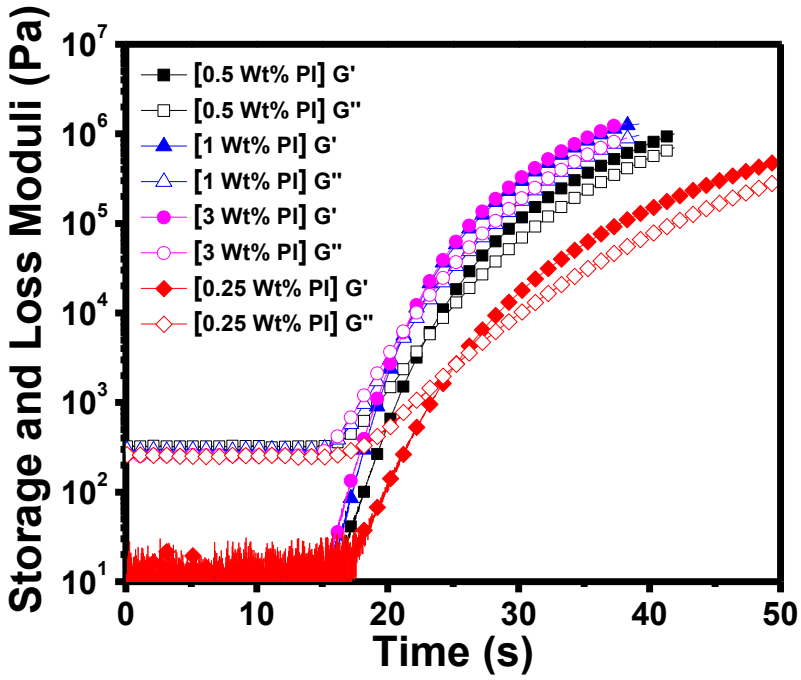

Figure B.2 Storage and loss modulus of 50 mol% MBOX blend with increasing TPO-L loading level as a function of time

REFERENCES

1. Huang, Y.; Leu, M. C.; Mazumder, J.; Donmez, A. *J. Manuf. Sci. Eng.* **2015**, *137* (1), 014001.
2. Ligon, S. C.; Liska, R.; Stampfl, J.; Gurr, M.; Mülhaupt, R. *Chem. Rev.* **2017**, *117* (15), 10212–10290.
3. Najmon, J. C.; Raeisi, S.; Tovar, A. *Review of Additive Manufacturing Technologies and Applications in the Aerospace Industry*; Elsevier Inc., 2019.
4. Liu, R.; Wang, Z.; Sparks, T.; Liou, F.; Newkirk, J. *Aerospace Applications of Laser Additive Manufacturing*; Elsevier Ltd, 2016.
5. Hofmann, M. *ACS Macro Lett.* **2014**, *3* (4), 382–386.
6. Wong, K. V.; Hernandez, A. *ISRN Mech. Eng.* **2012**, *2012*, 1–10.
7. Mitchell, A.; Lafont, U.; Hołyńska, M.; Semprimoschnig, C. *Addit. Manuf.* **2018**, *24* (September 2017), 606–626.
8. Bagheri, A.; Jin, J. *ACS Appl. Polym. Mater.* **2019**, *1* (4), 593–611.
9. Zhang, J.; Xiao, P. *Polym. Chem.* **2018**, *9* (13), 1530–1540.
10. Zarek, M.; Layani, M.; Cooperstein, I.; Sachyani, E.; Cohn, D.; Magdassi, S. *Adv. Mater.* **2016**, *28* (22), 4166.
11. Thrasher, C. J.; Schwartz, J. J.; Boydston, A. J. *ACS Appl. Mater. Interfaces* **2017**, *9* (45), 39708–39716.
12. Rusling, J. F. *ACS Sensors* **2018**, *3* (3), 522–526.
13. Wang, M. O.; Vorwald, C. E.; Dreher, M. L.; Mott, E. J.; Cheng, M. H.; Cinar, A.; Mehdizadeh, H.; Somo, S.; Dean, D.; Brey, E. M.; et al. *Adv. Mater.* **2014**, *27* (1), 138–144.

14. Jockusch, S.; Turro, N. J. *J. Am. Chem. Soc.* **1998**, *120* (45), 11773–11777.

15. Miao, X.; Zhu, W.; Zhang, Z.; Zhang, W.; Zhu, X.; Zhu, J. *Polym. Chem.* **2014**, *5* (2), 551–557.

16. Caronna, T.; Minisci, F. *Rev. React. Species Chem. React.* **1973**, *1* (2–4), 263–318.

17. Wang, F.; Wang, F. *J. Mol. Eng. Mater.* **2017**, *05* (02), 1740004.

18. Zhang, J.; Xiao, P. *Polym. Chem.* **2018**, 1530–1540.

19. Schuster, M.; Turecek, C.; Kaiser, B.; Stampfl, J.; Liska, R.; Varga, F. *J. Macromol. Sci. Part A Pure Appl. Chem.* **2007**, *44* (5), 547–557.

20. Konuray, O.; Fernández-Francos, X.; Ramis, X.; Serra, À. *Polymers (Basel).* **2018**, *10* (2), 178.

21. Jajam, K. C.; Bird, S. A.; Auad, M. L.; Tippur, H. V. *Polym. Test.* **2013**, *32* (5), 889–900.

22. Sperling, L. H.; Hu, R. *Polym. Blends Handb.* **2014**, 677–724.

23. Park, Y. J.; Lim, D. H.; Kim, H. J.; Park, D. S.; Sung, I. K. *Int. J. Adhes. Adhes.* **2009**, *29* (7), 710–717.

24. Dean, K.; Cook, W. D. *Macromolecules* **2002**, *35* (21), 7942–7954.

25. Jananee Narayanan Sivakami. 2015.

26. Oxman, J. D.; Jacobs, D. W.; Trom, M. C.; Sipani, V.; Ficek, B.; Scranton, A. B. *J. Polym. Sci. Part A Polym. Chem.* **2005**, *43* (9), 1747–1756.

27. El-ghayoury, A.; Boukaftane, C.; de Ruiter, B.; van der Linde, R. *Macromol. Symp.* **2002**, *187*, 553–561.

28. De Ruiter, B.; El-Ghayoury, A.; Hofmeier, H.; Schubert, U. S.; Manea, M. *Prog. Org. Coatings* **2006**, *55* (2), 154–159.

29. Jin, L.; Agag, T.; Yagci, Y.; Ishida, H. *Macromolecules* **2011**, *44* (4), 767–772.

30. Mohamed, M. G.; Hsu, K. C.; Kuo, S. W. *Polym. Chem.* **2015**, *6* (13), 2423–2433.

31. Koz, B.; Kiskan, B.; Yagci, Y. *Polym. Bull.* **2011**, *66* (2), 165–174.

32. Holly, F. W.; Cope, A. C. *J. Am. Chem. Soc.* **1944**, *66* (11), 1875–1879.

33. Burke, W. J. *J. Am. Chem. Soc.* **1949**, *71* (2), 609–612.

34. Burke, W. J.; Murdock, K. C.; Ec, G. *J. Am. Chem. Soc.* **1954**, *76* (6), 1677–1679.

35. Burke, W. J.; Bishop, J. L.; Glennie, E. L. M.; Bauer, W. N. *J. Org. Chem.* **1965**, *30* (10), 3423–3427.

36. Higginbottom, H. 4,501,864, 1985.

37. Ishida, H.; Low, H. Y. *Macromolecules* **1997**, *30* (4), 1099–1106.

38. Low, H. Y.; Ishida, H. *J. Polym. Sci. Part B Polym. Phys.* **1998**, *36* (11), 1935–1946.

39. Ishida, H.; Allen, D. J. *J. Polym. Sci. Part B Polym. Phys.* **1996**, *34* (6), 1019–1030.

40. Wang, Y. X.; Ishida, H. *Polymer (Guildf).* **1999**, *40* (16), 4563–4570.

41. Agag, T.; Geiger, S.; Alhassan, S. M.; Qutubuddin, S.; Ishida, H. *Macromolecules* **2010**, *43* (17), 7122–7127.

42. Baranek, A. D. **2013**, No. December 2013.

43. Agag, T.; Jin, L.; Ishida, H. *Polymer (Guildf).* **2009**, *50* (25), 5940–5944.

44. Burke, W. J.; Glennie, E. L. M.; Weatherbee, C. *J. Org. Chem.* **1964**, *29* (4), 909–912.

45. Rimdusit, S.; Jongvisuttisun, P.; Jubsilp, C.; Tanthapanichakoon, W. *J. Appl. Polym. Sci.* **2009**, *111* (3), 1225–1234.

46. Wang, Y. X.; Ishida, H. *J. Appl. Polym. Sci.* **2002**, *86* (12), 2953–2966.

47. Zhang, C.; Wang, L.; Yu, R.; Zheng, S. *Morphology and Properties of Polybenzoxazine Blends*; Elsevier B.V., 2011.

48. Huang, M. T.; Ishida, H. *Polym. Polym. Compos.* **1999**, *7* (4), 233–247.

49. Kuang, X.; Zhao, Z.; Chen, K.; Fang, D.; Kang, G.; Qi, H. J. *Macromol. Rapid Commun.* **2018**, *39* (7), 1–8.

50. Deliballi, Z.; Kiskan, B.; Yagci, Y. *Polym. Chem.* **2018**, *9* (2), 178–183.

51. Narayanan, J.; Jungman, M. J.; Patton, D. L. *React. Funct. Polym.* **2012**, *72* (11), 799–806.

52. Dayo, A. Q.; Wang, A.; Derradji, M.; Kiran, S.; Zegaoui, A.; Wang, J.; Liu, W. *React. Funct. Polym.* **2018**, *131* (July), 156–163.

53. Macko, J. A.; Ishida, H. *J. Polym. Sci. Part B Polym. Phys.* **2000**, *38* (20), 2687–2701.

54. Ishida, H.; Low, H. Y. *Macromolecules* **1997**, *30* (4), 1099–1106.

55. Kiskan, B. *React. Funct. Polym.* **2017**, *129* (January 2017), 76–88.

56. Beyazkilic, Z.; Kahveci, M. U.; Aydogan, B.; Kiskan, B.; Yagci, Y. *J. Polym. Sci. Part A Polym. Chem.* **2012**, *50* (19), 4029–4036.

57. Lu, C. H.; Su, Y. C.; Wang, C. F.; Huang, C. F.; Sheen, Y. C.; Chang, F. C. *Polymer (Guildf).* **2008**, *49* (22), 4852–4860.

58. Herzberger, J.; Meenakshisundaram, V.; Williams, C. B.; Long, T. E. *ACS Macro Lett.* **2018**, *7* (4), 493–497.

59. Hegde, M.; Meenakshisundaram, V.; Chartrain, N.; Sekhar, S.; Tafti, D.; Williams, C. B.; Long, T. E. *Adv. Mater.* **2017**, *29* (31).

60. Lee, C.-U.; Vandenbrande, J.; Goetz, A. E.; Ganter, M. A.; Storti, D. W.; Boydston, A. J. *Addit. Manuf.* **2019**.

61. Kuang, X.; Zhao, Z.; Chen, K.; Fang, D.; Kang, G.; Qi, H. J. *Macromol. Rapid Commun.* **2018**, *39* (7).

62. Lu, H.; Stansbury, J. W.; Nie, J.; Berchtold, K. A.; Bowman, C. N. *Biomaterials* **2005**, *26* (12), 1329–1336.

63. Li, C.; Strachan, A. *Journal of Polymer Science, Part B: Polymer Physics*. 2015, pp 103–122.

64. SMARTS - A Language for Describing Molecular Patterns https://www.daylight.com/dayhtml/doc/theory/theory.smarts.html.

65. Holly, E. E.; Venkataraman, S. K.; Chambon, F.; Henning Winter, H. *J. Nonnewton. Fluid Mech.* **1988**, *27* (1), 17–26.

66. Winter, H. H. *Polym. Eng. Sci.* **1987**, *27* (22), 1698–1702.

67. Anastasio, R.; Maassen, E. E. L.; Cardinaels, R.; Peters, G. W. M.; van Breemen, L. C. A. *Polymer (Guildf).* **2018**, *150*, 84–94.

68. Hill, L. W. *Prog. Org. Coatings* **1997**, *31* (3), 235–243.

69. Banks, J. L.; Beard, H. S.; Cao, Y.; Cho, A. E.; Damm, W.; Farid, R.; Felts, A. K.; Halgren, T. A.; Mainz, D. T.; Maple, J. R.; et al. *J. Comput. Chem.* **2005**, *26* (16), 1752–1780.

70. Shivakumar, D.; Williams, J.; Wu, Y.; Damm, W.; Shelley, J.; Sherman, W. *J. Chem. Theory Comput.* **2010**, *6* (5), 1509–1519.

71. Jorgensen, W. L.; Maxwell, D. S.; Tirado-Rives, J. *J. Am. Chem. Soc.* **1996**, *118* (45), 11225–11236.

72. Sanders, J. M.; Giesen, D. J.; Gavartin, J.; Kwak, H. S.; Hughes, T. F.; Christensen, S.; Halls, M. D.; States, U.; Diego, S.; States, U.; et al. 1–10.

73. Sutton, J. T.; Rajan, K.; Harper, D. P.; Chmely, S. C. *ACS Appl. Mater. Interfaces* **2018**, *10* (42), 36456–36463.

74. Green, B. J.; Guymon, C. A. *Addit. Manuf.* **2019**, *27* (February), 20–31.

75. Xu, P.; Stockwell, J. US 9,157,007 B2, 2015.

76. Lin, P.; AGHABABAIE, Arian GREENE, R.; ADZIMA, B.; POMEROY, J. US 2018/0348646 A1, 2018.

77. Achten, D.; Büsgen, T.; Tillack, J.; Ludewig, M.; Tomczyk, Christoph Wagner, R. US 2018/0133953 A1, 2018.

78. Ji, Z.; Yan, C.; Yu, B.; Wang, X.; Zhou, F. *Adv. Mater. Interfaces* **2017**, *4* (22), 1–6.

79. Hsiao, L. C.; Badruddoza, A. Z. M.; Cheng, L.-C.; Doyle, P. S. *Soft Matter* **2017**, *13* (5), 921–929.

80. Sirrine, J. M.; Zlatanic, A.; Meenakshisundaram, V.; Messman, J. M.; Williams, C. B.; Dvornic, P. R.; Long, T. E. *Macromol. Chem. Phys.* **2019**, *1800425*, 1800425.

81. Melchels, F. P. W.; Feijen, J.; Grijpma, D. W. *Biomaterials* **2010**, *31* (24), 6121–6130.

82. Lee, S. S.; Luciani, A.; Månson, J. A. E. *Prog. Org. Coatings* **2000**, *38* (3), 193–197.

83. Chambon, F.; Winter, H. H. *J. Rheol. (N. Y. N. Y).* **1987**, *31* (8), 683–697.

84. Ross-Murphy, S. B. *Polymer (Guildf).* **1992**, *33* (12), 2622–2627.

85. Winter, H. H.; Chambon, F. *J. Rheol. (N. Y. N. Y).* **1986**, *30* (2), 367–382.

86. Winter, H. H.; Mours, M. In *Neutron Spin Echo Spectroscopy Viscoelasticity Rheology*; Springer Berlin Heidelberg: Berlin, Heidelberg, 1997; Vol. 134, pp 165–234.

87. Magami, S. M.; Williams, R. L. *Journal of Applied Polymer Science*. 2018.

88. Kim, R. J. Y.; Kim, Y. J.; Choi, N. S.; Lee, I. B. *J. Dent.* **2015**, *43* (4), 430–439.

89. Świderska, J.; Czech, Z.; Kowalczyk, A. *Polish J. Chem. Technol.* **2013**, *15* (2), 81–85.

90. Münchow, E. A.; Meereis, C. T. W.; de Oliveira da Rosa, W. L.; da Silva, A. F.; Piva, E. *J. Mech. Behav. Biomed. Mater.* **2018**, *82* (October 2017), 77–86.

91. Atai, M.; Watts, D. C.; Atai, Z. *Biomaterials* **2005**, *26* (24), 5015–5020.

92. Jian, Y.; He, Y.; Zhao, L.; Kowalczyk, A.; Yang, W.; Nie, J. *Adv. Polym. Technol.* **2013**, *32* (1), 1–9.

93. MacCallum, J. R. *Die Makromol. Chemie Macromol. Chem. Phys.* **1965**, *83* (1), 137–147.

94. Sudo, A.; Du, L.-C.; Hirayama, S.; Endo, T. *J. Polym. Sci. Part A Polym. Chem.* **2010**, *48* (13), 2777–2782.

95. Kolanadiyil, S. N.; Minami, M.; Endo, T. *Macromolecules* **2017**, *50* (9), 3476–3488.

96. Sini, N. K.; Endo, T. *Macromolecules* **2016**, *49* (22), 8466–8478.

97. Chernykh, A.; Liu, J.; Ishida, H. *Polymer (Guildf).* **2006**, *47* (22), 7664–7669.

98. Lu, H.; Lovell, L. G.; Bowman, C. N. *Macromolecules* **2001**, *34* (23), 8021–8025.

99. Kannurpatti, A. R.; Anseth, J. W.; Bowman, C. N. *Polymer (Guildf).* **1998**, *39* (12), 2507–2513.

100. Han, L.; Iguchi, D.; Gil, P.; Heyl, T. R.; Sedwick, V. M.; Arza, C. R.; Ohashi, S.; Lacks, D. J.; Ishida, H. *J. Phys. Chem. A* **2017**, *121* (33), 6269–6282.

101. Jungman, M. J.; Cobb, J. S.; Lawler, D. J.; Sholar, J. D.; Johnson, C. B.; Patton, D. L. *Macromol. Symp.* **2013**, *329* (1), 133–141.

102. Benzoxazine, B. A. **2014**, *70* (August), 1–4.

103. Schissel, S. M.; Jessop, J. L. P. *Polymer (Guildf).* **2019**, *161* (July 2018), 78–91.

104. Sirrine, J. M.; Meenakshisundaram, V.; Moon, N. G.; Scott, P. J.; Mondschein, R. J.; Weiseman, T. F.; Williams, C. B.; Long, T. E. *Polymer (Guildf).* **2018**, 1–10.

105. Stansbury, J. W.; Dickens, S. H. *Dent. Mater.* **2001**, *17* (1), 71–79.

106. Ortega, A. M.; Kasprzak, S. E.; Yakacki, C. M.; Diani, J.; Greenberg, A. R.; Gall, K. *J. Appl. Polym. Sci.* **2008**, *110* (3), 1559–1572.

107. Dušek, K.; Prins, W. *Structure and Elasticity of Non-Crystalline Polymer Networks*; 1969; Vol. 6.

108. Estridge, C. E. *Polymer (Guildf).* **2018**, *141*, 12–20.

109. Patrone, P. N.; Dienstfrey, A.; Browning, A. R.; Tucker, S.; Christensen, S. *Polymer (Guildf).* **2016**, *87*, 246–259.

110. Li, C.; Strachan, A. *J. Polym. Sci. Part B Polym. Phys.* **2015**, *53* (2), 103–122.

111. Han, J.; Gee, R. H.; Boyd, R. H. *Macromolecules* **1994**, *27* (26), 7781–7784.